



TAMPEREEN TEKNILLINEN YLIOPISTO
TAMPERE UNIVERSITY OF TECHNOLOGY

Johan Sand

Alpha Radiation Detection via Radioluminescence of Air



Julkaisu 1449 • Publication 1449

Tampere 2016

Tampereen teknillinen yliopisto. Julkaisu 1449
Tampere University of Technology. Publication 1449

Johan Sand

Alpha Radiation Detection via Radioluminescence of Air

Thesis for the degree of Doctor of Science in Technology to be presented with due permission for public examination and criticism in Festia Building, Auditorium Pieni Sali 1, at Tampere University of Technology, on the 21st of December 2016, at 12 noon.

Tampereen teknillinen yliopisto - Tampere University of Technology
Tampere 2016

ISBN 978-952-15-3882-7 (printed)
ISBN 978-952-15-3889-6 (PDF)
ISSN 1459-2045

Abstract

Alpha radiation presents a challenge for operators in the field of nuclear safety and security. Due to the short range (few centimeters in air) and high stopping power, alpha particles are conventionally detected with dedicated instruments in close proximity of the source. However, the thermalization of an alpha particle in air causes an effect similar to northern lights. The scale of this radioluminescence emission is very weak, but the increase in range and number of signal carriers allows remote detection of alpha particles. This Thesis investigates the light yield of this effect and its applications to alpha radiation detection.

An experimental approach is taken to estimate the amount of radioluminescence photons per single alpha particle. Two different methods are employed for the measurement and the result of 19 ± 3 photons/MeV is discussed in the light of previous works. In addition, the emission spectrum is recorded in order to support the observations. This knowledge is essential for quantitative performance estimations of the method.

Contamination screening at distances greatly exceeding the typical range of alpha particles is studied by two-fold approach. First, three types of scientific-grade cameras are used to image radioluminescence light of alpha radiation sources at a nuclear research facility. The images are taken through translucent materials in darkness, and the feasibility implications of this fieldwork are described. Second, the translation into operative use is facilitated by development of a remote mapping system, optimized for use in an illuminated environment. The system is based on single pixel detector with a telescope that is panned across an area of interest. The process is automated in order to demonstrate its potential in nuclear decommissioning applications.

Whilst the radioluminescence method enables remote mapping of alpha sources, further analysis of the emitters requires gamma spectrometry. Here, the optical signals of alpha particles are used to trigger a gamma measurement of materials which decay via simultaneous emission of an alpha particle and a gamma ray. This allows focusing of gamma measurement without collimators and provides an effective means to reduce background level for the detection of minute amounts of material.

The coincidence method is also applied to direct detection of radon decay in air by observing simultaneous photon detection events. For the demonstration, high speed electronics are employed for list mode collection of radon events. The results are carefully analyzed to maximize the potential of large measurement volume and the temporal response of the method. The developed detection system is benchmarked and calibrated against a leading commercial radon detector.

Overall, the results confirm that radioluminescence light can be successfully utilized for *in situ* detection and characterization of alpha radiation sources. Moreover, the method allows unprecedented approaches that may establish their niche in the coming years.

Preface

This work was carried out as a joint effort of Tampere University of Technology and Säteilyturvakeskus – Radiation and Nuclear Safety Authority during the years 2012-2016. I wish to express my gratitude to Alphamon (Tekes), GIFT-CBRN (EU FP7) and MetroDecom (EMPIR) projects which funded the major portion of this work. In addition, the support from Faculty of Natural Sciences (TUT) allowed me to concentrate on finalizing the work during the last few months. I also acknowledge the Finnish Support Programme to the IAEA Safeguards, funded by the Ministry of Foreign Affairs, for providing the vital financial support for the first field tests, and the Finnish Foundation for Technology Promotion for the personal grant.

First of all I would like to thank my supervisor Assoc. Prof. Juha Toivonen for providing this opportunity and for the energetic guidance over the years. I am also very grateful to my unofficial supervisors Dr. Harri Toivonen and Dr. Kari Peräjärvi. Your guidance and enthusiasm are the cornerstones of this Thesis. I am equally thankful to my co-author Dr. Sakari Ihtola whose insightful comments and positive attitude have been essential in the project. Moreover, I am indebted to my co-authors and collaborators Dr. Erich Hrncsek and Mr. Adrian Nicholl for their help and hospitality during the experiments in Karlsruhe. In addition, I wish to thank Mr. Tapani Honkamaa for the support in organizing the field tests and Mr. Philip Holm for all the help during GIFT project. I also thank Mr. Ari Laitinen for providing the radiation source and Mr. Antti Lepistö for manufacturing custom components for the research.

I have learned a great deal from senior D.Sc. students of Applied Optics Group and hence Albert, Jaakko and Tapsa deserve a thanks for their time and patience. Furthermore, it has been a joy to work in the friendly atmosphere of Optics Laboratory and I wish to thank every current and former member for being part of that great culture. I would especially like to thank Antti, Jussi, Kim, Mariusz, Mikko, Miro and Samu for the unforgettable discussions. I also thank the colleagues at Säteilyturvakeskus who were very friendly and helpful during my employment there.

I wish to thank my parents, Hilikka and Antero, for the continuous flow of support and encouragement over the several years of study and work. I also thank my sisters Anne and Leena together with your families, for the many happy moments that we have shared. Finally, I would like to thank Alexandra for being such a sunshine in my life.

Tampere, November 2016

Johan Sand

Contents

Abstract	iii
Preface	v
Symbols and abbreviations	ix
List of publications	xi
Author's contribution	xiii
1 Introduction	1
1.1 Aim and scope of the work	3
1.2 Outline of the Thesis	4
2 Radioluminescence in air	5
2.1 Interactions of alpha particles	5
2.2 Spectrum of nitrogen	6
2.3 Radioluminescence yield	12
3 Surface contamination detection and analysis	17
3.1 Alpha radiation detection	17
3.2 Camera imaging	18
3.3 Telescope scanning	26
3.4 Alpha-gamma analysis	34
4 Radon detection	39
4.1 Radon monitoring	39
4.2 Optical detection principle	41
4.3 System response	43
4.4 Considerations on background	46
5 Conclusions and discussion	49
Bibliography	53
Publications	63

Symbols and abbreviations

CCD	charge coupled device
CEA	Commissariat à l'énergie atomique et aux énergies alternatives
COTS	commercial off-the-shelf
cps	counts per second
CsTe	cesium telluride
EM	electron-multiplying
EMCCD	electron-multiplying CCD
FOV	field of view
GaN	gallium-nitride
HAUVA	Hand-held alpha UV application
HPGe	high-purity germanium
ICCD	intensified CCD
IR	infrared
ITU	Institute for Transuranium Elements
LaBr₃	lanthanum(III) bromide
LED	light-emitting diode
NaI(Tl)	sodium iodide (thallium activated)
MCA	multichannel analyzer
MDA	minimum detectable activity
MDC	minimum detectable concentration
MOX	mixed oxide
NORM	naturally occurring radioactive material
NTP	normal temperature and pressure
PIPS	passivated implanted planar silicon
PMT	photomultiplier tube
PSD	pulse shape discrimination
SBR	signal-to-background ratio
SDD	source-to-detector distance
SNM	special nuclear material

STUK	Säteilyturvakeskus – Radiation and Nuclear Safety Authority
TUT	Tampere University of Technology
QE	quantum efficiency
UV	ultraviolet
ZnS	zinc sulfide
3S	safety, security and safeguards
ϵ_α	alpha detection efficiency
ϵ_γ	gamma detection efficiency
μ	reduced mass
ω	frequency of harmonic oscillator
Ω	geometrical efficiency
ρ	average reflectance
τ	coincidence window length
A_S	surface activity
d	sphere diameter
D_e	dissociation energy
f	relative fraction of sphere openings
L	average path length in integrating sphere
L_D	detection limit
M	integrating sphere multiplier
N_α	alpha particle count rate
N_γ	gamma ray count rate
N_{random}	count rate of random coincidences
N_{S+B}	combined signal and background count rate
N_B	background count rate
P	probability of detection
P_c	coincidence probability
Q	pulse charge
r	intermolecular distance
r_e	intermolecular equilibrium distance
V	potential energy
x_0	anharmonic constant
Y	photon yield of an alpha particle

List of publications

- I J. Sand, S. Ihantola, K. Peräjärvi, H. Toivonen, and J. Toivonen, “Radioluminescence yield of alpha particles in air,” *New Journal of Physics*, vol. 16, p. 053022, 2014.
- II J. Sand, S. Ihantola, A. Nicholl, E. Hrnccek, K. Peräjärvi, H. Toivonen, and J. Toivonen, “Imaging of alpha emitters in a field environment,” *Nuclear Instruments and Methods in Physics Research Section A*, vol. 782, pp. 13-19, 2015.
- III J. Sand, A. Nicholl, E. Hrnccek, H. Toivonen, J. Toivonen, and K. Peräjärvi, “Radioluminescence mapping of alpha emitters under bright lighting,” *IEEE Transactions on Nuclear Science*, vol. 63, no. 3, pp. 1777-1783, 2016.
- IV S. Ihantola, J. Sand, K. Peräjärvi, J. Toivonen, and H. Toivonen, “Principles of UV-gamma coincidence spectrometry,” *Nuclear Instruments and Methods in Physics Research Section A*, vol. 690, pp. 79-84, 2012.
- V S. Ihantola, J. Sand, K. Peräjärvi, J. Toivonen, and H. Toivonen, “Fluorescence-assisted gamma spectrometry for surface contamination analysis,” *IEEE Transactions on Nuclear Science*, vol. 60, no. 1, pp. 305-309, 2013.
- VI J. Sand, S. Ihantola, K. Peräjärvi, H. Toivonen, and J. Toivonen, “Optical detection of radon decay in air,” *Scientific Reports*, vol. 6, p. 21532, 2016.

Author's contribution

The subject of the articles included in this thesis and their key points are listed below.

- | | |
|------------------------|---|
| Publication I | The radioluminescence yield of alpha particles is studied in air. Two different techniques are employed for the investigations. |
| Publication II | Three camera technologies are used to image alpha emitters in a glovebox at a nuclear research facility. The performance of the cameras and implications of the work are described. |
| Publication III | An automated radioluminescence mapping device is presented. The device is capable of stand-off alpha particle detection under bright lighting. |
| Publication IV | The first results of optical alpha-gamma coincidence measurement with a germanium gamma detector and a simple optical system are described. |
| Publication V | The alpha-gamma technique of Publication IV is further enhanced by utilizing a better optical system and X-ray spectrometer. |
| Publication VI | An optical radon detection method is reported. Experimental results are bench-marked with a state-of-the art radon detector. |

The Publications included in this thesis are results of collaborative team efforts. For Publications I, II, III and VI the author performed major contribution in all aspects of the work, including preparation and design, experiments, data analysis, and preparation of the manuscripts. For Publications IV and V, the author designed the optical systems, participated in the experiments and contributed to the reporting of optical systems.

1 Introduction

Materials that spontaneously decay by emitting an ionizing particle are defined as radioactive¹. Today, these types of materials are handled in power production, industry, research and medicine. The safe application of radioactivity would not be possible without reliable radiation detectors, most of which have a pedigree that dates back to early years of the nuclear era. Also, the prevalent best practices and regulations in radiological protection are based on the capabilities of established technologies. The three intertwined actions which together ascertain the safe and secure use of radioactivity are nuclear safety, security and safeguards (3S). In brief, nuclear safety is implemented to protect people and environment from radiation hazards² while nuclear security aims to protect the society from criminal actions where nuclear materials are involved³. Nuclear safeguards can be described as a set of actions which are agreed upon and performed to ascertain that peaceful nuclear activities are not diverted into a weapons program⁴. These operations are subject to high standards and therefore novel approaches are adopted conservatively. Nevertheless, developing new methods can be beneficial to all fields of 3S.

Radioluminescence light is created when ionizing particles excite material to higher energy states which decay by emitting an optical photon. Typically, it is exploited for self-illumination in applications where extended operational time is required without external power. Radioluminescence is also widely adopted for the detection of gamma rays in crystals that create light upon absorption of a highly energetic photon. In all these applications, the materials are selected for high light-yield and apt decay time to fulfill the desired purpose. In contrast to the aforementioned approach, this work utilizes the extremely weak radioluminescence emissions of air for the detection of alpha particles. Hence, the selection of scintillating media is not made on the basis of light yield but instead on the basis of abundance.

All ionizing particles excite radioluminescence in the atmosphere but the effect is best observed with alpha particles. They have a high stopping power and for this reason their range is only few centimeters in air¹. Because the excitation takes place within this short range from the radiation source, also the light emission is created within this relatively small volume^{5,6}. This has two implications: first, alpha particles can be detected from distances which greatly exceed their typical range. Second, the detection can be performed through translucent materials. The practical feasibility of these applications was not identified until the beginning of the new millennium⁷, although the radioluminescence of alpha particles in air has been known to scientists for more than a hundred years⁸.

A major challenge for the method is in differentiating between radioluminescence photons and normal background light. Air converts the kinetic energy of an alpha particle into optical photons with the efficiency of 10^{-5} order^{5,9,10}. This means that the remote detection capability is often achieved only in darkness, and even so, the light emission

from a single decay event is still very hard to distinguish from instrumental background. From this perspective, it is not surprising that the potential has been overlooked for a century. Fortunately, recent developments of scientific grade cameras and photomultiplier tubes together with advancements in optical filter manufacturing technology, have paved the way for new applications in low light detection. The demand for these technologies comes from other fields, which have sufficient critical mass for commercial use, but the outcomes can be utilized in optical detection of alpha particles and other ionizing radiations.

The need for new approaches in radiation detection is facilitated by the phase-out of first generation nuclear installations¹¹. This will be a major undertaking for the nuclear industry and it is estimated that Europe alone will decommission close to 150 nuclear power plants by 2030, which sets the expected market size to more than 80 billion dollars^{12,13}. It is distinctive that both the general audience and governments require clearance projects to be carried out in a rigorous manner. Also the industry has a strong incentive for efficient operations, since the commercial viability of nuclear power production is defined by the cost of decommissioning together with expenses related to disposal of spent fuel.

In addition to power plants, there will be a number of old nuclear research facilities decommissioned in the upcoming years. Many of them were built during the onset of commercial nuclear power, and their service life will come to an end soon. The prevalent problem with the early facilities is that they were not necessarily designed with decommissioning as a priority. To add to this problem, the knowledge of past activities can be lost as senior workers retire. The decommissioning of research facilities also differs from projects in the power industry since these facilities tend to be unique, and therefore, standard procedures are not easily established. Furthermore, the location and type of radioactive contamination is usually well known at power plants, whereas in research facilities separated materials may have been handled. Some of them can be very difficult to detect if their presence is not expected.

The substantial size of the upcoming decommissioning market is a major attraction for companies and innovators in the field of radiation detection. With regard to optical alpha imaging, it is very important to identify the most fruitful application areas to coordinate research and development efforts accordingly. At power plants, alpha contamination can be found in the primary circuit but to a lesser extent in other parts of the facility. A more prominent application area may be found in the decommissioning of fuel fabrication facilities and reprocessing plants where alpha contamination is a common concern. However, decommissioning should not be regarded as the only application of radioluminescence based alpha particle detection.

The central concern in nuclear security is the use of radioactive material as a poison or as a means to inflict disruption¹⁴. Especially materials and sources out of regulatory control pose a risk to the public and may proliferate to criminal or terrorist purposes. A prime example of the risk is the assassination of Alexander Litvinenko with radioactive polonium in 2006^{15,16}. The incident left traces of polonium in numerous locations and attracted a lot of media interest. The related forensic investigation and contamination screening was a laborious effort because alpha-active polonium can only be detected with surface contamination probes in close proximity. In order to raise preparedness for this kind of malevolent acts with alpha radiation sources, optical detection tools can be developed to assess the situation from a stand-off distance. The instruments may also find use as a payload on robotized vehicles or in automated screening applications.

1.1 Aim and scope of the work

The applications of optical alpha particle detection have been studied by several research groups around the Globe since it became recognized as a potential remote detection method by the pioneering works of Baschenko⁵ and Lamadie⁶ in 2004 and 2005. Outside of Finnish institutes, the number of peer-reviewed journal articles on the topic currently stands at six^{5,6,10,17–19} while most works in this field are published as conference proceedings. In Finland, the topic has been studied by Tampere University of Technology (TUT) and Säteilyturvakeskus – Radiation and Nuclear Safety Authority (STUK) since 2008.

The first goal of this Thesis is to determine the radioluminescence efficiency (i.e. photon yield) of alpha particles in air. There is currently no consensus on this subject, as very few studies exist. The aim is to measure the yield with an accuracy and precision that is sufficient for basic feasibility estimations. The experimental work is performed in normal indoor conditions. The spectral properties and environmental aspects affecting the yield are discussed in the light of electron studies, which are readily available in literature.

The second goal is to advance methods for remote detection and analysis of alpha radiation sources. For this purpose, scientific grade cameras are employed and a remote mapping system is developed. The imaging study has the most overlap with previous works and its scope is in different camera technologies and in their application in a real environment. The development of light-tolerant alpha contamination mapping system builds on the research conducted at TUT earlier²⁰, but this work takes the approach to a next level in terms of detection capability, light tolerance, and measurement automation. The located sources are analyzed by triggering a gamma spectrometer with radioluminescence photons of alpha particles. Previously, this method has been realized with conventional alpha detectors which are replaced with the optical approach in this work.

The third goal is to harness radioluminescence photons for the direct detection of radon decay. This is achieved by using coincidence counting with list mode data acquisition. The approach aims for rapid radon response by utilizing a large measurement volume and highly sensitive photon detectors.

In conclusion, this Thesis is a description of applied research work at the intersection of optics and nuclear physics. The main goals of the work can be summarized as follows:

- To determine the radioluminescence yield of alpha particles in air
- To develop remote surface contamination detection and analysis methods
- To demonstrate direct optical detection of radon decay in air

In all demonstrations, the target is in verifying the principle by using commercial off-the-shelf (COTS) components and laboratory instruments. The engineering efforts required to increase technology readiness are beyond the scope of this work.

1.2 Outline of the Thesis

This Thesis is based on six Publications which present the results of the work carried out between 2012 and 2016. The experimental work described in these Publications is summarized in Chapters 2-4 of this Thesis. The Chapters are structured to provide an overview on each subject area after which the current experiments and the main results are described. A discussion on the implications for practical applications concludes the Chapters.

The excitation of radioluminescence light and quenching effects are covered in Chapter 2. The experimental part of this Chapter is focused on the radioluminescence yield of alpha particles in air, studied in Publication I. In addition, the spectrum of radioluminescence light is measured to give insight on the effect. The results are compared with previous works and potential improvements for the experiment are discussed at the end of the Chapter.

Publications II-V present the surface contamination detection and analysis techniques that are summarized in Chapter 3. The remote detection of alpha sources with cameras and a dedicated telescope system is presented in Sections 3.2 and 3.3. The alpha-gamma analysis of located sources is introduced in Section 3.4. A more detailed description of this technique is available in the Thesis of Dr. Sakari Ihantola²¹, also featuring Publications IV and V. This Chapter also includes application examples of the aforementioned techniques that have not been previously published.

The optical radon measurement of Publication VI is presented in Chapter 4. It contains an introduction to radon after which the optical method is described and demonstrated. The final remarks include comparison with established radon detection technologies and discussion on potential causes of detector background.

Conclusions and implications of the current work are summarized in the final Chapter 5 together with a future outlook. The original Publications are included in the appendices of this Thesis.

2 Radioluminescence in air

Radioluminescence light is produced when ionizing particles excite material to higher energy states which then relaxate by emitting optical photons. Radioluminescence of alpha particles was discovered for the first time already in 1903 by William and Lady Huggins^{8,22,23}. At the time, the observations of Rutherford and Curie had suggested that radium emits positively charged particles, but their structure was not yet identified to be similar to that of helium nuclei. The discovery of Huggins was that ultraviolet (UV) light is emitted by a radium source, and furthermore, the emission wavelengths correspond to the spectrum of molecular nitrogen, when excited by electric discharge. Later on, the band spectrum of nitrogen was extensively studied and used for observation of cosmic rays, while the optical emissions of alpha radiation were left with little role in the scientific debate. In the context of astrophysics, the widely adopted term for the emissions induced by cosmic rays is “air fluorescence”, although the excitation is not of optical origin. Despite the differences in the primary particles, optical emissions of alpha radiation sources and cosmic rays share the same de-excitation characteristics, thereby providing a solid basis for air luminescence studies of alpha particles.

2.1 Interactions of alpha particles

Alpha particles are emitted in the spontaneous decay of heavy elements. They consist of two protons and two neutrons, which produces a net of two elementary charges. Due to this charge, Coulomb force is the main mechanism governing the interactions of alpha particles with matter. In contrast to electrons, the double charge of alpha particles intensifies the Coulomb interaction, and therefore, their energy loss per unit length is high. The energy loss is typically presented as a function of range with a Bragg curve, shown in Figure 2.1 for 5.5 MeV alpha particles. As observed in the fundamental investigations on radioactivity and structure of atoms^{24,25}, alpha particles mostly interact with electron clouds of other atoms and only very rarely collide directly with an atomic nucleus. Moreover, light electrons are more likely to change direction upon collision with much heavier alpha particles due to conservation of momentum ($m_\alpha/m_\beta \approx 7300$). Consequently, alpha particle trajectories tend to be straight in thin media.

Figure 2.1 shows that the typical alpha particle range is in the order of few cm in air at normal pressure, but is limited to a few μm in liquids and solids²⁶. This is explained by the high linear energy transfer, and therefore alpha particles are commonly described as non-penetrating type of radiation. For the same reason, external exposure is not considered harmful, as alpha particles are absorbed in the outer surface layers of skin before they reach living cells. However, this type of radiation is very dangerous if ingested or inhaled due to high damage potential for living tissues of the human body²⁷.

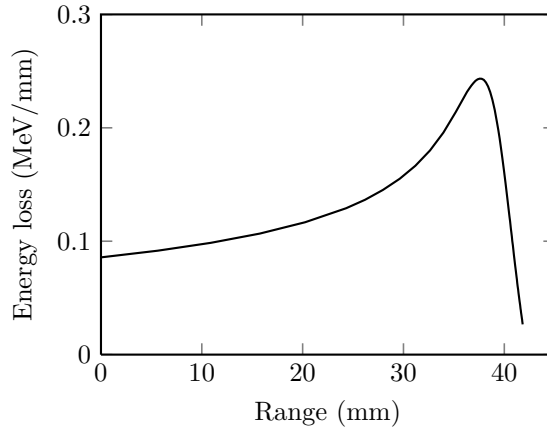


Figure 2.1: Energy loss of 5.5 MeV alpha particle as function of range in dry air at normal pressure (so-called Bragg curve). The curve is calculated from stopping powers reported in ²⁶.

Alpha particles in MeV energy range can ionize a great number of molecules and atoms during passage through media. The released electrons acquire kinetic energy from the alpha particle in accordance with the conservation of momentum, and these so-called secondary electrons* can further ionize other molecules and atoms. The mass ratio of colliding particles sets the upper limit for energy transfer in an elastic collision. In an alpha-electron interaction the limit is $4m_{\beta}/m_{\alpha}E_{\alpha} \approx E_{\alpha}/1800$ ¹. Hence, the thermalization of an alpha particle is a cascade of at least several thousands of collisions. The temporal duration of this process is in the range of a few nanoseconds¹.

The aforementioned interactions apply to beta particles as well, since they are electrons ejected in radioactive decay process. In contrast, gamma rays are highly energetic photons, and as such, they carry zero charge. Their ionizing nature arises upon absorption or scattering from an electron, which causes the electron to travel through media with the kinetic energy acquired from the photon. The main differences of these radiations to alpha particles are twofold. First, the energy released in beta or gamma decay is somewhat lower than in alpha decay on average. Second, their linear energy transfer is much smaller than that of alpha particles. Hence, the ion production of these radiations is less intense and distributed over significantly larger volume.

2.2 Spectrum of nitrogen

Atmospheric air consists of nitrogen (78 %), oxygen (21 %) and argon (1 %) together with trace amounts of other gas species. The aim of this work is to utilize atmosphere as an abundant scintillator, and for this purpose, the emissions of molecular and ionized nitrogen are best suited. Nitrogen has several narrow emission peaks at the near UV region which are an integral part of the auroral emission spectrum²⁸, and can reveal the presence of other ionizing particles too. The benefit of UV region is that the amount of natural background light is less intense with respect to visible wavelengths. Additionally, detection of UV photons is facilitated by their energy, which allows higher detection threshold to reduce spurious signals from e.g. thermal effects. The scintillations of other

*Secondary electrons are also known as delta electrons or delta rays²⁷.

atmospheric gases could also be used for the purpose, but their emissions are either weak or located at less desirable wavelengths²⁹. Therefore, this section will describe the origin and characteristics of nitrogen spectrum only.

Nitrogen is a diatomic homonuclear molecule and its spectrum has been thoroughly studied because of its significance for different fields of physical sciences. The atoms of a nitrogen molecule are bound together with a triple covalent bond. This type of bonding is very strong and inhibits further reactions with other atoms under normal conditions. The spatial structure of the diatomic molecule allows two degrees of freedom for its movement. First, the molecule can rotate around its center of mass. Second, the atoms can oscillate around their equilibrium points. Both the rotational and vibrational degrees of freedom are quantized in energy, which means that only discrete energy states are allowed. This gives rise to rotational and vibrational spectrum of the molecule.

In addition to the movements of atomic nuclei, the state of electron cloud is central in the definition of a molecular energy. Molecular orbitals describe the electronic state and are formed by superimposition of atomic orbitals of free atoms. A molecular orbital can be bonding or anti-bonding, depending on the energy with respect to corresponding atomic orbital. Bonding orbitals are of lower total energy than the corresponding atomic orbitals, whereas anti-bonding orbitals are destructive and higher in energy.

The ground state electron configuration of a nitrogen atom is $1s^2 2s^2 2p^3$. The 1s electrons have little role in the formation of molecular orbitals since their overlap is small. The bonding molecular orbitals are mostly formed by 2p orbitals. In ground state, the electron configuration of a nitrogen molecule is³⁰

$$(\sigma_g 1s)^2 (\sigma_u^* 1s)^2 (\sigma_g 2s)^2 (\sigma_u^* 2s)^2 (\pi_u 2p)^4 (\sigma_g 2p)^2. \quad (2.1)$$

Here, σ is used for orbitals which are cylindrically symmetrical with respect to intermolecular axis and π is used for asymmetric orbitals. The subscript “g” stands for symmetry and “u” for anti-symmetry to inversion through the center of the molecule. The asterisk denotes the anti-bonding character of the orbital.³⁰

The total energy of a molecule is formed as a sum of rotational, vibrational and electronic components. The optical spectrum results from allowed transitions between these states. The rotational transitions have small energy separation and the corresponding photons are emitted deep in the infrared (IR) range. The contribution of rotational transitions in the molecular spectrum in UV region is small, but can be observed with systems of high spectral resolution. There is no need or benefit to resolve these transitions in stand-off radiation detection applications.

From the practical point of view, the characteristic peaks of nitrogen spectrum in the UV region are explained by vibronic transitions. They correspond to electronic transitions which are accompanied by a change in the vibrational state. Each electronic state has a characteristic electron distribution, which results in different bond length and strength for each state. Hence, the states have distinct potential energy curves with a range of vibrational states. The vibrational states are denoted with a quantum number ν , which takes non-negative integer values.

As a homonuclear diatomic molecule, the spectrum of nitrogen can be described with relative ease by using the quantum mechanical approach. If the rotational energy levels of nitrogen are omitted, the molecule can be approximated as two masses which are connected with a spring. Furthermore, each stationary energy state can be described with

a wavefunction $\psi(r)$, where r is the separation from the molecular equilibrium distance. A classical starting point for the analysis of molecular states is the time-independent Schrödinger equation

$$-\frac{\hbar^2}{2\mu} \frac{d^2\psi(r)}{dx^2} + V(r)\psi(r) = E\psi(r). \quad (2.2)$$

This is a differential equation and its eigenvalue E corresponds to the energy of molecule. The potential $V(r)$ arises from the combined effect of molecular binding and nuclear repulsion forces. It is often described with so-called Morse potential. The equation for this asymmetric potential is

$$V(r) = D_e(1 - e^{-\beta(r-r_e)})^2, \quad (2.3)$$

where D_e is dissociation energy of state, r_e is the intermolecular equilibrium distance, and β is defined by $\beta = 2\pi\omega_0c\sqrt{\mu/2D_e}$. In this expression, μ is the reduced mass of the molecule and ω_0 is the fundamental frequency of vibration in wavenumbers.³¹

By using the Morse potential of 2.3 in the Schrödinger equation 2.2, one can solve the eigenstates of each vibrational level of a molecule^{30,31}. The solution for vibrational quantum state v is

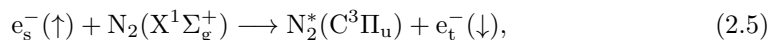
$$\frac{E_{vib}}{hc} = \omega_0(v + \frac{1}{2}) - \omega_0x_0(v + \frac{1}{2})^2 + \dots, \quad v = 0, 1, 2, \dots \quad (2.4)$$

This can be used to model the energy of a molecule at a certain vibrational state. The estimation requires that anharmonicity x_0 and fundamental frequency ω_0 are known.

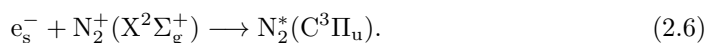
The Morse potentials of the most noteworthy electronic states of nitrogen molecule are plotted in the energy diagram of Figure 2.2. The required constants were taken from the extensive compilation of Lofthus & Krupenie³². Although the diagram is based on well established constants, it should be noted that Morse potential is an approximation. The diagram also shows the 2P and 1N transitions which are the most important band systems of nitrogen.

Excitation of nitrogen

Excitation of radioluminescence is mostly due to secondary electrons which are released by alpha particles. The 2P band of the nitrogen molecule cannot be directly excited from ground state, since this would require transition from a singlet to a triplet state. In other words, the total spin of the system is not conserved, which is forbidden by the so-called Wigner spin rule³³. Yet the excitation is possible via an exchange of low energy electron^{34,35}. This is described with



where e_s^- and e_t^- stand for a secondary and thermalized electron, respectively. This is the main excitation path for neutral nitrogen molecule and relaxation from higher states to this state is not considered to be significant³⁶. However, it is possible that some of the excitation arises from the recombination of ionized molecule³⁵. This process is described as follows



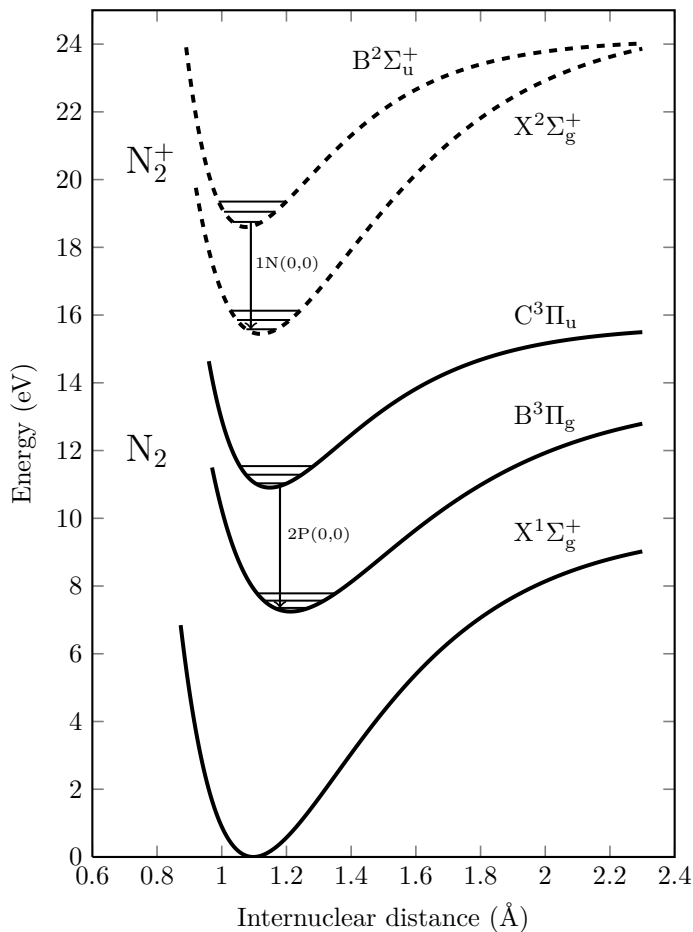
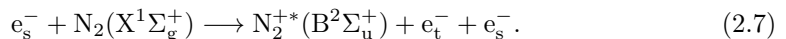


Figure 2.2: Selected energy levels of N_2 molecule illustrated with Morse potential plots, using molecular constants from Lofthus & Krupenie³². The first three vibrational levels ($v = 0, 1, 2$) are also depicted on the excited states. The most important radiative transitions of nitrogen molecule are in the 2P system ($C^3\Pi_u \rightarrow B^3\Pi_g$) and 1N system ($B^2\Sigma_u^+ \rightarrow X^2\Sigma_g^+$). The ground state of neutral molecule is $X^1\Sigma_g^+$.

The once-ionized nitrogen molecule emits light in the 1N system. The excitation takes place simultaneously with the ionization



The excitation efficiency of secondary electrons is highly dependent on their energy. The most effective excitation of 2P band system is observed with 14-15 eV electrons³⁷⁻⁴¹. The interaction probability vanishes rapidly towards lower energies and decreases somewhat slower towards higher energies. At 200 eV, the efficiency is already reduced by two orders of magnitude. For the 1N band system, the excitation cross-section peaks at 100 eV⁴², where also the highest ionization cross-section is observed⁴¹. It is interesting to note that alpha particles produce ten times more nitrogen ions than excited states of neutral molecule⁴³ while most of the light is still emitted by 2P bands of neutral nitrogen.

Table 2.1: Quenching constants ($10^{-10}\text{cm}^3\text{s}^{-1}$) at 20°C temperature for major nitrogen transitions. The values are averages of different works listed in Table 5.9 of reference²⁹. Large values correspond to strong quenching effect.

Molecule	$2\text{P}(v' = 0)$	$2\text{P}(v' = 1)$	$1\text{N}(v' = 0)$
N_2	0.1	0.3	3.9
O_2	2.4	2.9	5.3
H_2O	5.5	5.4	16.0

The majority of the nitrogen molecules in excited states relaxate by non-radiative collisional quenching. Hence, increasing number density of the gas (pressure) has a decreasing effect on the light yield. Furthermore, different molecules have different quenching efficiency, depending on their electron structures. The most important quencher in air is oxygen, but also nitrogen can quench its own emissions. Water vapor has even higher quenching constant than oxygen but the effect is less pronounced due to its lower abundance. Quenching rate constants of these molecules are listed in Table 2.1 to demonstrate their effect on radioluminescence yield. The constants increase proportionally to square root of temperature.²⁹

A molecule in an excited state can relaxate by spontaneous photon emission at any given time. The rate of quenching and spontaneous emission processes define the dominating de-excitation route. The intensity of an emission band is proportional to the Einstein coefficient and Frank-Condon factor of the transition⁴⁴. The former is the emission probability per unit time for given state. Frank-Condon factor is the overlap integral of vibrational wavefunctions of the lower and higher energy state⁴⁴. Alternatively, it can be described using the famous Frank-Condon approximation which states that transitions between electronic states are much faster than the consequent changes in intermolecular distance. For this reason, the factor is favorable for transitions between states that have approximately equal intermolecular distance (see Figure 2.2)²⁹. The Einstein coefficients and Franck-Condon factors are available in the literature⁴⁵.

Measurement of radioluminescence spectrum in air

Each band in the radioluminescence emission spectrum corresponds to a spontaneous transition from one electronic state to another. In order to illustrate the spectrum, a measurement was performed with a monochromator (Horiba iHR 550) and a low dark count rate photomultiplier tube (PMT) (Perkin Elmer, MP-1982P). The radioluminescence light of a 32 MBq ^{241}Am alpha source was collected to the monochromator input by a single lens. A high activity source is preferred for the measurement as very small portion of the isotropic emission can be guided through the monochromator. The spectrum is revealed by scanning the spectral bandpass of the monochromator by turning the grating. The grating has 1800 grooves per millimeter which in combination with 1 mm slits provides a spectral bandpass of 1 nm. The recorded radioluminescence spectrum is presented in Figure 2.3.

The result corresponds to the widely known spectrum of molecular nitrogen as expected. However, during this work some emissions at below 280 nm wavelengths were observed in laboratory trials in normal air. These emissions became the main motivation for Publication III, and in order to gain insight on the matter, the scan was repeated at 200-300 nm wavelengths with adjusted parameters for this Thesis. The emissions in deep

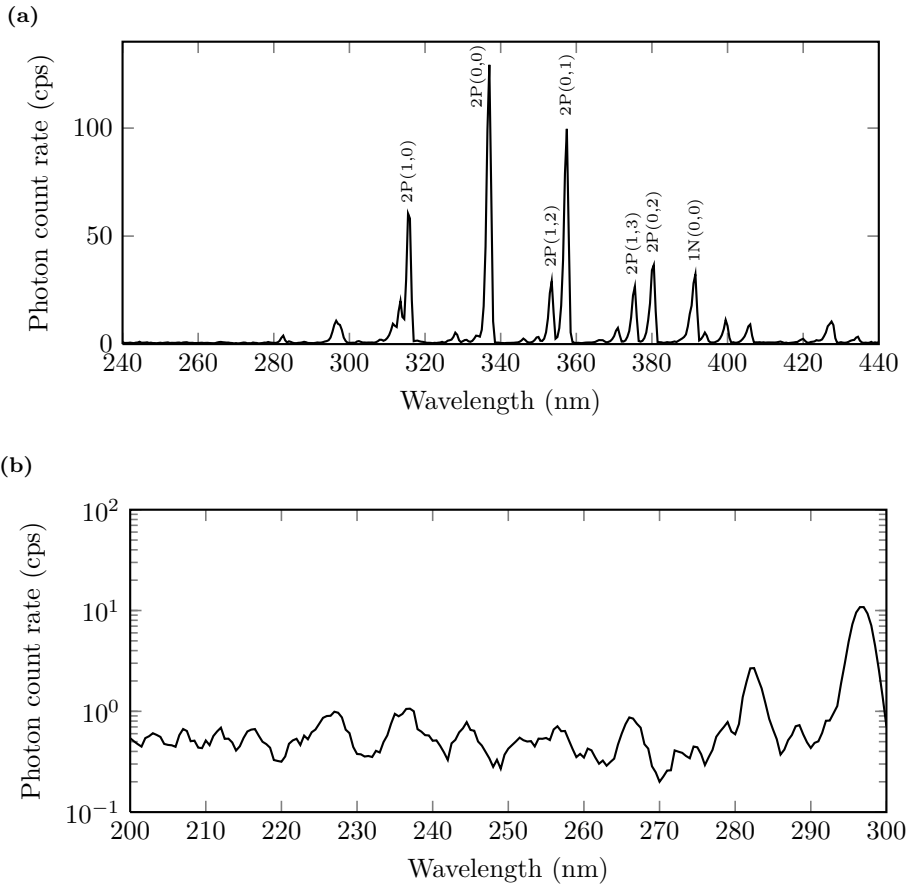


Figure 2.3: (a) Radioluminescence emission spectrum of air excited by Am-241 alpha particles. The spectrum is measured with monochromator (1 mm slits) and it is corrected for the instrument response. The most intense transitions are labeled. (b) Deep UV radioluminescence emissions measured with a monochromator and PMT. Larger slit size (2 mm) was used to reveal peaks at below 280 nm wavelengths and here the count rates are scaled to allow comparison with (a). Both spectra are recorded with 220 s integration per point.

UV are weak and a long acquisition time (220 s per point) was used together with wide (2 mm) monochromator slits. The result is shown in Figure 2.3b, which verifies that there are emission peaks also in this region. The recorded spectrum shows a consistent structure, and therefore, it is plausible that the observed bands are created by some lesser known processes or molecules. Some of the peaks correspond to band heads of nitric oxide as reported by Danielak et al.⁴⁶, but further and more focused investigations are definitely needed.

The interesting feature of this wavelength region is that the amount of background light is very low both indoors and outdoors. Indoors, the UV emissions of lamps are limited by absorption in the glass of the lamp. Outdoors, the absorber is ozone in the upper atmosphere which prevents the so-called solar blind wavelengths (220-280 nm) from reaching ground level^{47,48}.

The potential of this wavelength region has been recognized earlier by Ivanov et al. who used a solar blind camera for alpha imaging⁴⁹. In addition, a technical report describing the amount of light emitted was published in 2013⁵⁰. This report concludes that the radioluminescence yield in this region is around 0.08 solar blind photons per one MeV of energy deposited by a typical alpha particle. However, Figure 2.3b may show the first spectrally resolved measurement of radioluminescence in solar blind region. This was first published in a project deliverable⁵¹.

2.3 Radioluminescence yield

Light production of ionizing particles is based on the conversion of kinetic energy into excitation energy of spontaneously luminous molecular states. Optical emission competes with non-radiative relaxation and only a fraction of the initial kinetic energy is converted into optical photons while the rest is released via non-radiative relaxation. The luminescence efficiency of electrons is widely studied since they are the key constituent of cosmic rays^{29,52-57}. The information is used as a calibration parameter for cosmic ray (air fluorescence) telescopes, which observe the energy deposition and distribution of cosmic rays in upper atmosphere⁴⁴. Although the vast majority of astrophysicists use electron sources for air fluorescence studies, the results concerning de-excitation are directly applicable to alpha particles and vice versa³⁶. However, the excitation efficiency needs to be studied separately, since electrons are much lighter than alpha particles and carry only one elementary charge.

The first time that gas luminescence studies gained momentum was in 1950s and '60s, when the emerging PMT technology enabled fast measurement of low light levels. In these works, the scintillation properties of gases were extensively investigated, and in many cases alpha sources were utilized^{9,43,58-65}. The focal point of these works was in the luminescence of nitrogen, noble gases, and their mixtures. The interest is explained by their relatively high light yield, which showed potential for gas proportional counting applications.

Some of the early works describe the characteristics of air luminescence. Already Huggins⁸ noted that its spectrum corresponds to band spectrum of nitrogen, and his observations have been verified by numerous authors later on. Quantitative studies on the absolute light yield are rare, and the reason may be that air was not considered especially interesting for practical applications⁶⁶. One of the earliest reports on the light yield of alpha particles is published by Duquesne and Kaplan in 1960⁹. The authors presented a detailed analysis of the measurement geometry and concluded that approximately 60 photons are created in air by 4.6 MeV alpha particles.

The interest in alpha particle scintillation studies was re-established in 2004 by Bashenko, who proposed that the luminescence of air can be used for remote detection of alpha particle sources⁵. Bashenko estimated that the light yield of ²³⁹Pu alpha particles is 30 photons in the 300-400 nm region in normal air. The value was determined by collecting radioluminescence light onto an UV sensitive film that has a known sensitivity.

Self-absorption of the source has an effect on alpha particle energy and on the radioluminescence yield. Therefore, quantitative contamination measurements with the optical approach require detailed knowledge of these effects. In 2009, Bachelor et al. performed investigations with filter samples and also estimated the alpha particle radioluminescence efficiency which resulted in value of $1.3 \cdot 10^{-5}$ ¹⁷. The wavelength range was not specified

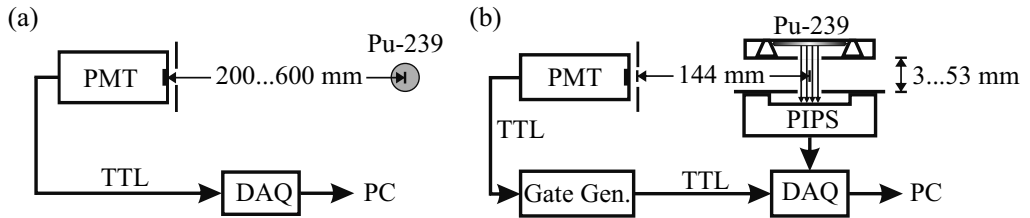


Figure 2.4: (a) Measurement of photon count rate as function of distance from alpha source. (b) Measurement of photon yield as function of alpha particle energy loss. The Figure was originally presented in Publication I.

in the article, but the authors compare their result to a literature value⁶⁷ that refers to 337 nm wavelength.

In 2009 and 2010, yield studies were performed at Tampere University of Technology and the results were 200 and 400 photons per one particle with approximately 5 MeV energy^{20,68}. However, the latter result was due to a mix-up of calibration certificate which lead the authors to believe that the source had an activity of 1.2 kBq while it actually contained 4.2 kBq. This resulted in overestimation of radioluminescence yield by a factor of four. At the same time, Chichester and Watson estimated the the yield is between 20 and 200 photons per particle^{10,69}.

The motivation for further studies on the radioluminescence yield of alpha particles was stimulated by the low number of earlier works and a high variation in results. It was also clear that uncertainties need to be minimized which is best achieved by using conceptually simple experimental setups. Two different methods for the yield measurement were used in the investigations presented in Publication I. The experimental setups are shown in Figure 2.4.

The setup in Figure 2.4a was used to measure photon count rate as function of distance from an alpha source (^{239}Pu , 53.9 kBq, $E_\alpha \approx 5.1$ MeV). Since the radioluminescence photons are emitted in random directions as a result of spontaneous luminescence, it is assumed that the number of photons per solid angle is uniform in the hemisphere, where the source itself does not subtend the emissions. It is also assumed that reflections from the source surface are negligible. Under these conditions, the signal intensity reduces according to the geometrical scaling ($1/R^2$). This relation can be described with equation

$$N_{S+B} = A_S \cdot Y \cdot QE \cdot \Omega + N_B, \quad (2.8)$$

where N_{S+B} is the total pulse count rate (signal and background), A_S is the surface emission rate of alpha source, Y is the number of photons per alpha particle, QE is the detector quantum efficiency, Ω is the geometrical efficiency, and N_B is the detector background count rate.

The photon count rate was measured at ten source-to-detector distance (SDD) values and model, based on Equation 2.8, was fitted to the data. Photon yield Y and background count rate N_B were used as fitting parameters. The latter was included in the fitting due to reflected photons which elevate the detector background, even though the light shielding box had black matte aluminum foil lining the surfaces. The result of the fitting

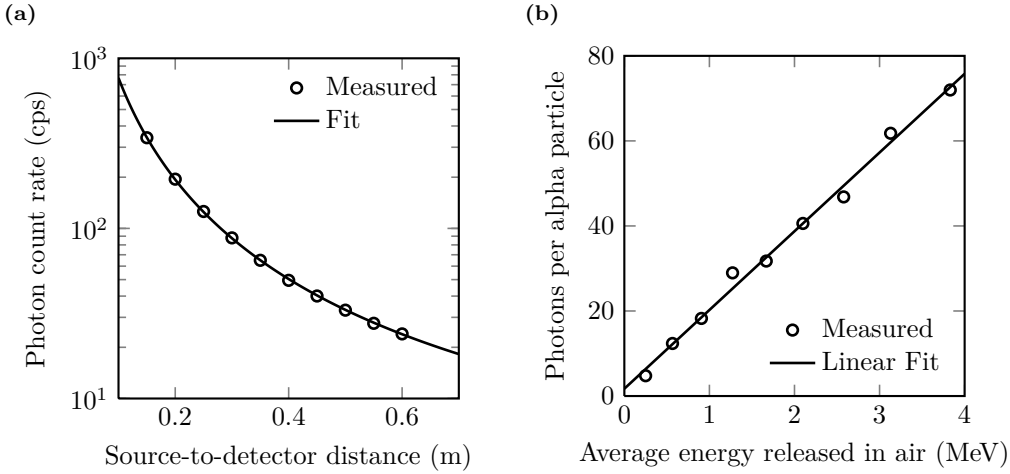


Figure 2.5: (a) Photon count rate as function of distance from 54 kBq alpha source. (b) Photon yield as function of alpha particle energy loss.

was 99 photons per one alpha particle. The data set is shown together with the fitted curve in Figure 2.5a.

The alternative method for the yield measurement employed a coincidence technique. The setup is shown in Figure 2.4b where a passivated implanted planar silicon (PIPS) detector was used to count and measure the energy of incident alpha particles. The UV photons of alpha particles were used as a trigger signal for the alpha spectroscopy system. By measuring the singles and UV-gated alpha spectrum it was possible to estimate the absolute alpha detection efficiency of the PMT. This is related to the photon yield with simplified version of Equation 2.8

$$P = Y \cdot QE \cdot \Omega, \quad (2.9)$$

where P is the alpha particle detection efficiency of the PMT. It is calculated by dividing the relevant area of gated alpha energy spectrum by the same area in an ungated spectrum. This approach removes the alpha emitter calibration from the list of uncertainties. However, background still exists due to random coincidences and the relatively large PIPS detector may reflect photons if not shielded properly.

The energy loss within the field of view (FOV) of the PMT was adjusted by changing the distance between the alpha source and the PIPS detector. The energy loss was calculated using the measured energy spectra and assuming typical Bragg curve behavior, as described in Figure 3 of Publication I. The photon yield is presented as function of energy loss in Figure 2.5b. This plot confirms that the relation of energy loss and photon yield is very linear at these energies. Regression analysis shows that the radioluminescence yield is 18.5 photons per each MeV of energy released in air.

The results of both methods are in reasonable agreement and the average of the two is 19 ± 3 per one MeV of energy released into air in normal temperature and pressure (NTP) conditions. This agreement gives confidence to the methods, but there are certain factors that can have a strong effect on the photon yield estimate. As an example, the yield is always subject to ambient temperature, pressure and humidity. The most pronounced

Table 2.2: Radioluminescence yield of alpha particles in literature.

	Wavelengths (nm)	E_α (MeV)	Photon yield	Gas
Grün & Schopper, 1951 ⁵⁸	300 - 400	5.3	1000	N ₂
Koch & Lesueur, 1958 ⁷⁰	-	4.7	900	N ₂
Duquesne & Kaplan, 1960 ⁹	220 - 520	4.6	60	air
Baschenko, 2004 ⁵	300 - 400	5.1	30	air
Chichester & Watson, 2011 ¹⁰	300 - 400	4-5	20-200	air
Publication I, 2014	200 - 650	1	19 ± 3	air
Thompson, 2016 ¹⁹	1N & 2P bands	1	18.9 ± 2.5	air

effect in indoor applications is expected from humidity due to its natural variation and high quenching constant of H₂O molecules (see Table 2.1).

The effect of humidity was studied with a brief test in Publication I. For the measurement, an alpha source (²⁴¹Am, 13 kBq) was enclosed in an air-tight casing with a UV transmissive window for the observation of photons. This setup was used to measure photon count rate in dry air and in nitrogen in addition to room air. The temperature of the room was 21°C at the time of measurements and relative humidity remained close to 43 %.

In this experiment dry air provided 7 % more signal than room air, while nitrogen produced a signal enhancement by a factor of 6. Since gases are extremely sensitive to even the slightest amounts of impurities, these results serve as general guidelines only. Nevertheless, the test with dry air confirms that humidity has a notable effect on the light yield. The result with nitrogen is compatible with the observations of Duquesne⁹ and Hannuksela²⁰, both reporting a signal increase by a factor of 5 when no special attention is paid to the gas purity or dryness.

The results of other yield studies are presented in Table 2.2 to allow comparison with the current work. The reported values are in agreement to the order of magnitude at best and the differences may be related to calibration issues with detector response or source activity. In contrast, astrophysicists have a good consensus that the light yield of electrons is close to 20 photons per MeV in dry air at NTP conditions^{54–56}. The result of this work (19 ± 3 / MeV) is in agreement with this consensus and actually this could be expected. The reason is that while electrons and alpha particles have different charge, they still produce a swarm of secondary electrons in the media which are primarily responsible for the excitation of radioluminescence emitting molecular states. The difference is that alpha particles deposit their energy in a shorter range because the Coulomb interaction is stronger than for electrons. Yet any saturation effects are not expected because the number of excited molecules remains low in gas phase. This is contrary to solid state scintillators which usually produce less light with alpha particles than with electrons.

Recently, Thomson et al. developed an air fluorescence model using Geant4¹⁹. The model can be used to predict air fluorescence yield of alpha, beta and gamma rays. It considers only 2P and 1N band systems of nitrogen which are the most significant emissions in air. The simulation process starts with the interactions of primary particles and finalizes with quenching and de-excitation. The atmospheric input parameters of the model include ambient temperature, pressure and humidity. Using the same conditions as described in Publication I, a good agreement (within 0.5 MeV per alpha particle) was found between the experimental results and the simulation model. However, the dependance of energy deposition and photon yield was found to be slightly non-linear in the simulated range (0-10 MeV), which is in contrast to conclusions of Publication I. In

any case, the non-linearity is subtle, and does not disqualify the linear approximation for the majority of practical estimations.

There are several ways to improve the measurement of radioluminescence yield. As noted before, the de-excitation mechanisms of radioluminescence emitting states are subject to quenching, and therefore, the ideal measurement would be performed in a large casing that can be stabilized with regard to temperature, pressure and humidity. It would also be beneficial to use an alpha source that contains only one nuclide to reduce fluctuation in particle energy. The experiment also calls for absolute calibration of the PMTs although this can be somewhat challenging⁷¹. A way to mitigate the challenge of detector calibration would be to measure the relative luminescence yield of alpha particles against electrons, which are thoroughly investigated by astrophysicists. A particle accelerator with alpha and electron beam output capability would provide an ideal test bed for this purpose.

3 Surface contamination detection and analysis

Alpha particle detection has a pedigree that dates back to the early 1900s. Therefore, the technology of conventional detectors is well-established and excels in applications where close proximity of an alpha source can be reached. This Chapter introduces conventional alpha particle detection principles and their practical features, but the main emphasis is on the optical detection and imaging techniques which were investigated in Publications II and III of this Thesis. The isotopic analysis of located sources is presented in Publications IV and V by utilizing alpha-gamma coincidence measurements.

3.1 Alpha radiation detection

Thanks to Ernest Rutherford and his students, Geiger and Marsden, it is well-known that scintillations of single alpha particles can be visually seen on zinc sulfide (ZnS) films^{24,25}. Even today, silver-activated ZnS films have a significant role in large-area alpha particle detectors. The popularity is based on their high light-yield and low cost. The material produces more than 10 000 photons per one MeV of absorbed energy¹ and the sensitivity for gamma rays is low if utilized as a thin film. When this material is combined with a light guide to a PMT in an optimal manner, low detection limits can be reached since a detection efficiency of 33 % (4π) is achievable with a background of below 3 cpm⁷². On the other hand, the energy resolution of ZnS scintillation is rather poor and the material is opaque to its own emission. Hence, it is not very useful for alpha spectroscopy.

Another common detection principle is based on ionization of gases. These systems employ chambers in which an electrical potential is used to collect or multiply the charge created by an alpha particle. The applied voltage defines the operation region of the system together with filling gas and its pressure. The systems are categorized as ionization chambers, proportional counters or Geiger-Mueller tubes on the basis of operational characteristics. Each of them have their benefits and disadvantages.¹

Today, semiconductor devices provide numerous solutions for alpha particle detection and measurement. The simplest option is to utilize a commercial photodiode which features a low background and good energy resolution with a very low cost⁷³. However, PIPS detector is a more typical choice for alpha spectroscopy in science. This is a silicon detector especially designed for high energy resolution and large active area. For the most exquisite energy resolution, silicon can even be used in calorimetry configuration as described by Horansky et al.⁷⁴.

Although the alpha particle spectroscopy systems are currently dominated by silicon, scintillation detectors are often used for surface contamination monitoring at decommiss-

sioning sites. As an example, the widely-used Berthold LB 124 series relies on ZnS(Ag) film with entrance window areas ranging from 170 cm² to 345 cm². The popularity of this and other scintillation detectors is related to their moderate cost and large active area which facilitates the screening process. However, the manual labour required to inspect materials with these tools prior to release or final repository incurs major costs to the whole industry.

3.2 Camera imaging

Surface contamination screening with conventional methods is very time consuming, causing an interest towards less laborious radiation imaging systems. However, these systems have rarely been used for radiological characterization at decommissioning sites before this century. Yet the first gamma cameras which comprise a scintillator plate and PMT matrix date back to 1950s^{75,76}. These systems were developed for medical imaging applications, and since then, gamma cameras have become standard tools in the field.

In contrast, alpha imaging was proposed by Imbard and Pineau with a patent entitled “Remote α Source Location Device and Method” as late as in 2001⁷. The patent considers the use of an optical system and a suitable detector as a means to remotely detect alpha radiation. Moreover, the potential for signal enhancement in certain gases is discussed. However, in scientific literature the first demonstration of remote alpha imaging was published by Sergiy Baschenko in 2004⁵. In this study, an UV sensitive film was used to photograph a 37 MBq alpha ²³⁹Pu source from a distance of 30 m in darkness. In addition, Baschenko placed a 185 MBq ⁶⁰Co next to the alpha source to prove that the radioluminescence of air is rather insignificant under gamma irradiation. For this reason, alpha sources can be imaged even under intense gamma fields.

The pioneering, *in situ* alpha imaging experiments at nuclear installations were reported by Lamadie et al. in 2005⁶. As noted by the authors from Commissariat à l'énergie atomique et aux énergies alternatives (CEA), the need for an alpha camera arises from practical experience on decommissioning work with actinides*, which are hard-to-detect with gamma cameras due to their low gamma yields. Hence, alpha imaging can be regarded as a complementary technique for gamma imaging.

Lamadie et al. used a scientific-grade charge coupled device (CCD) camera in darkness in the study. The main implications of the work were that UV cameras can be used to detect alpha contamination at nuclear facilities and images can be taken through translucent materials to inspect e.g. gloveboxes. The camera was able to detect contamination levels down to few hundred Bq/cm² in laboratory environment with an exposure time of five hours. In field experiments, the performance was sufficient for the observation of MBq activities through 10 mm of plexiglass with a 600 s exposure time. The authors concluded that the limits of detection are dependent on the level of darkness that can be achieved in the field.

The continuation of alpha imaging work at CEA was described by Mahé et al.⁷⁸⁻⁸⁰ In these proceedings, the CCD camera was replaced with an intensified CCD (ICCD). The new approach also included image acquisition by frame summing (25 Hz rate) instead of a single exposure of desired length. Further development was the testing of interference

* Actinides are metallic elements with atomic numbers from 89 to 103. Natural uranium and thorium are part of the group but the majority of actinides are synthesized via nuclear transmutation. Typically actinides decay by alpha emission and all of the elements are radioactive and -toxic.⁷⁷

filters to suppress background light, but their performance was found to be insufficient to enhance detection under illuminated environment. In overview, these reports show insightful examples of glovebox characterization and real time monitoring of a clean-up process with optical techniques.

Very advanced systems for stand-off detection have been developed by Bubbletech Industries in Canada approximately at the same time with Baschenko and CEA. Their long range imager comprises six ICCD cameras and it was featured in CBRNe World magazine in 2006⁸¹. The article shows that high alpha activities can be detected with this system at distances of several hundreds of meters and even beyond 1 km. The company has also developed a wide field alpha imaging system which suits decommissioning and crime scene investigation purposes^{82,83}. Likewise to the long range imager, this system exhibits a high technology readiness level. However, the filter performance imposes a limitation to its application under illumination⁸⁴.

The motivation to develop sophisticated optical systems may arise from the need to detect special nuclear materials (SNMs)[†] from a distance. This capability would be useful for combating illicit trafficking of these materials and the passive observation of their secondary signatures could be an elegant approach for this purpose. This was proposed by Seidler et al. in patent application in 2002⁸⁶. The indirect detection of SNMs at stand-off was also addressed in US Defense Advanced Research Projects Agency call in 2009⁸⁷. These applications do not target detection of alpha radiation but rather the radioluminescence effects of neutrons and gamma rays in the atmosphere. Hence, the physical principles are similar as with alpha particles, but the practical challenges are even greater due to low local ionization yield. It is worthwhile to note that the long range of optical photons is the major motivator for these approaches, despite the low conversion efficiency.

The optical detection of alpha and gamma sources has been investigated in the recent project of Sandia National Laboratories⁸⁸. One of the motivations in this three-year long project was to improve long range radiation detection capabilities to benefit post-detonation nuclear forensics applications. The report contains a comprehensive collection of experiments indoors and outdoors with both alpha (MBq range) and gamma (TBq range) radiation sources. The images were acquired by using electron-multiplying CCD (EMCCD) and CCD cameras. The successful demonstrations of gamma source detection via radioluminescence of air are few in numbers, and in this work, a 150 Ci ⁶⁰Co source was imaged at 75 m distance with 1 h exposure. The report concludes by endorsing hyperspectral techniques to improve confidence levels in the detection.

The interest towards alpha imaging can also be identified in nuclear safeguards. In this field, alpha imaging could have potential in verification and sampling of plutonium work. Specifically, imaging could verify declared work activities and even identify some undeclared work activities as suggested by Chichester et al.⁸⁹. Furthermore, swipe sampling is in central role in safeguards and it is essential that samples are taken from spots which are abundant with actinides. With further development optical systems may find use in pinpointing the best sampling areas, and in this way, the risk of taking a sample with practically zero activity would be significantly reduced. This would incur savings in operational costs of regulatory bodies because each sample needs to be treated as an evidence material, requiring careful transportation and handling.

[†] The most important SNMs are plutonium and uranium enriched in the isotope 233 or in the isotope 235⁸⁵.

An interesting application of alpha imaging could be the verification of nuclear warheads. Jessica Feener has investigated this in her PhD Thesis⁹⁰ and published a number of proceedings about the results⁹¹⁻⁹³. The aim of the work was to investigate if radioluminescence imaging can be used for verification of warheads, and secondly, if the technique can reveal sensitive information about these components. The discussion is centered around uncanned warheads which directly expose fissile material to air and thereby enable radioluminescence imaging. The conclusion of the work is that highly enriched uranium turns out to be too weak of an alpha emitter to reveal any detailed warhead designs. On the other hand, alpha yields of fissile plutonium are much higher, but these were not thoroughly investigated during the course of work. Hence, further experiments would be needed to ascertain the achievable amount of image detail in this case.

In Publication II of this Thesis, the detection performance of alpha imaging cameras was investigated by using three different technologies in relevant test environment. The cameras used were iXon3 897 and iStar 320T, both manufactured by Andor Corporation. iXon3 is an EMCCD camera which uses on-chip signal multiplication to enhance the signal before analogue-to-digital conversion. This helps to overcome the noise floor caused by readout process to detect very low light levels. The camera also has the conventional CCD readout amplifier which allows comparison of these technologies by using the same instrument. iStar is an intensified camera and it utilizes the photoelectric effect for the initial conversion of a photon. Hence, the operation principle is analogous to a PMT, but an ICCD sensor has a pixelated (microchannel plate) signal amplification. The readout is achieved by converting the electron burst into light by a phosphor screen which is optically connected to a CCD sensor. All of the aforementioned camera types have been previously employed for alpha imaging and here they are compared side-by-side in a field test.

The camera images shown in Publication II and in this Thesis were acquired with light shielding in darkness, which helps to maximize the UV signal level. On the other hand, the use of filters to allow imaging in an illuminated environment is desirable but not feasible in practice. This is due to the fact that the cameras have a wide spectral response from UV to IR wavelengths and achieving sufficient blocking level in this wide range poses a challenge for absorptive filters. However, single interference filters were used during the work to enhance signal-to-background ratio (SBR) in some experiments where imaging was limited by optical background permeating through the light shield.

The established approach to alpha image processing with high resolution cameras was introduced by Lamadie et al.⁶. Briefly, this method is based on the superimposition of an alpha UV image and a visible light image, which provides a visual localization of alpha activity. The image processing steps used in this work are presented in Figure 3.1 with an EMCCD image of a mixed oxide (MOX) fuel pellet. The UV image was acquired with 100 s exposure with electron-multiplying (EM) gain of 300. The first image processing step is to remove the bright spots created by gamma rays and cosmic particles. The second step is to apply a low pass filter to smoothen the image. Finally, the processed UV image is superimposed on a daylight image, captured with the same camera. The underlying daylight image is in grayscale while the UV image is in appropriately scaled color map.

The experiments were performed at the Institute for Transuranium Elements (ITU) in Karlsruhe, Germany. ITU is a nuclear research institute of the European Commission and it has access to many radioactive and nuclear materials that are not commonly available elsewhere. At ITU, the materials are handled either in gloveboxes or shielded cells

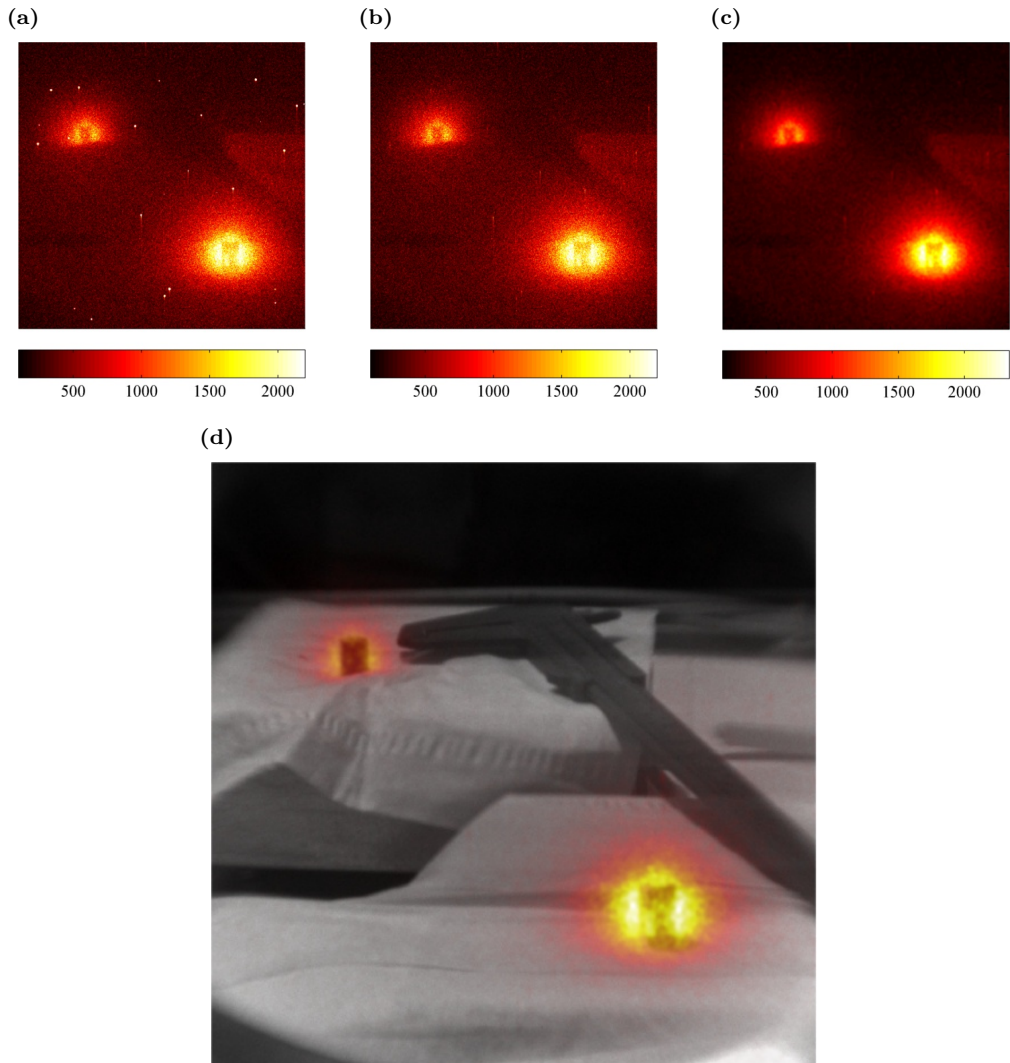


Figure 3.1: Two MOX fuel pellets imaged in glovebox with EMCCD camera. The image processing steps are as follows: (a) the original UV image with 100 s exposure in darkness, (b) the spots of gamma rays are removed, (c) a low pass filter is applied, (d) the UV image is superimposed to a visible light image.

which are also known as “hot” cells. Gloveboxes are used to provide physical protection and separation of the hazardous materials while shielded cells have additional radiation absorbing glasses that are designed to stop gamma rays.

Publication II describes the imaging of alpha active samples in a glovebox. The imaging was performed through a quartz glass window to enhance the transmission of UV light. The plexiglass used in ITU gloveboxes allows transmission down to 360 nm, and therefore, the special window is not mandatory for these experiments. However, the broad transmission of quartz allows the whole nitrogen emission spectrum to be used for the detection.

Considering that the glovebox is not originally designed to be light-tight, it was quite tedious to darken the box completely for alpha imaging. The light shielding was done by carefully covering the glovebox with black rubberized fabrics (BK5, Thorlabs). Practical challenges arose not only from covering every joint and fold of the fabric with black tape, but also from making sure that light does permeate through the fabric itself. In the final stage before experiment, the box was covered with at least two layers of fabric, but still the imaging was limited by optical background within the box.

The main results of Publication II can be summarized to three key points. First, the imaging of MBq level alpha activities is feasible by applying a light shield to a standard glovebox. The use of a quartz window for viewing enhances detection but is not mandatory (see Figure 3.4) with this glovebox. Second, the ICCD camera provided the best detection performance in the field test. Thirdly, filters can be used to improve selectivity for UV light and pixel binning helps to enhance signal to noise at the acceptable cost of image resolution. These main results are also described in the figures of Publication II.

In addition to the glovebox experiments described, the camera system was utilized for the imaging of hot cell facilities at ITU. These are used for the handling of highly active materials and irradiated fuel. The cells are heavy installations with vast amounts of concrete and steel, and therefore, they are inherently more light-tight than gloveboxes. The viewing into a cell takes place through thick lead glass windows that usually have yellow appearance resulting from poor transmission in the UV and blue region. In addition, the last barrier of modular cells is made of plexiglass to keep all active material within the module.

Radiation shielding glasses typically exhibit a cut off at 400 nm wavelength^{94,95} which dictates that the imaging needs to be performed at the visible region. Figure 2.3 shows that there are some emissions that could be used for the purpose. Despite the expectation of significant optical losses, feasibility tests were performed with the same instrument configuration as in the glovebox experiments. The preparation of the experiments was now more straightforward since only the cell window required shielding for external light.

Two different hot cells were imaged for alpha activity. The first cell is used for fuel fabrication and it contained approximately 10 mg of ²⁴¹Am in a glass crucible, which could be used as reference point. The exposure time was 5 min for the image shown in Figure 3.2a. This substantial amount of ²⁴¹Am is clearly visible in the image even though light leaks from the ceiling of the cell severely hinder the detection. Despite the positive detection of ²⁴¹Am in the crucible, the optical background is clearly too high for a practical contamination screening application in this cell.

The second cell was a part of post-irradiation examination facility and it was previously used for polishing of spent fuel. Thus a widespread contamination could be expected within. The imaging was performed as before, but with an extended acquisition time of 60 min. The result is shown in Figure 3.2b where one hot spot at the back of the cell and a bottle clearly show signs of radioluminescence. Moreover, the back wall shows some faint signs of light emission which could well be explained by contamination. As before, the visible points represent only the highest activities.

Figure 3.2c demonstrates a scenario related to nuclear security. For this test, an improvised laboratory was staged in a room at ITU. Two alpha sources (²⁴¹Am, 13 MBq and 37 MBq) were contained in quartz bottles and placed alongside other items on the table. Again, the superimposition of a daylight image and UV image clearly revealed the location of open sources. The total exposure time was 5 min for the UV image with EM gain of

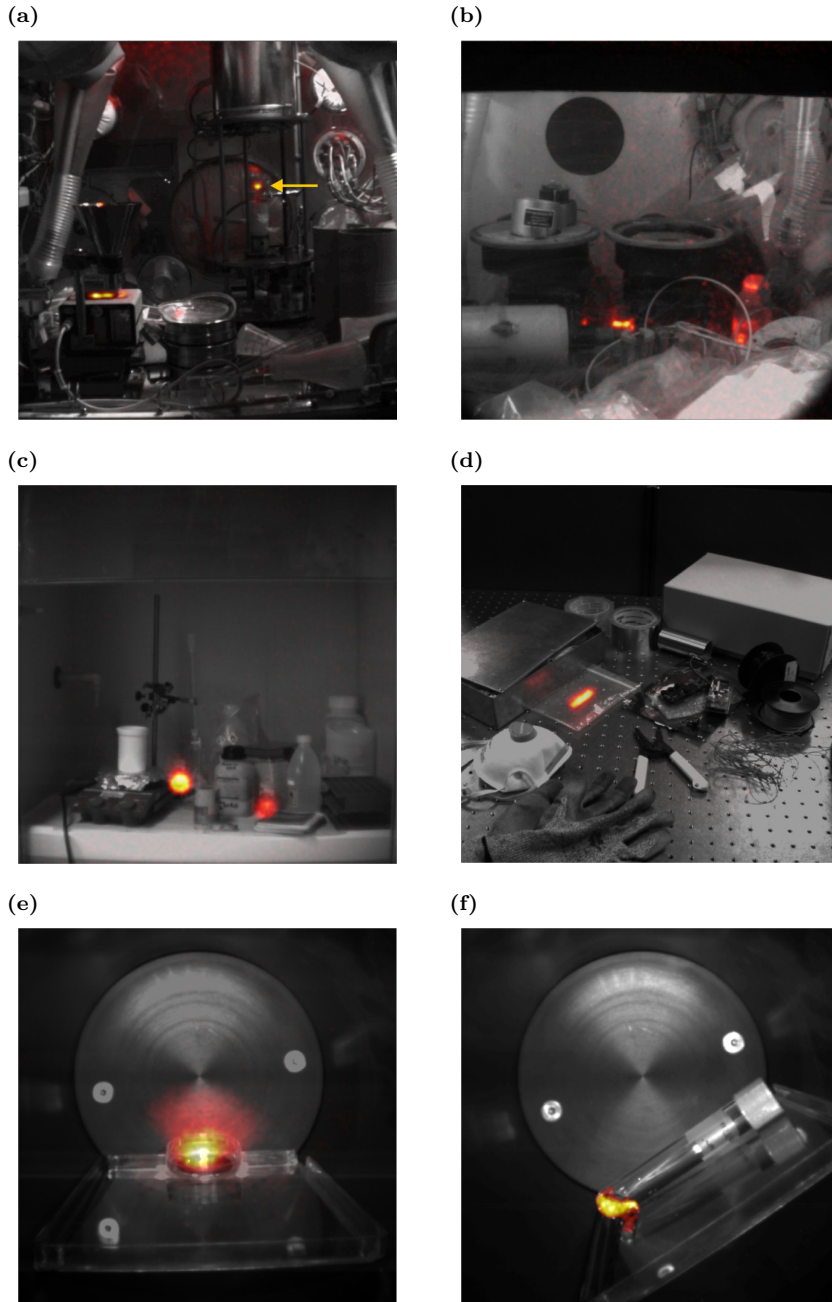


Figure 3.2: (a) Shielded cell for fabrication of fuel pellets. Macroscopic amount of ^{241}Am is visible in a glass crucible (arrow). All other spots are either light leaks from above or instrument's lights. (b) Hot cell facility for the analysis and polishing of irradiated fuel. Hot spots and a contaminated bottle can be identified. (c) Demonstration of crime-scene alpha imaging scenario. ^{241}Am alpha sources (37 MBq and 13 MBq) are packed in quartz vials and seen as two bright spots. (d) Additional crime-scene alpha imaging demonstration with 32 MBq ^{241}Am stripe. The image was acquired with a conventional telephoto lens at TUT. (e) Imaging of a 5.6 MBq ^{239}Pu planchet and (f) an alpha active solution, both in a glovebox-integrated light-tight chamber. The color maps are scaled for each image separately.

300. However, the sources could be detected with 1 min exposure if needed. The light shielding was performed by covering the door frames with tape and a very good level of darkness was achieved with minimal effort.

Figure 3.2d is another example of crime scene imaging. The special feature of this image is that it was taken with a conventional telephoto lens (Cosmicar No. 84611, 12.5 mm, F/1.4) which is not designed for use with UV light. For this reason, the UV image is formed only by the emissions at around 400 nm wavelength. However, the wide aperture of this lens compensates the losses and allows the imaging of a 32 MBq source in 100 s time. Based on the result, it is probable that this lens would have worked well for the scenarios shown in Figures 3.2a and 3.2b.

Figures 3.2e and 3.2f show alpha imaging with a dark chamber that is integrated to a glovebox. The design enables rapid and safe sample manipulation through the back lid of the chamber. Also, an excellent darkness level is achieved without the need for tape seals in the glovebox. In Figure 3.2e, a 5.6 MBq ^{239}Pu sample is placed in the chamber and imaged with 200 s exposure. The imaging was repeated with four similar samples and the analysis is shown later in this Chapter.

In Figure 3.2f the alpha emitter (plutonium) is dissolved in nitric acid solution. The light emission of this solution is an unexpected result and it was observed both in a plastic bottle and in the quartz vial shown here. The light could be generated in the solution itself or at the container surface. Some observations of light emission from glass under alpha particle irradiation can be found in literature⁶⁰, and also, a light yield of few photons per alpha particle in water was reported by Duquesne⁹. More recently, Yamamoto et al. reported observations of light emission by alpha particles in water using an EMCCD camera⁹⁶. Yamamoto suggests that the light is emitted by radicals created in water by alpha irradiation and the light yield is much lower than with air.

The dark imaging chamber shown in Figure 3.2e was not available at the time of measurements for Publication II. This chamber enables imaging with nearly non-existent optical background which is beneficial for the investigation of detection limit defined by the camera instrument itself. This was briefly studied with the EMCCD camera and the plutonium planchettes used in Publication II. The results of 300 s exposure times with these samples are shown in Figure 3.3a. The average signal level is shown as function of planchet activity together with the corresponding signal to noise value in Figure 3.3b. The signal is calculated as a mean of pixels in a rectangular area that fits the whole scintillation hemisphere. The noise is the standard deviation of pixels in a no-signal-area of each image. The experiment confirms that this lens and camera combination can detect MBq sources and the relation of UV signal and alpha activity is linear.

In conclusion, the detection capability for MBq level alpha sources in a glovebox was demonstrated with different camera technologies. This result and the experience that optical background limits the detection in-field are consistent with the studies conducted at CEA earlier. The fieldwork showed that light shielding of gloveboxes is a painstaking process which would be hard to translate into standard operating procedure. However, a specific imaging room could be established at sites where there is a large number of gloveboxes at the end of their service lives. In the case of shielded cells, the situation is better since the cells are often inherently light tight and only the window requires covering.

The camera imaging experiments of this work represent a technology demonstration which can be significantly enhanced. For operative use, the light shielding of the gloveboxes

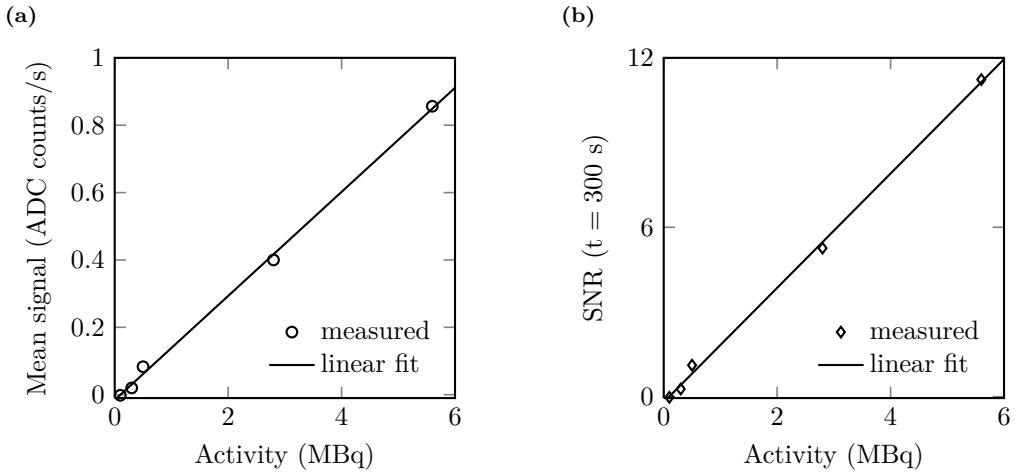


Figure 3.3: (a) UV signal as a function of ^{239}Pu activity on planchet. The images were acquired with the setup shown in Figure 3.2e, using EMCCD camera with exposure time of 300 s and EM gain of 300. (b) Signal-to-noise ratio of the measured signal levels.

should be standardized to reduce the time required for preparations. The technological improvements can include camera objectives with higher light collection capability, which is achieved by lowering the f number and by increasing the diameter of the lens. Moreover, the physical size of the camera sensor used was very small (8.2 mm x 8.2 mm) and therefore it limited the FOV. For comparison, most digital single reflex cameras have sensor dimensions of 25.1 x 16.7 mm (APS-C format). In this sense, ICCDs have a slight competitive edge over EMCCDs since large sensors are more readily available. In terms of sensitivity, the ICCD camera was found to provide slightly better SNR than the EMCCD camera. In light of these points, the ideal camera for alpha imaging is based on ICCD sensor.

It is important to note that the images presented in Publication II were acquired through a quartz window which enhances the transmission of UV light. In operative scenarios, quartz glasses are not available without special preparations and it is likely that gloveboxes would be imaged through plexiglass or even lead glass. This attenuates deep UV emissions and forces the use of detection wavelengths close to 400 nm or above. This has some implications for practical work. First, it is not mandatory to use UV objectives since many commercial lenses provide sufficient transmission at the blue edge of the visible range. This reduces the lens cost significantly. Second, the silicon-based CCD sensors have excellent quantum efficiency (QE) at above 400 nm wavelengths, and therefore, those may provide better performance than ICCD cameras. Also, the availability of high performance optical filters is very good for these wavelengths.

Figure 3.4 shows the transmission properties of two plexiglass types. The first sample is manufactured by Röhm AG and it is widely used for gloveboxes at ITU. Premac is a trade name for plexiglass that has been added with lead to enhance absorption of gamma rays (manufactured by Wardray Premise Ltd). The transmission of this material is shown for two thicknesses (12 mm and 35 mm). The convolution of nitrogen spectrum with transmission curves suggests that ITU sample transmits 18 % of the total radioluminescence light while the thinner Premac transmits 7 %. Sometimes Premac is

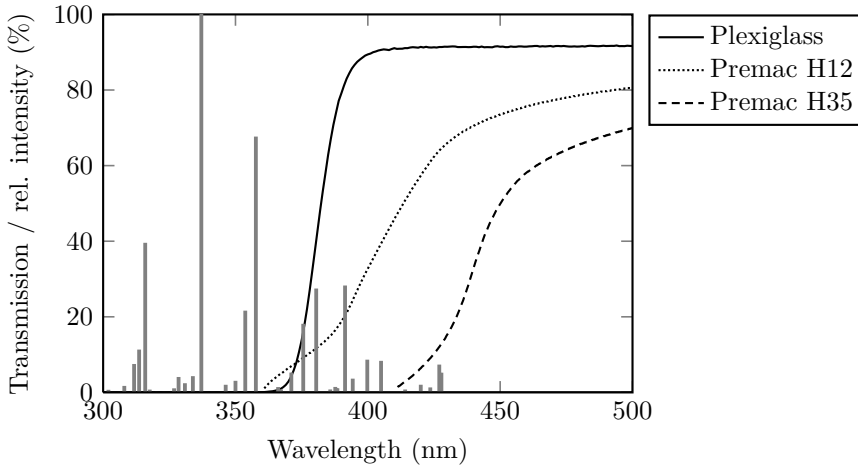


Figure 3.4: Optical transmission of plexiglasses that are typically used for gloveboxes. The curves are shown for standard plexiglass (Röhm AG) and two different thicknesses of Premac (Wardray Premise Ltd) which has added lead to enhance absorption of gamma rays. The transmissions of Premac are based on vendor specification while Röhm plexiglass was measured with a spectrophotometer. The most important nitrogen band heads are shown as in ⁹⁷.

used in conjunction with other materials which provide additional physical protection and this can further reduce transmission. With regard to heavily shielded cells, lead glasses are usually thicker and have even lower anticipated transmission than the materials shown here. It is not possible to estimate the transmission properties of gloveboxes in general and usually it is best to confirm feasibility with onsite testing.

3.3 Telescope scanning

Telescopes are used to observe remote objects with a narrow FOV. They are built using either reflecting or refracting components. In optical alpha particle detection, the radioluminescence signal decreases with the well-known geometric scaling ($1/R^2$). Therefore, it is obvious that detection at very long distances is only possible if geometrical losses are compensated by increased source activity. However, telescopes may find use also at shorter ranges where the narrow FOV can be used to detect and localize sources without the need for image formation.

A simple stand-off alpha particle detector can be constructed from a telescope objective, PMT and a suitable filter. This design concept has been used in some of the first demonstration systems^{20,68,98,99}. The popularity of the approach is further justified by low weight and cost of components. On the other hand, it does not allow the screening of a large area with single exposure which is one of the key arguments for alpha imaging. The central point of the trade-off is that a telescope collimates light by design. This allows simple utilization of interference filters which are designed to operate at normal incidence. Moreover, since image formation is not necessarily required, the number of interference filters can be increased without considering distortions which arise from multiple reflective surfaces. The goal of these developments is to create a system that can be effectively operated in an illuminated environment.

Hand-held alpha UV application (HAUVA) device was developed at TUT during 2009-2010. It uses the aforementioned approach to detect radioluminescence light under artificial light. The key feature of HAUVA is that the optical signal is split with a polka-dot beam splitter into two channels. The first channel measures the number of photons within the whole passband (300-340 nm) and the second channel observes only a narrow band close to 300 nm for background estimation. With this principle it is possible to perform background reduction and reveal the amount of true signal, provided that the characteristics of background spectrum are well-known. However, this detection principle would significantly benefit from custom filters which were not available at the time of development. The main lesson from the work was that multiple interference filters are needed to enable radioluminescence detection in an illuminated environment. In terms of detection performance, HAUVA is able to detect >10 kBq alpha sources from 50 cm distance with few seconds integration time, but detailed analysis is not available. It is tolerant for light-emitting diode (LED) lamps, but any fluorescent light raises background level to several hundred counts per second (cps) and beyond.

The development of HAUVA type detection system was continued in Publication II by targeting even higher tolerance for visible light. In other words, the best compromise between light tolerance and sensitivity was experimentally investigated. Again, the goal was approached by stacking interference filters to create a solid rejection of visible light while maintaining good transmission for the selected signal band. Two different filter sets were developed to address the specific challenges of different lighting environments. Under UV-free lighting, the main emission peaks of nitrogen can be used to achieve high signal count rates. Examples of this lighting include LEDs, fluorescent lights with superb UV filters, and low pressure sodium lamps. On the other hand, the typical illumination in an industrial installation is white fluorescent lighting and the lamps cannot always be shut off or replaced to facilitate optical alpha detection. Therefore, it was necessary to seek solutions for this environment as well.

When near UV region is free from significant background light, a good choice for detection wavelength is 337 nm since it has the strongest emission peak (see Figure 2.3). Moreover, this peak is away from visible region which is beneficial because the spectral output of light sources generally reduce towards short wavelengths. Typical pass bands of interference filters could simultaneously cover several nitrogen emission peaks to collect a maximal portion of the radioluminescence signal. However, in this case any overlapping light sources could rapidly accumulate background level since their spectrum is often continuous. Therefore, a decision was made to minimize the width of the pass band for near UV detection.

The narrow pass band for 337 nm wavelength was implemented using three interference filters (FF01-340/12-25 and 2 x FF01-335/7-25, Semrock Inc). The number of filters is a trade-off between signal band transmission and rejection band blocking. Moreover, additional filters do not have any effect on the SNR ratio within the signal band. Absorptive filters could not be considered for the purpose since narrow and steep pass bands are difficult to achieve with this technology. Also, achieving a high off-band rejection ratio usually requires a thick absorptive layer.

Finding a wavelength that would allow optical alpha particle detection under white fluorescent light is a challenge. This is demonstrated in Figure 3.5a where the measured emission spectrum of typical fluorescent light (Master TL-D 830, Philips) is shown. The spectrum consists of sharp peaks together with continuous emission that extends down to 300 nm wavelength. It is likely that the continuum emission arises from a delayed

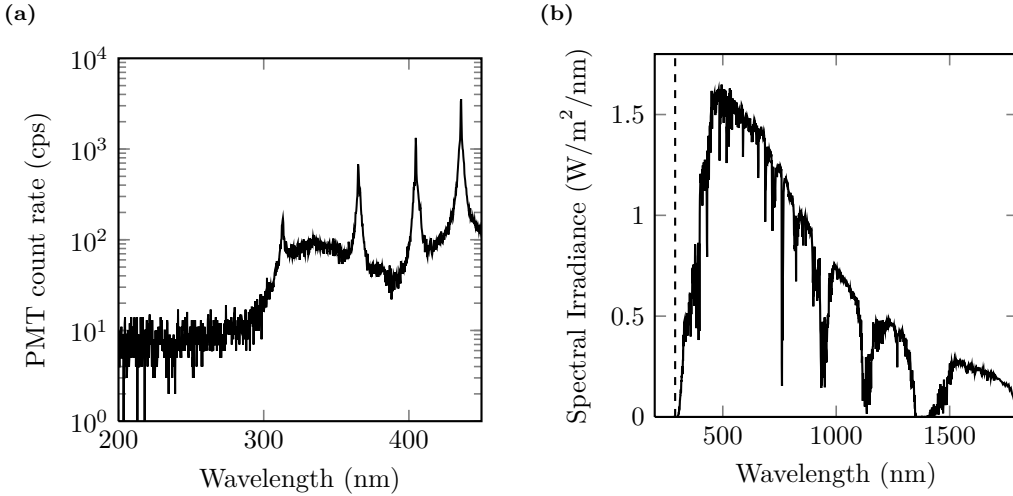


Figure 3.5: Spectra of typical light sources which are very challenging for optical alpha particle detection: (a) white fluorescent light and (b) solar light at ground level. Both prevent the use of near UV region for radioluminescence detection but also cut off at 290 nm wavelength (vertical dashed line in (b)). The spectrum of the lamp was measured with monochromator and the solar emissions are shown as in ASTM G173-03 reference spectrum⁴⁸.

fluorescence process of the phosphor and it leaves little room for optical alpha detection in near UV region. Fortunately, rigorous experimental work revealed that there are very weak emissions at below 300 nm wavelength which can be used for detection in most environments. The best results were reached using filters with pass band close to 260 nm (3 x FF01-260/16-25, Semrock Inc). An extensive collection of other typical background spectra is available in the dissertation of W.C. West, entitled “Background UV in the 300 to 400 nm region affecting the extended range detection of radioactive material”¹⁰⁰.

The total response of a photon counting system results from the combination of filter and detector characteristics, and therefore, careful selection of detector response can further reduce unwanted background signals. The response of an optimal detector would roll off towards long wavelengths immediately after signal band. For measurements at 337 nm wavelength, this could be achieved with novel gallium-nitride (GaN) photocathodes. However, only image intensifiers are currently available with this cathode and there is no information on typical background levels. Hence, an ultra bi-alkali photocathode was selected for near UV detection. Its QE exceeds 30 % at UV wavelengths but unfortunately the response also extends to 700 nm. This photocathode type is mostly available with a diameter of 8 mm and the PMT model selected was H10682-210 (Hamamatsu).

For measurements at 260 nm wavelength, it is possible to use a cesium telluride (CsTe) photocathode which is sensitive to below 320 nm wavelengths. This type of PMT is often described as “solar blind” detector, meaning that it is not sensitive to sunlight. However, this operational capability is only achieved in combination with a suitable filter because solar radiation extends down to 300 nm wavelength (see Figure 3.5b). The PMT selected for this purpose (H11870-09, Hamamatsu) was equipped with 21 mm diameter photocathode and quantum efficiency of 13 % at the signal wavelength. The filter stack

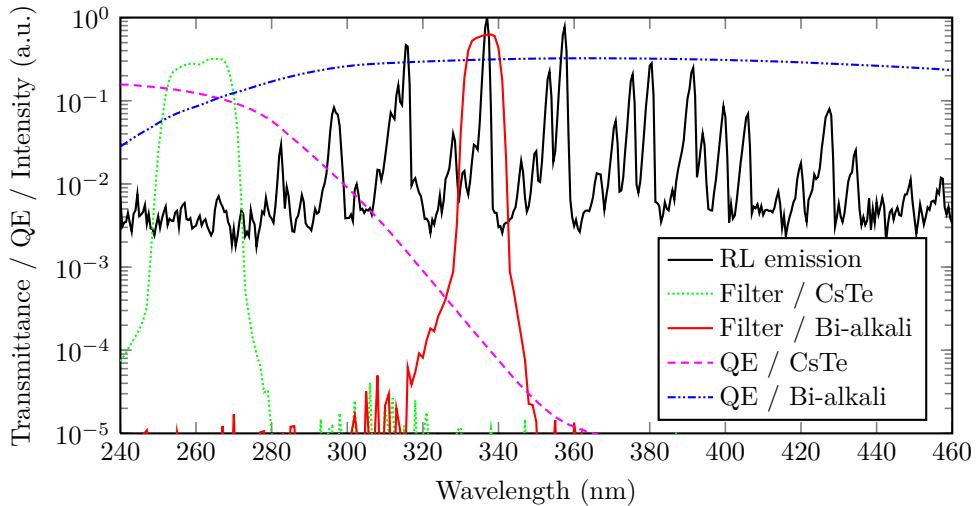


Figure 3.6: Transmission spectra of filter stacks and QE curves of the PMTs utilized in the radioluminescence mapping device. The transmissions of the filter stacks are based on experimental verification with a spectrophotometer (UV-3600, Shimadzu Corp.) while the PMT curves are reported as in manufacturer specifications.

transmissions and photocathode quantum efficiencies are shown in Figure 3.6 together with the radioluminescence spectrum.

The telescope was designed using the Galilean approach in order to keep the device as compact as possible. The goal of the design was to maximize light collection from a single point source and the work was initiated with ray-tracing software (FRED) while the final assembly was optimized on an optical bench using radioactive sources. The telescope objective is a 100 mm diameter lens and the optical components were selected on basis of availability (i.e. most are COTS components). The current design leaves room for later optimization, but performs well in demonstrating the capabilities of the approach. Beam splitting was not performed to separate signal from background which means that the system was operated as simple counting detector. However, it is clear that a well-designed background measurement would enhance the reliability of the detection.

In contrast to HAUVA, which was designed for hand-held operation, the new telescope assembly was mounted on a motorized pan-tilt head which was fixed on top of a tripod. This enables automated screening of surfaces without the need for operator presence during measurement. The device is shown in Figure 3.7 without the peripheral devices, which include a data acquisition card, laptop, and power supplies. The small camera on top of the telescope is used to record visible light images of the scene.

For the experiments described in Publication III, the pan-tilt head was programmed to scan a user-defined area with 1° steps. This allowed some overlap for adjacent points since the FOV of the telescope was 3.4° with the CsTe and 2.5° with the ultra bi-alkali photocathode. This difference arises from the different diameters of the photocathodes used. The scanning was performed on a point-by-point basis, which is time consuming but enables straight-forward analysis of the results. The grid of overlapping scan points was interpolated to create a continuous contamination map. The interpolation was performed using interp2 function of Matlab with 'cubic' option and 0.25° grid resolution. The



Figure 3.7: Radioluminescence mapping device.

outcome is similar to images acquired with cameras in the previous Chapter and can be overlaid with an visible light image. In the future, this should be replaced with 3D scanning that also considers the changes in detection distance.

The time required to scan a certain surface depends on the size of the area, scan resolution, and acquisition time. The movement and settling of the pan-tilt head from one point to another takes few seconds. The acquisition time t sets the minimum detectable activity (MDA) according to Currie's definition¹⁰¹ ($\alpha = \beta = 0.05$)[‡]

$$MDA = \frac{L_D}{N_s t} = \frac{2.71 + 4.65\sqrt{N_b t}}{N_s t}. \quad (3.1)$$

Here, N_s and N_b are the signal and background count rate, respectively. The detection limit applies for paired observations where signal and background are measured using the same acquisition time. The signal count rate is expressed in counts per time unit per alpha activity. In this work, all scans were performed using 10 s acquisition for each point.

The calibration of the telescope system was performed at ITU using ^{239}Pu and ^{241}Am samples. The activities ranged from 100 kBq up to 36 MBq. The count rates observed with the two different nuclides were scaled to equal alpha particles with 5 MeV energy. This enabled the analysis of signal count rate as function of source activity which is needed for the MDA calculation. The results are shown in Figure 3.8. According to linear fitting,

[‡]According to Currie's definition, α stands for the probability of false positive (type I) error and β for the probability for false negative (type II) error. L_D is the net signal level which can be *a priori* expected to lead to detection.

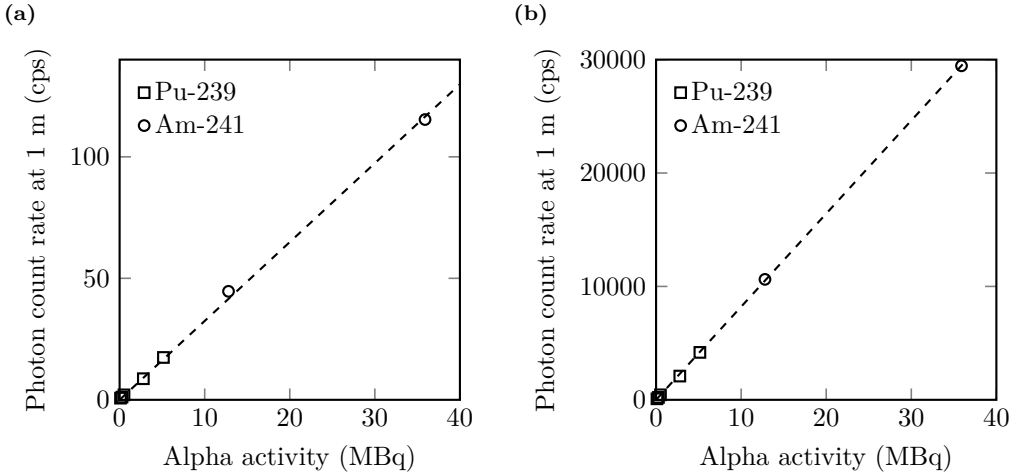


Figure 3.8: Performance calibration of the telescope with (a) CsTe and (b) bi-alkali PMTs. The count rates are scaled to equal alpha particles with 5 MeV energy.

Table 3.1: MDA estimates at 1 m distance in 10 s time.

	Air	Nitrogen	Argon	
Bi-alkali (330-340 nm)	4	0.4	-	<i>kBq</i>
CsTe (250-270 nm)	800	6	2	<i>kBq</i>
Bi-alkali (330-340 nm)	0.3	0.03	-	<i>kBq/cm²</i>
CsTe (250-270 nm)	30	0.2	0.07	<i>kBq/cm²</i>

Table 3.2: Relative signal enhancement in N₂ and Ar.

	Nitrogen	Argon
Bi-alkali (330-340 nm)	10	< 0.2
CsTe (250-270 nm)	150	420

the CsTe has a sensitivity of 3.2 cps/MBq while the bi-alkali exhibits 820 cps/MBq at the cost of higher sensitivity to visible light. These numbers form the basis of MDA calculation shown in Table 3.1.

This table shows the MDAs in nitrogen and argon in addition to air. The numbers are based on the measured relative signal increases shown in Table 3.2. The tests were performed at TUT with the gas-tight casing that was also applied in Publication I. It should be emphasized that these multiplicative enhancement factors are strongly dependent on the measurement bands which were defined by the used filter stacks in this case. Furthermore, gas purity and residual humidity can have a drastic effect on the results. Here, the gas chamber was simply flushed with the gases which best reflects the situation in industrial applications. In conclusion, argon and nitrogen provide significant enhancements to solar blind detection of alpha radiation, and importantly, they are used as a shielding gas for certain processes in the industry^{102,103}.

An example of the radioluminescence mapping is shown in Figure 3.9. This experiment was performed at ITU in a laboratory room that could be sealed from external light if necessary. Two ^{241}Am alpha sources (13 MBq and 36 MBq) were used in this demonstration. In addition, two control samples were used to rule out false positives due to reflection of background light. The first control was a circular plate of Spectralon which has a very high reflectivity from UV to IR wavelengths¹⁰⁴. The second control sample was a zero-activity planchette in a quartz vial.

The lighting conditions of the experiment were selected to illustrate the light tolerance of the system. Figure 3.9a shows the experiment with CsTe PMT under white fluorescent light and 3.9b with the bi-alkali PMT under white LED bulb (5W). In both cases, the sources are easily resolved from the background, which consists of intrinsic detector background, reflections, and to a lesser degree, from background light. The negligible contribution of visible light is confirmed by the Spectralon reflection standard which is not resolved in either of the experiments. However, the vial with the blank source is visible in Figure 3.9b. The probable reason is reflected radioluminescence light that originates from the alpha sources. The same effect is not observed with the Spectralon plate as it is located in front of the sources.

The maximal detection range and applicability of this technique is defined by three main factors:

- Photon flux created by the source
- Optical background at the detection band
- Intrinsic detector background

The first depends on the source activity and its surface characteristics. It is also subject to geometrical scaling where signal level is inversely proportional to the square of the detection distance. This can be somewhat compensated by using large collection optics, but the radius of the input lens needs to grow linearly with the detection distance to balance out any increase in detection distance.

The optical background is defined by ambient lighting. Practically any lamp whose spectrum overlaps with detection wavelength renders the method incapable to detect even moderate activities. Therefore, a more typical challenge is that light in the stop band affects the system so that background levels increase. If the intrinsic background limits the detection, it may be beneficial to consider cooling systems which can reduce the thermal background of detectors.

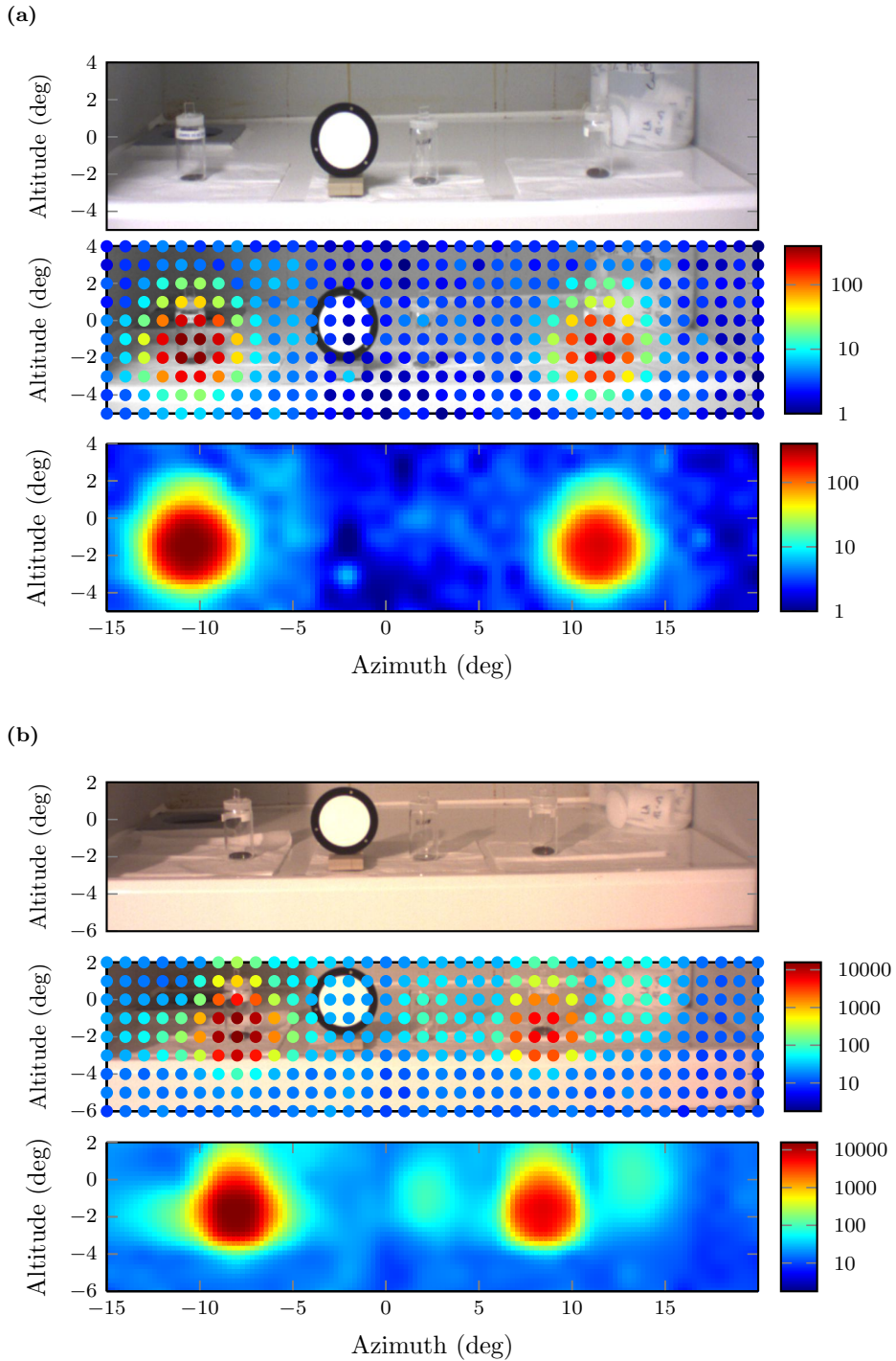


Figure 3.9: Radioluminescence mapping of ^{241}Am samples in quartz vials. The leftmost sample has an activity of 36 MBq while the rightmost has an activity of 13 MBq. The distance between the telescope and samples was 1 m. Figure (a) shows the experiment under normal fluorescent light using CsTe photocathode while (b) is acquired under LED light with bi-alkali photocathode PMT. The measured points and the final interpolated map are presented for both cases.

3.4 Alpha-gamma analysis

The two preceding sections describe how alpha active materials can be remotely detected by radioluminescence imaging and photon counting. However, these techniques cannot identify different radionuclides without prior knowledge on substances present at the site. The number of radioluminescence photons created by an alpha radiation source depends on the particle energy, self-absorption, and activity of the source. The isotope identification would require knowledge on how many photons are created per particle, but given the unknowns and uncertainties, the estimation is not feasible in field conditions.

Gamma spectroscopy is an established method for nuclide identification. It is based on the measurement of highly energetic photons which are emitted by atomic nucleus upon transition from a high energy state to a lower state. Similarly as in optical spectroscopy, the energy of the emitted photon equals the energy difference between the states. For this reason, the photon is the fingerprint of the radionuclide and provides a means for isotope identification. These highly energetic rays are able to penetrate materials much better than optical photons and their stopping is governed by the atomic number of the media.

A scintillation crystal is typically used for gamma ray spectroscopy. The possible interactions of gamma rays and material are absorption, Compton scattering and pair production¹. Photoelectric absorption is the most favorable for nuclide identification because all energy is transferred to an electron inside the crystal. The electron excites molecules of the crystal to luminous states which decay spontaneously. This creates a photon pulse whose intensity is proportional to the energy absorbed by the electron. In contrast, Compton scattering is an inelastic process where a photon transfers only a part of its energy to the crystal. This is problematic for identification as part of the photon energy may escape the crystal. Photoelectric absorption is typical for low energy photons while the probability of Compton scattering increases with photon energy. Pair production occurs at very high energies, when a photon interacts with electric field of an atomic nucleus and produces an electron-positron pair.

The directionality of gamma measurement is rather poor due to the fact that only heavy materials, such as lead, are effective for collimation. Therefore, gamma spectroscopy provides information on the amount and type of radionuclides present at the site, but gives only crude estimations on the location of the material. If collimation is not available, detector can be moved towards increasing count rates to locate sources, but this approach is not especially convenient. Another challenge is related to detection of trace quantities of active material which may be buried in the background spectrum of natural radioactivity. These issues can be addressed by using alpha-gamma coincidence detection for nuclides that decay by emitting gamma rays in conjunction with alpha particles.

Gamma rays are emitted as a side product of alpha decay if the daughter nucleus stays in an excited state after particle emission. This is characteristic to actinides and the prime example is ²⁴¹Am. Roughly every third alpha particle of ²⁴¹Am is accompanied by a 59.5 keV gamma ray, resulting from the excited state of ²³⁷Np that has a half-life of 68 ns¹⁰⁵. Hence, the emissions are emitted almost simultaneous. By focusing on these coincident events, it is possible to reduce the background of gamma detection significantly. This benefit comes at the cost of reduced detection efficiency but it is acceptable under certain conditions. Previously, alpha-gamma coincidence measurements have been applied to laboratory analysis using conventional alpha detectors¹⁰⁶. Publications IV and V describe the application of this technique by utilizing radioluminescence for alpha particle detection.

Figure 3.10a shows the basic components required for optical alpha-gamma measurement. Radioluminescence photons are collected with a lens objective to a PMT which produces digital pulses upon photon detection. The collection efficiency of the objective has a major effect on the coincidence count rate, since the product of alpha (ϵ_α) and gamma (ϵ_γ) detection efficiencies defines the total efficiency of coincidence detection

$$P_c = \epsilon_\alpha \epsilon_\gamma. \quad (3.2)$$

A geometric scaling gives adequate estimates on the detection efficiency of gamma rays while the optical alpha particle detection is highly dependent on objective and filter characteristics.

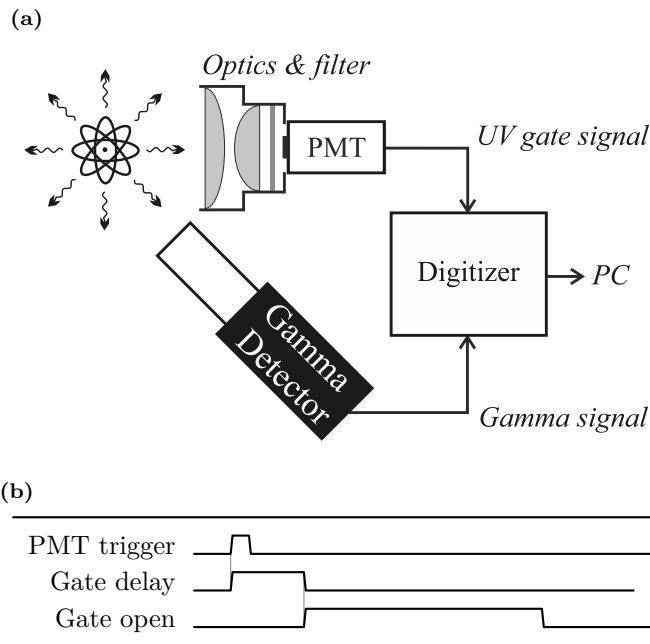


Figure 3.10: (a) Alpha-gamma coincidence measurement with PMT and gamma detector. Latest instruments can handle the trigger generation digitally while older instruments often need additional hardware for creating analogue gate signals. (b) Timing diagram of alpha-gamma coincidence gating. A PMT pulse triggers the delay timer after which the acquisition gate opens for a fixed time period. Although the emission of an alpha particle and gamma ray is often almost simultaneous, the propagation of gamma pulse is usually notably delayed in the signal acquisition electronics to justify the use of gate delay.

Several different detector types can be used for gamma spectrometry in this application. An ideal choice would exhibit high energy resolution together with a fast time response. In both Publications IV and V, high-purity germanium (HPGe) detector was used for gamma detection. It has a very high energy resolution which is especially important in X-ray region where there are several adjacent photopeaks. However, the charge collection process from a HPGe crystal takes time, and therefore, the length of the coincidence window has to be kept rather long (few μs). This increases the number of random coincidences which contribute to the background signal. The expected count rate of

random coincidences can be estimated with the equation

$$N_{random} = N_{\alpha}N_{\gamma}\tau, \quad (3.3)$$

where τ is the length of coincidence window. N_{α} and N_{γ} are the singles count rates of alpha and gamma detectors, respectively. Typical alternatives for the HPGe are sodium iodide (thallium activated) (NaI(Tl)) and lanthanum(III) bromide (LaBr₃) crystals which have their own benefits and trade-offs¹⁰⁷.

The gamma spectrum can be recorded with a multichannel analyzer (MCA) that has a gate input for use in coincidence applications. The gate signal is generated from the PMT pulse by introducing a short delay after which the gate is enabled for a desired time period. The gate signal timing diagram is depicted in Figure 3.10b. It is beneficial if both the alpha-gated and singles spectrum can be recorded simultaneously. In Publication IV, this was achieved by using two MCAs, but an attractive option is to use list mode data acquisition. In list mode, a time stamp and some parameters of the signal pulse are saved to a data file. This allows detailed post-processing, and also, the adjustment of coincidence window afterwards.

An example of optical alpha-gamma analysis is shown in Figure 3.11, where the technique was used in conjunction with the telescope of Section 3.3 to analyze a triple alpha source under high gamma environment. The telescope was focused on the alpha source that contains ²³⁹Pu, ²⁴¹Am and ²⁴⁴Cm with respective activities of 1720 Bq, 1871 Bq and 466 Bq. The gamma background was elevated with a ¹³³Ba source (approximately 30 kBq).

The gamma detection was performed with a LaBr₃ crystal (BrilLanCe 380, Saint Gobain), which has a fast primary decay time of 16 ns¹⁰⁸ that allows the utilization of short coincidence windows. Generally this material also has a high light yield and good energy resolution, but they are not realized at low energies which are in the main role with ²⁴¹Am. The crossover of energy resolution takes place in favor of NaI(Tl) at around 100 keV¹⁰⁹. The alpha and gamma signals were fed into input channels of a fast digitizer (DT5751, Caen) for list mode data acquisition. The results were later processed with a coincidence window of 500 ns. The singles spectrum is shown in Figure 3.11a and the alpha-gated spectrum in Figure 3.11b.

The peaks in the singles spectrum belong to the ¹³³Ba source and internal contamination of LaBr₃¹¹⁰. It would be difficult to notice the presence of ²⁴¹Am in the singles spectrum without any prior knowledge. However, when the alpha-gate is applied to the gamma spectrum, the 59.5 keV emission of ²⁴¹Am starts to dominate and only few random coincidences are observed. The downside is that the coincidence detection efficiency is very low, in the order of 0.01 cps. Without any gating applied, the average count rate of LaBr₃ was 561 cps while the PMT saw 13 cps in total. In retrospect, a higher alpha detection efficiency would have been achieved by using only the filter and PMT part in close proximity to the source. The telescope was designed for use at longer detection distances and provides little in benefit in this geometry.

The results shown here and in the Publications IV and V verify that radioluminescence light can be used to focus gamma measurements of alpha-gamma active materials. Furthermore, the method can be used to detect low activities which would otherwise be overwhelmed by more active gamma sources. The successful application of this technique is highly dependent on the collection efficiency of the optical system. Both alpha and gamma detector efficiencies scale with $1/R^2$ dependance, and therefore, the total coincidence

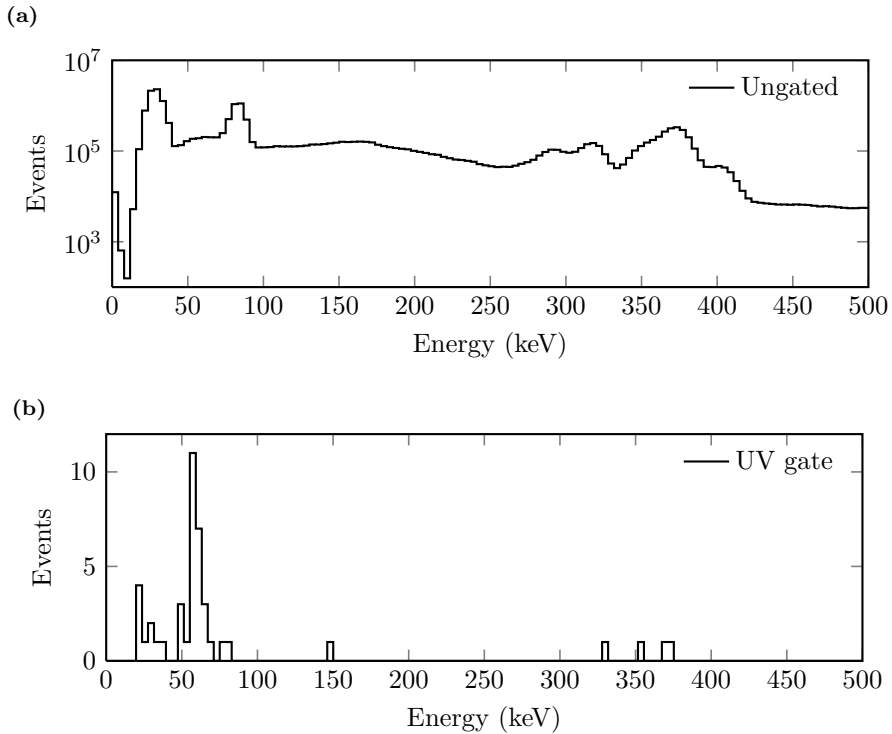


Figure 3.11: Results of alpha-gamma coincidence measurement with radioluminescence mapping telescope and LaBr_3 crystal (both at 20 cm SDD). (a) Singles gamma spectrum without UV gate. The 59.5 keV emission of ^{241}Am is buried in the background of ^{133}Ba and internal contamination of LaBr_3 . The trigger rate of LaBr_3 was 561 cps. (b) Alpha-gated gamma spectrum in which ^{241}Am is clearly visible. The coincidence count rate was 0.01 cps due to low efficiency of the UV detector.

count rate scales with $1/R^4$. This effectively limits the maximal detection range because diminishing true coincidence count rate rapidly reaches the level of random coincidence count rate. Hence, the best potential lies in close geometry applications where the optical approach has other benefits. An example of this could be non-destructive analysis of samples which are sealed in plastic bags to ascertain their integrity. These types of needs can be identified in nuclear safeguards and forensics applications.

4 Radon detection

Radon gas is the most significant source of ionizing radiation in the environment. It causes half of the population's annual radiation dose in Finland and more than 40 % globally¹¹¹. The only known health concern of radon is lung cancer and the number of related cases is estimated to be 200 per year in Finland¹¹². In United States, the number of radon related lung cancer deaths is around 10 000 - 20 000 annually¹¹³. It is difficult to distinguish between adverse effects of smoking and radon, because most people who develop lung cancer are exposed to both and as a result there is a certain degree of uncertainty in the estimations. Nevertheless, it is obvious that radon is hazardous to human health and causes a financial burden to society. Recently, there has been debate whether the dose coefficient of radon should be doubled^{114,115}. This change would emphasize the significance of radon mitigation even further.

4.1 Radon monitoring

Radon is generated in soil in the decay chain of uranium series, presented in Figure 4.1. Natural uranium (^{238}U) originates from time before formation of Earth and it has nothing to do with nuclear activities of the humankind. Radon (^{222}Ra) is born after alpha decay of radium (^{226}Ra), and unlike other materials in this decay series, it is a gaseous substance. It has a half-life of 3.8 days which is sufficiently long for the atoms to emanate from the ground into buildings. Interestingly, this "radioactivity which diffuses from radium as if gaseous in its nature" was already observed by Sir and Lady Huggins during their studies on radioluminescence of alpha particles in early 1900s⁸.

In addition to being gaseous, radon has a noble electron configuration which makes it chemically inert and prevents it from accumulating in the human body. However, one radon atom produces three alpha particles since its progenies (^{218}Po and ^{214}Po) are also alpha active. These are solid materials which effectively adhere to surfaces and also to respiratory tract. Therefore, the adverse health effects are mostly related to these nuclides rather than radon itself. The decay chain also includes two beta decays which inflict some cell damage, but at a smaller scale than alpha particles. The half-life of ^{210}Pb is long, and therefore, it can be considered as a stable nuclide within the time span of a typical radon measurement.

There are many isotopes of radon and they all are radioactive, but only two of them have significance for public health. In addition to uranium series, radon is also born in the decay chain of natural thorium. This isotope ^{220}Ra has a short half-life of 4 s and therefore it usually decays before reaching housings. However, it may have some role in areas which have a lot of thorium in the soil. The identification of the isotopes presents a challenge for radon detectors but there are solutions for this¹¹⁷.

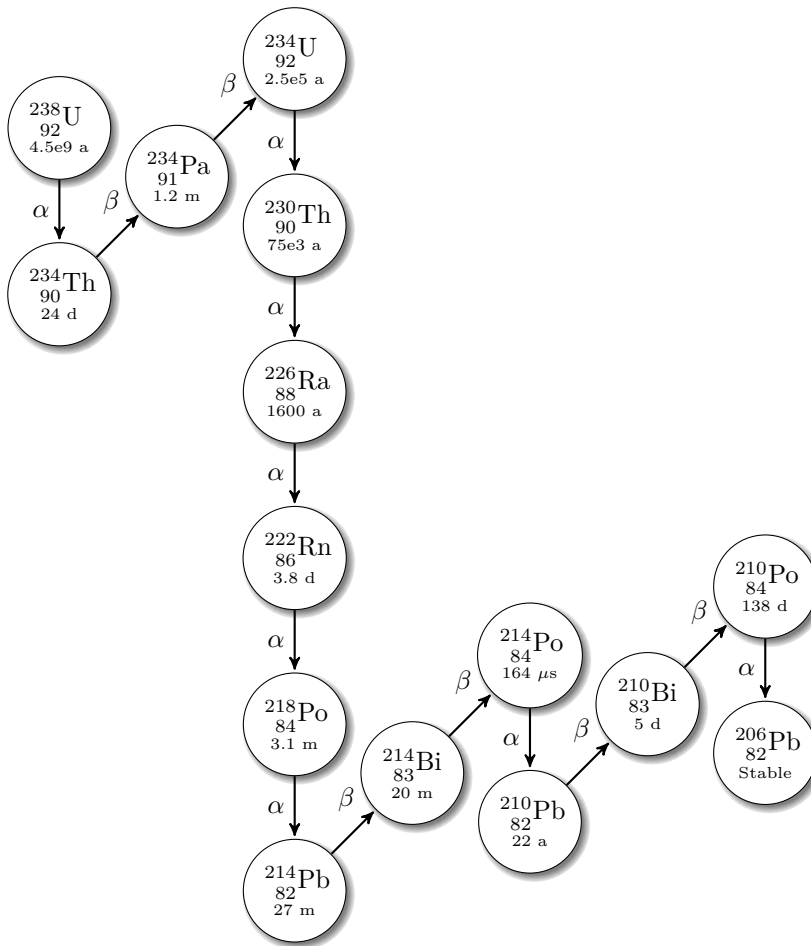


Figure 4.1: Dominant decay scheme of uranium series with half-lives¹¹⁶. Radon is created by spontaneous decay of natural radium. The half-life of 3.8 d is sufficient for radon to emanate from the ground into housings.

The classic radon detector is based on ZnS, similarly to many early and current alpha contamination probes. In 1950s, Henry Lucas invented a scintillation cell that carries his name and became widely adopted for fast radon measurement¹¹⁸. The inner walls of these cells are coated with ZnS so that radon and its progenies within the cell emit alpha particles onto the scintillator. The light pulses are observed with a PMT which usually enables good signal to background ratio. The background level of best Lucas cells is limited by alpha-active impurities contained in detector materials. However, the energy resolution of this design is limited by the varying light yield of ZnS and challenges in achieving uniform light collection geometry.

Another large volume approach for the detection of radon gas is based on ionization chamber. When an ionization chamber is used in the proportional counting regime, it has some energy resolution which is necessary for nuclide identification. However, the challenge is that radon decay may take place anywhere within the chamber volume and this complicates the signal analysis.

In Publication VI, the radioluminescence photons created in alpha decay are harnessed for the optical detection of radon. This approach enables direct detection of radon decay with good efficiency. Also, the detector is very scalable because physical size limitations are not especially stringent. The large volume is also the key in achieving high signal count rate. On the other hand, the energy resolution of the optical approach is limited by the number of generated photons (approximately 100 for ^{222}Ra) and pronounced by losses in the photon collection and detection process.

4.2 Optical detection principle

The photons created in radon decay are emitted in random directions. In free space, their detection would be difficult unless an exceptionally high radon concentration is present. The detection efficiency for single decay events can be increased by using a highly reflective measurement volume. In essence, the volume is an optical resonator where multiple reflections take place before photons are absorbed in the reflective walls or they escape through ports. For radon detection, two PMTs in coincidence counting mode are needed. This enables separation of alpha particle events from dark counts of the PMTs.

The optical radon detection system is shown in Figure 4.2. An integrating sphere was selected to be used as detection volume because they exhibit high diffuse reflectance which is also well-characterized by the manufacturer. The diameter of the sphere (SPH-8-3 AdaptaSphere, Labsphere) is 20 cm and average reflectance for nitrogen emission was calculated to be 97 %. In addition to high sphere reflectance, it is necessary to use large area PMTs to collect as many photons as possible from a single decay event. Here, two inch PMTs (9829QB, ET Enterprises) with high QE characteristics were selected for the purpose. The data acquisition was handled by using online coincidence detection feature of a fast digitizer (DT5751, Caen) with 32 ns window.

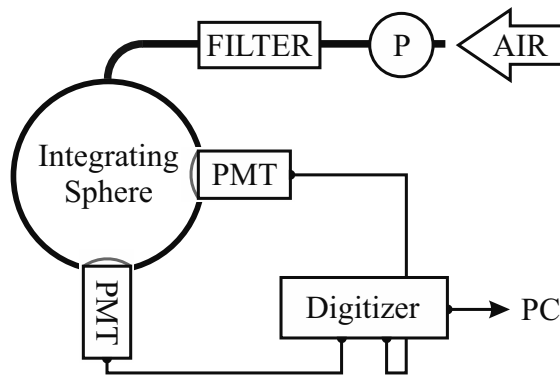


Figure 4.2: Optical radon detection setup. The pump (P) moves air into the detection volume through a HEPA filter which removes radon progenies from the air. The Figure was originally presented in Publication VI.

Air was continuously pumped into the measurement volume through a filter that removes radon progenies and other impurities from inlet air. This is important since the amount of radon progenies in room air can vary significantly. The varying fraction of daughter atoms would make calibration challenging because they represent 2/3 of the total number

of alpha decay events at a certain radon concentration. When the filter is employed, only radon can enter the detection volume and it can be assumed that each radon decay is followed by two additional alpha particles of the uranium series.

The digitizer stores events in list mode with 1 ns time resolution and integrates the pulse charge in two time windows of different length. This enables separation of fast and slow pulse components which are needed for the calculation of pulse shape discrimination (PSD) parameter. It is typically used in neutron-gamma discrimination¹¹⁹ but the principle is applicable to radon, provided that fast electronics are available. The PSD figure is calculated from the integrated charges with equation

$$PSD = \frac{Q_{long} - Q_{short}}{Q_{long}}. \quad (4.1)$$

The integration windows start 1 ns after trigger level is crossed. The length of the short window was 7 ns while the long window was 50 ns throughout this work. The values were experimentally selected to create the best possible separation of alpha particles from other events.

The evolution of a radon flash within the integrating sphere is a multifaceted process. First, the alpha particle is absorbed in air during its 5 ns flight time. The excitation of nitrogen molecules is instantaneous and the luminous states emit all photons within few ns lifetime. The emitted photons stay in the sphere until they are absorbed either in the sphere wall or in the PMT photocathodes. The highly reflective walls of the sphere act as a pulse stretcher which enables the evaluation pulse shape using the PSD parameter described above. The theory of integrating spheres is widely studied and hence the approximate duration of the flash can be estimated by calculating the product of the average number of reflections¹²⁰ M and average path length within the sphere¹²¹ L

$$t = \frac{1}{c} \cdot M \cdot L = \frac{1}{c} \cdot \frac{\rho}{1 - \rho(1 - f)} \cdot \frac{2}{3}d. \quad (4.2)$$

In this equation, c is the speed of light, ρ is the average sphere reflectance for nitrogen emission, f is the fraction of port area to sphere surface area (0.031), and d is the diameter of the sphere. It does not consider absorption which is negligible in air at short distances at these wavelengths^{47,122}. According to this calculation, the estimated average lifetime of a photon in the sphere is 7 ns.

The experimental work showed that the PSD analysis improves selectivity for radon decay events while the more intuitive approach with pulse energy spectroscopy did not produce the desired result in the initial tests. Simple coincidence counting without any further signal processing provides excellent detection efficiency, but this comes at the cost of high background signal. A major part of this background corresponds to pulses which resemble single photoelectron pulses and the origin of this signal is not fully understood at the moment. Nevertheless, the PSD analysis reduces background level by a factor of three. The method is described in Figure 4.3 which shows that the PSD values of coincident pulses accumulate to four main regions in a two dimensional histogram.

The designated regions of the histogram have different response to changes in radon concentration. This is presented in Table 4.1 where the correlation of UV coincidence count rate and radon concentration is shown together with corresponding background signal levels. Type A events have a PSD of around 0.2 which is typical for single photoelectron pulses. The coincidences in this region respond to changes in radon concentration but

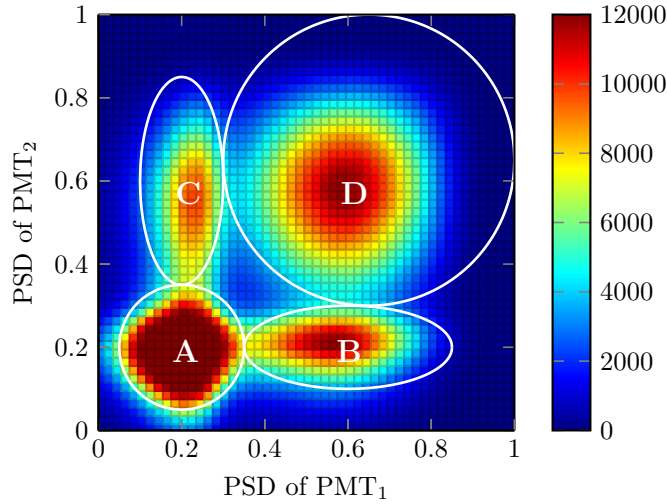


Figure 4.3: Distribution of coincident pulse shapes in the optical radon detector. The histogram is based on events recorded during a two week measurement period. The peak value in region A is 45 000.

Table 4.1: Signal and background count rates in specified areas of Figure 4.3.

Area	Radon response (cps/Bq/l)	Background (cps)
A	0.8	1.6
BC	1.8	1.2
D	4.6	0.6

with low SBR. In regions B and C one PMT is triggered by only one photoelectron while the other detects a longer pulse, and hence, the SBR is better for radon effects. In region D, the highest response to radon is achieved together with the lowest background. As a compromise between count rate and background level, regions B, C and D were selected for the final radon signal calibration.

4.3 System response

The optical radon detection system was tested and benchmarked against AlphaGuard detector (Saphymo GmbH) which is among the leading instruments for rapid radon detection. It is based on proportional counter design which suggests ability to perform alpha spectroscopy to a certain degree. For the measurements, the detectors were deployed at Optics Laboratory of TUT which is located at ground level. The ventilation of this property is operational during extended office hours only. During nights and weekends, radon levels rise significantly due to radon diffusion from the ground. An example of this daily variation is clearly observed in Figure 4.4a.

As seen in the results, the agreement between AlphaGuard and optical detector is excellent. However, the agreement is achieved by calibrating the optical signal against the data provided by AlphaGuard. The calibration was performed by using data points of late afternoon and early morning hours, because in these the radon concentration is at its most stable. The calibration curves are shown in Figure 4.4b.

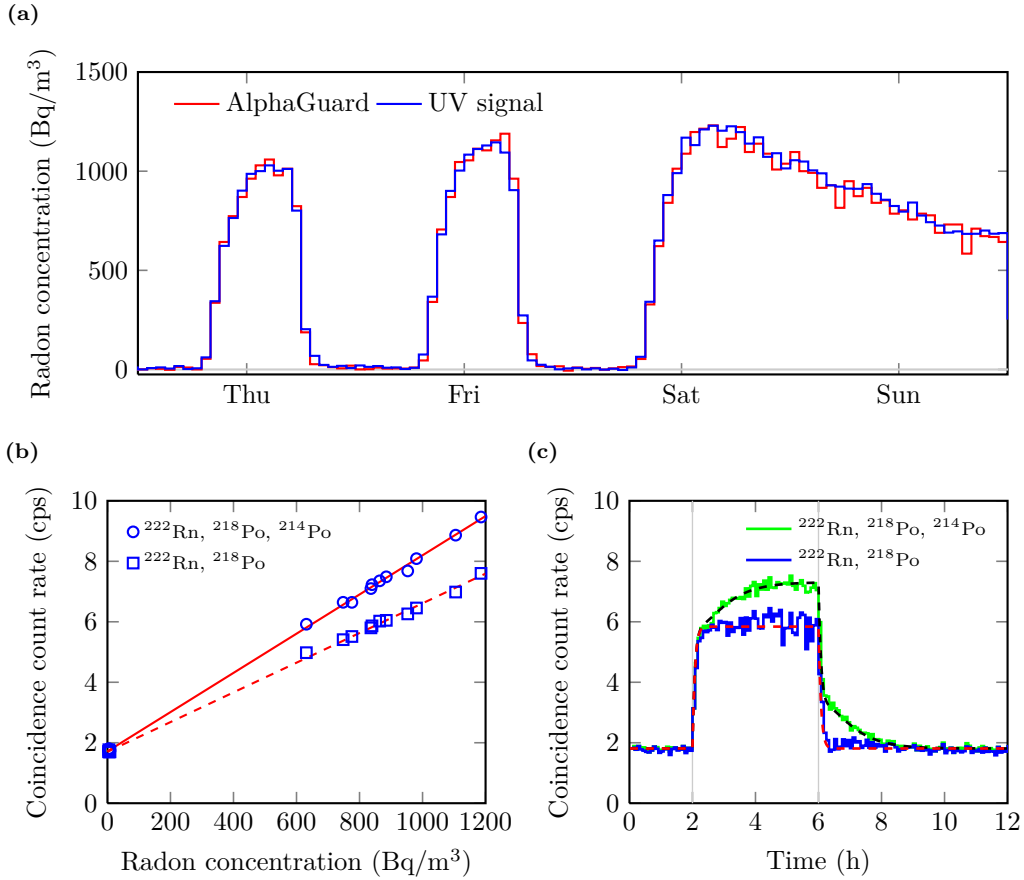


Figure 4.4: (a) Radon concentration in an office property measured with AlphaGuard and UV signals of ^{222}Rn and ^{218}Po . The variation arises from ventilation which operates during office hours only. (b) Calibration of UV signals with AlphaGuard. The calibration is presented with and without the contribution of ^{214}Po . (c) Step response test using clean scientific air and radon-containing room air (870 Bq/m^3). The start and stop of the radon feed are indicated with the vertical lines. The result verifies that the slowly settling ^{214}Po has to be addressed in rapid measurement applications.

The calibration curves are shown for two distinct cases: The first is shown for the total signal with all detected alpha decay events of ^{222}Rn , ^{218}Po and ^{214}Po . The second includes the contribution of ^{222}Rn and ^{218}Po only. Although the latter option detects lower number of events, it has a fast response to changes in radon concentration. This is related to ^{214}Po that grows slowly into the measurement volume. By analyzing the decay chain in Figure 4.1 it can be shown that it takes more than two hours before ^{214}Po reaches secular equilibrium with ^{222}Rn and ^{218}Po . Therefore, fast radon measurements require that the signal of ^{214}Po is separated from the other two.

In this case, the identification of ^{214}Po decay was achieved by observing the nearly coincident emission of ^{214}Bi beta and ^{214}Po alpha particles. The particles are emitted within a short time interval because the half-life of ^{214}Po is only $164 \mu\text{s}$. Another solution could be based on the pulse energy spectroscopy, but this approach was not thoroughly

investigated. However, it was used as an additional parameter to filter out the desired events with enhanced confidence. The background-free detection efficiency for these events was 2.5 %, assuming that decay products do not leave the measurement volume. The blue curve in Figure 4.4a was obtained by subtracting the estimated amount of ^{214}Po from the total alpha signal.

The estimation of ^{214}Po contribution to the total signal requires knowledge of its detection efficiency. In order to study this, it is necessary to assume that Po attaches to sphere surfaces and produces light only upon emitting alpha particles towards air. In this case, the theoretical upper limit for detection efficiency is 50 %. The same assumption was made for ^{218}Po although it is likely that bigger portion of this nuclide is airborne at the time of decay, because the half-life is only 3.1 min.

The slow stabilization of ^{214}Po is demonstrated in a step response test shown in Figure 4.4c. Here, the evolution of UV signal is shown with and without the contribution of ^{214}Po . The figure also contains the modeled responses for both cases. The models were fitted to the experimental data by using detection efficiencies as fitting parameters. It was observed that a good agreement between the model and experiment was achieved when the detection efficiency for radon was set to 0.7. It was assumed that both polonium isotopes were detected with equal efficiency which found good agreement to the data at 0.4. Using this value, the subtraction of ^{214}Po signals was possible. It would be interesting to develop the method towards better independence of this polonium signal in the future.

In conclusion, the optical radon detector provides exceptional signal count rate in a volume that is not limited by the range of alpha particles. Therefore, the statistical quality is very high but this comes at the cost of high background. Due to the high background, the full potential of the large measurement volume could not be exploited in the detection of low radon concentrations. The minimum detectable concentration (MDC) of the device was calculated with Currie's method ($\alpha = \beta = 0.05$) with the assumption of well-known background¹⁰¹

$$MDC = \frac{L_D}{N_S t} = \frac{2.71 + 3.29\sqrt{N_B t}}{N_S t}. \quad (4.3)$$

Here, N_S is the slope of the calibration curve and N_B is background count rate. The detection limit is 12 Bq/m³ for 1 h measurement when ^{214}Po is in equilibrium within the detector. If the signal of ^{214}Po is subtracted, the MDC is 15 Bq/m³ with ^{222}Rn and ^{218}Po alone.

In order to fully verify the capabilities of the optical approach, extensive testing would be required under varying environmental conditions. These experiments have not been performed to date, but studies on air fluorescence yield show that the method would benefit from decreasing temperature and humidity²⁹. Additionally, it would be important to reduce the component cost of the device before further steps towards commercialization in radon applications. One way to achieve this would be to utilize only one low background PMT for the measurement. This would rule out the detection of low concentrations but could potentially work already at 100 Bq/m³ radon concentration.

The performance of the optical radon detector is listed with leading radon detection technologies in Table 4.2. The performance of commercial instruments is reported as in manufacturer specifications^{117,123}. The Table verifies that commercial instruments have a lower signal count rate but they still provide better detection capability due to their low background. The optical detector would have the lowest relative uncertainty in a rather

Table 4.2: Comparison of online radon measurement technologies.

Detector	Sensitivity (cps/Bq/l)	Background (cps)	Volume (dm ³)	Efficiency (%)	Range (Bq/m ³)
This work	6.5	1.8	4.2	0.52	12...
Alpha Guard	0.8	<0.0002	0.56	0.48	2...2e6
Radon Scout	0.4	<0.0002	0.25	0.53	2...2e6

unusual application where a high activity is measured with a short integration time. This strengthens the conclusion that further developments should be directed towards reducing the background of the optical system. Also, it should be noted that the background of any radon detector increases in use due to accumulation of ²¹⁰Po within the detection volume. In the case of AlphaGuard unit used in this work, this accumulation contributed to a background signal equal to 11 Bq/m³ radon concentration. This is usually addressed with regular device calibrations.

The efficiency column in Table 4.2 refers to detection of all alpha particles (²²²Rn, ²¹⁸Po, ²¹⁴Po) within the measurement volume per time unit in secular equilibrium. Interestingly, all detectors seem to have approximately equal detection efficiency. This is a positive result for the optical approach because it justifies the use of large detection volume.

The limit for the maximal measurement concentration was not studied in this work, but it is expected that very high concentrations could be measured. Air is a very fast scintillator and the integrating sphere does not stretch the flashes beyond 100 ns. Therefore, pile-up effects are not easily observed from the physical point of view. For example, in 2 MBq/m³ radon concentration the presented detector would have an alpha particle event every 40 μ s on average. This is a reasonable event rate for a PMT in photon counting, although it would present a challenge for the list mode data acquisition used in this work. High concentrations could also be tackled by single channel or current mode measurements in extreme cases.

An application for the presented device may also be found in surface contamination detection of small objects. The 20 cm diameter sphere would fit small tools that need to be screened for alpha or beta emitters. The benefit of the approach is in the integral measurement of contamination. This allows single measurement for an object without maneuvering the detector or object to achieve full coverage. In other words, the integral measurement principle reduces the maximum missable activity which is important for practical applications. The 1 h detection limit of the device (12 Bq/m³) equals to an alpha activity of 0.05 Bq in the detection volume, which as an integral value, is more than sufficient for alpha contamination screening of most objects¹²⁴. However, physical objects reduce the optical efficiency of the sphere due to absorption of photons. For this reason, maintaining a high detection efficiency for small items may require increase in the number and size of PMTs.

4.4 Considerations on background

The source of the background signal (1.8 cps) was not identified in Publication VI. However, the potential causes are discussed here on the basis of literature. The presence of so-called naturally occurring radioactive materials (NORMs) can always be expected when a measurement of radioactivity is performed. The most critical locations are the inner coating of the detection sphere and the windows of the PMTs. Assuming that

the observed background signal is induced by an alpha active NORM, the total activity within the sphere would be 4.5 Bq (40 % detection efficiency). This equals to average activity of 0.004 Bq/cm² on the inner surface of the sphere. This activity level would be difficult to detect experimentally, and hence, the contribution of natural radioactivity can not be ruled out.

A constant nitrogen purge into the detection volume increases the background level (in BCD regions) by 50 %. This is a clear indication that at least a part of the background is due to ionizing radiation within the detection volume. The only and yet subtle change in the PSD plot can be observed in area where both pulses have a PSD of about 0.8. Judging from the behavior of radon decay events which are loosely concentrated around PSD of 0.6, the observed change in nitrogen is due to particles which have a high total light yield in the sphere. This suggests that there are heavy ionizing particles in the sphere also when it is flushed with radon-free gases.

One form of natural ionizing radiation are muons which are created by interactions of cosmic particles in upper atmosphere. The muon flux at ground level is less than 1 muons/cm²/min which means that a few muons pass through the 20 cm diameter sphere every second. The linear energy loss of a muon is about 2.2 keV/cm in air at ground level¹²⁵. By making a crude estimate that their light yield is similar to alpha particles (19 photons/MeV), the number of created photons in the sphere is less than one per muon. For this reason, the interactions of muons with air molecules are not a likely reason for any multiphoton background events in optical radon measurement. On the other hand, muons may interact with the sphere surface or with the PMT windows. It is known that relativistic particles cause Cherenkov radiation in glass and the rate of muon events is approximately 15 per minute at ground level for a two inch PMT¹²⁶. These Cherenkov emissions contribute to the coincidence background in this experiment since the light propagates easily from one PMT to another via the reflecting sphere. A similar effect may also arise from NORMs such as beta-emitting ⁴⁰K which is known to be present in PMT glass¹²⁶.

The expected background count rate of two PMTs in coincidence mode is actually higher than proposed by Equation 3.3. This is due to extraneous light emission of PMTs as noted by several authors^{127–129}. There are numerous independent causes for these effects and they are especially relevant to systems where discrimination level is set for photon counting^{127,128}. Furthermore, the light emissions tend to overlap with nitrogen bands¹²⁷ and hence filters can not be used to overcome the challenge.

The contribution of extraneous emissions can be investigated by analyzing the list mode data acquired during the experiments. If a PMT emits light in coincidence setup, the emitting PMT has an excellent geometry to detect its own emission and the emitting PMT is likely to detect the pulse first. While the magnitude of these emissions may vary, it is expected that some of the mechanisms produce large pulses to the emitting PMT and only a small portion of the light travels to the receiving unit. The charge ratio of coincident pulses is plotted in Figure 4.5, by dividing the charge of smaller pulse with the charge of larger pulse. An anomaly is observed for charge ratios smaller than 0.1 and this could be related to an extraneous emission effect. The temporal behavior supports this assumption since the big pulse is predominantly observed before the smaller one. Moreover, the incidence rate of these events does not change under nitrogen purge as shown in the Figure 4.5. This supports to the assumption that the initiating light pulse is produced within the PMTs.

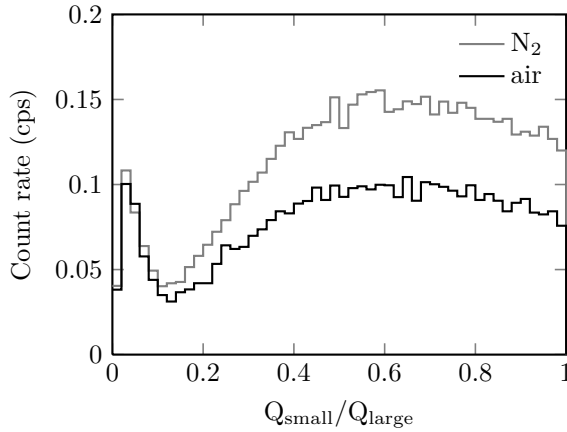


Figure 4.5: Charge ratios of background coincidences in clean scientific air and nitrogen. An anomaly is observed for pulse pairs which have a charge ratio smaller than 0.1. The incidence rate of these events does not change under nitrogen purge and they do not respond to changes in radon concentration at all. These events may be related to spurious light emission of PMTs.

A further investigation of pulses with charge ratio smaller than 0.1 reveals that they are not affected by changes in radon concentration. Hence, they can be filtered from the data without loss in signal, although this was not implemented in this work. The total contribution of these pulses is close to 10 % of the observed background in regions BCD (see Figure 4.3). In conclusion, this analysis suggests that at least the aforementioned part of the background signal is related to light emission processes within the PMTs. On the other hand, the increase in nitrogen atmosphere verifies that a substantial part of background events are caused by ionizing radiation within the detector. It would be essential to investigate if this radiation can be mitigated in future designs. Significant reduction in the background level would unveil the full potential of the optical method in rapid measurement of very low radon concentrations.

5 Conclusions and discussion

The results presented in this Thesis confirm that air can be successfully used as a scintillator to detect alpha radiation in practical applications. Whilst the remote detection sensitivities are far from the typical free release limits of alpha contamination, the systems are progressing towards levels which could be relevant for characterization applications in nuclear industry. The main results of this work can be categorized under three topics: photon yield study, surface contamination detection and analysis, and radon detection.

The quantitative performance estimation requires exact knowledge of the radioluminescence efficiency of alpha particles and this was investigated in Publication I. The study concluded that the light production of alpha particles is 19 ± 3 photons/MeV, which is close to the conversion efficiency of electrons at comparable energies. The result is expected since secondary particles are the most important exciters of luminous states in gas phase. The study also showed a linear dependency between photon yield and alpha particle energy loss, which is widely observed for electrons too.

A key argument for radioluminescence imaging is the capability to measure through translucent materials. This was demonstrated in Publication II where a camera system was deployed at a nuclear research facility. The camera was used to image alpha active materials that were in gloveboxes and in shielded cells. The purpose of this work was to gain understanding on practicalities of fieldwork and to test the performance of different camera technologies in darkness. Both the EMCCD and ICCD camera were able to detect MBq level alpha sources within the glovebox with an exposure time of a few min. Thick lead glasses elevate the detection limit in shielded cells, but the experiments verify that some hot spots can still be identified. In addition to ambient optical background and its spectrum, the limit of detection with a camera is always affected by light transmission of windows and characteristics of the lens. Furthermore, the trade-off between FOV and light throughput has implications for the selection of the lens. The benefit of camera-based alpha detection is in the high resolution and information content of the images.

The experiences with camera imaging facilitated the development of light-tolerant detection capabilities presented in Publication III. In this work, an automated radioluminescence mapping device was developed. The system is based on single pixel scanning which enables the use of filters that have a high tolerance for background light, as long as the light does not overlap with the detection band. The system can be used under UV-free lighting to detect alpha sources with a 4 kBq activity (1 m distance, 10 s integration). Under normal lighting, the device can detect 800 kBq sources with similar parameters. The system can be quickly deployed for an automated alpha screening mission, but it is best suited for free space detection. The reason is that most translucent materials have limited transmission in UV region, and therefore, a new filter would need to be developed for use in the vicinity of 400 nm wavelengths.

Coincidence techniques for alpha contamination analysis are presented in Publications IV and V, where radioluminescence photons of alpha particles are used to trigger a gamma measurement. This suits to the analysis of the actinides which decay by simultaneous emission of an alpha particle and gamma ray. The utilization of alpha gate enhances signal to noise ratio by reducing background of gamma spectrum drastically. Additional benefit comes from the ability to focus the gamma measurement to a certain point by optics.

In Publication VI photon-photon coincidences are used for direct detection of radon decay in air. The conversion of signal carriers into optical photons enables large detection volumes to be used with high detection efficiency. This provides fast response and high signal count rate for the measurement, but the inherent background of the system limits detection of very low radon concentrations. The current system is capable of detecting 12 Bq/m³ concentrations in 1 h measurement time.

Prospective applications

The imaging and mapping systems presented in this work are best suited for remote characterization applications in nuclear industry. The technique can be regarded complementary to gamma cameras in the detection of actinides. In contrast to gamma cameras, radioluminescence imaging is strictly surface specific, providing a means to assess the amount of open contamination. Alpha imaging systems may be applied to *in situ* sensing of contaminated facilities, buildings and waste packages. Outdoor applications can also be identified for sufficiently light-tolerant systems.

The user benefits from remote characterization by receiving an improved picture of the radiological state of the facility. This information can be used to make informed decisions in planning and executing decommissioning work. Furthermore, the approach allows for automated or vehicle-borne information gathering. This limits the time spent in hazardous areas and enables remote screening of spaces which are difficult to access otherwise. The increased detection distance also helps to prevent instrument contamination.

The optical alpha screening of gloveboxes and shielded cells is shown to be technologically possible. However, this requires light shielding because most UV emissions are blocked by the materials used in their construction. The light-shielding of an operational glovebox is rather tedious due to the transparent structure and numerous feed-throughs, whereas in the case of shielded cells, the light shield can be more easily applied.

The decontamination of a shielded cell is a process that can span several months, because the work is performed with telemanipulators, and methods to characterize contamination within the cell are very limited. A typical challenge can be a cell from which all material is removed, but the dose rate still remains high. In this situation, alpha imaging may help to identify the problem areas since only optical photons are transmitted through the lead glass. Imaging can also be used at the beginning of the process to identify hot spots so that contamination is not spread to clean areas during the course of work.

As noted before, solar blind techniques can be insensitive to visible light but they can not operate through most windows or plexiglass. Therefore, their use is limited to free-space applications at old installations. However, it would be easy to make new facilities compatible with this technology if remote alpha detection is regarded as potential need in the future. The use of nitrogen and argon as protective gas further emphasizes the potential because these gases increase the radioluminescence yield of alpha particles. In

solar blind region, the signal enhancement can be as high as two orders of magnitude which enables detection of few kBq point sources regardless of lighting used (see Table 3.1).

Additional need for free-space alpha particle detection can be identified in the field of nuclear safety and security. To date, nuclear materials have been released in at least two accidents where aircrafts carrying nuclear weapons have crashed to the ground. The most famous cases are the Palomares incident of 1966 and the Thule incident of 1968^{130,131}. In both accidents, some of the warheads on-board the planes were damaged and nuclear material was dispersed into the environment. The resulting contamination is very tedious to locate since nuclear warheads are primarily based on ²³⁹Pu which is a strong alpha emitter but has rather low gamma yields. Therefore, it is obvious that an optical alpha detection system would be a useful tool to guide cleanup in such cases. The same applies to scenarios where alpha active material has been dispersed with malicious motives.

The concept of optical radon measurement is attractive due to the unique characteristics of radioluminescence light. This application also differs from the aforementioned examples in a sense that light shielding does not pose practical challenges. The achieved signal count rates were high and the response was fast. However, the potential of the large measurement volume was not fully unveiled due to the background signal which limited the measurement of low concentrations. Moreover, the detector is not viable for commercialization before current components can be replaced with low cost alternatives. At present, the small item screening application could be the most interesting way forward.

Future outlook

The detection concepts described in this work represent demonstrations with a technology readiness level equal to 5, according to NASA definition¹³². The commercialization of the demonstrators would require efforts especially in the fields of systems integration and software development. The aim of the current work was to develop proof-of-concept designs using COTS components which naturally leaves room for future improvements.

The key enabling technologies of radioluminescence detection are filters and detectors. As an example, narrow-band and high performance absorptive filters would be needed for a scanning camera system that tolerates background light in the visible region. The utilization of an imaging detector would make alpha contamination mapping faster and the results more appealing to the end user. However, this is not possible with filters that are readily available from component vendors. Military applications are important facilitators for development in this branch of photonics and potentially these outcomes can be translated to optical alpha particle detection in the future. Furthermore, it is clear that spectral identification would help to avoid false positives in the detection.

The prospect of significant operational savings or improvements in safety are usually required before an investment is made to translate new technology into operative use. The challenge of optical alpha particle detection is to achieve detection limits that would be especially appealing to the industry. Although there is definite interest towards this technology, the relatively high detection limits easily turn the table towards technology push rather than market pull. The gap can be bridged by two-fold approach. First, the performance of the current systems can be further optimized and any progress in filters and detectors should be utilized. Second, the dialogue between nuclear operators and instrument developers should be strengthened to identify cases where this technology would be best applied.

Bibliography

- [1] G. Knoll, *Radiation Detection and Measurement*. John Wiley & Sons, New York (US), 2010.
- [2] *Radiation Protection and Safety of Radiation Sources: International Basic Safety Standards*. International Atomic Energy Agency, Austria, 2014.
- [3] *Nuclear Security Fundamentals, Objective and Essential Elements of a State's Nuclear Security Regime*. International Atomic Energy Agency, Austria, 2013.
- [4] *IAEA Safeguards Glossary*. International Atomic Energy Agency, Austria, 2002.
- [5] S. M. Baschenko, "Remote optical detection of alpha particle sources," *Journal of Radiological Protection*, vol. 24, pp. 75–82, 2004.
- [6] F. Lamadie, F. Delmas, C. Mahe, P. Girones, C. Le Goaller, and J. R. Costes, "Remote alpha imaging in nuclear installations: new results and prospects," *IEEE Transactions on Nuclear Science*, vol. 52, no. 6, pp. 3035–3039, 2005.
- [7] G. Imbard, "Remote α source location device and method," 2001. US Patent 6,281,502.
- [8] W. Huggins and L. Huggins, "On the spectrum of the spontaneous luminous radiation of radium at ordinary temperatures," *Proceedings of the Royal Society of London*, vol. 72, no. 477-486, pp. 196–199, 1903.
- [9] M. Duquesne and I. Kaplan, "Mesure de la luminescence induite par le rayonnement α du ^{210}Po dans l'air et dans l'eau," *Journal de Physique et le Radium*, vol. 21, no. 10, pp. 708–716, 1960.
- [10] D. L. Chichester and S. M. Watson, "Multispectral UV-visual imaging as a tool for locating and assessing ionizing radiation in air," *IEEE Transactions on Nuclear Science*, vol. 58, no. 5, pp. 2512–2518, 2011.
- [11] Working Party on Decommissioning and Dismantling, *R&D and Innovation Needs for Decommissioning Nuclear Facilities*. OECD Nuclear Energy Agency (NEA), 2014.
- [12] *Nuclear Reactor Decommissioning Industry: Global Market Size and Competitive Landscape Analysis to 2030*. Global Data, 2012.
- [13] A. Neslen, "Europe faces €253bn nuclear waste bill," *The Guardian*, 4 April 2016.
- [14] M. A. Levi and H. C. Kelly, "Weapons of mass disruption," *Scientific American*, vol. 287, no. 5, pp. 76–81, 2002.

- [15] R. B. McFee and J. B. Leikin, “Death by polonium-210: lessons learned from the murder of former Soviet spy Alexander Litvinenko,” *Seminars in Diagnostic Pathology*, vol. 26, no. 1, pp. 61–67, 2009.
- [16] S. R. Owen, ed., *Report into the death of Alexander Litvinenko*. House of Commons, 2016.
- [17] P. Bachelor, D. Jordan, W. Harper, B. Cannon, and E. Finn, “Self-absorption effects on alpha-induced atmospheric nitrogen fluorescence yield,” *Journal of Radioanalytical and Nuclear Chemistry*, vol. 282, pp. 873–876, 2009.
- [18] J. Yao, J. Brenizer, R. Hui, and S. S. Yin, “Standoff alpha radiation detection via excited state absorption of air,” *Applied Physics Letters*, vol. 102, no. 25, p. 254101, 2013.
- [19] C. Thompson, E. Barritt, and C. Shenton-Taylor, “Predicting the air fluorescence yield of radioactive sources,” *Radiation Measurements*, vol. 88, pp. 48 – 54, 2016.
- [20] V. Hannuksela, *Remote detection of alpha radiation by fluorescence of nitrogen (in Finnish)*. Master’s thesis, Tampere University of Technology, 2009.
- [21] S. Ihantola, *Novel approaches to the analysis of nuclear and other radioactive materials – Improving detection capability through alpha-gamma coincidence, alpha-induced optical fluorescence and advanced spectrum analysis*. PhD thesis, Aalto University, 2013.
- [22] W. Huggins and L. Huggins, “On the spectrum of the spontaneous luminous radiation of radium. Part III. Radiation in hydrogen,” *Proceedings of the Royal Society of London. Series A*, vol. 76, no. 512, pp. 488–492, 1905.
- [23] W. Huggins and L. Huggins, “On the spectrum of the spontaneous luminous radiation of radium. Part IV. Extension of the glow,” *Proceedings of the Royal Society of London Series A*, vol. 77, no. 515, pp. 130–131, 1906.
- [24] H. Geiger and E. Marsden, “On a diffuse reflection of the α -particles,” *Proceedings of the Royal Society of London. Series A, Containing Papers of a Mathematical and Physical Character*, vol. 82, no. 557, pp. 495–500, 1909.
- [25] E. Rutherford, “The scattering of α and β particles by matter and the structure of the atom,” *The London, Edinburgh, and Dublin Philosophical Magazine and Journal of Science*, vol. 21, no. 125, pp. 669–688, 1911.
- [26] M. J. Berger, J. S. Coursey, M. A. Zucker, and J. Chang, *Stopping-power and range tables for electrons, protons, and helium ions*. NIST Physics Laboratory, 1998.
- [27] E. B. Podgorsak, ed., *Radiation oncology physics – a handbook for teachers and students*. International Atomic Energy Agency, Austria, 2005.
- [28] J. W. Chamberlain, *Physics of the Aurora and Airglow*. Academic Press, New York (US), 1961.
- [29] T. Waldenmaier, “Spectral resolved measurement of the nitrogen fluorescence yield in air induced by electrons,” *Wissenschaftliche Berichte FZKA*, vol. 7209, 2006.
- [30] J. M. Hollas, *Modern spectroscopy*. John Wiley & Sons, Chippingham (UK), 2004.

- [31] S. Bayram and M. Freamat, “Vibrational spectra of N_2 : An advanced undergraduate laboratory in atomic and molecular spectroscopy,” *American Journal of Physics*, vol. 80, no. 8, pp. 664–669, 2012.
- [32] A. Lofthus and P. H. Krupenie, “The spectrum of molecular nitrogen,” *Journal of Physical and Chemical Reference Data*, vol. 6, no. 1, pp. 113–307, 1977.
- [33] J. H. Moore, “Investigation of the Wigner spin rule in collisions of N^+ with He, Ne, Ar, N_2 , and O_2 ,” *Physical Review A*, vol. 8, no. 5, pp. 2359–2362, 1973.
- [34] A. N. Bunner, *Cosmic Ray Detection by Atmospheric Fluorescence*. PhD thesis, Cornell University, 1967.
- [35] T. Waldenmaier, J. Blümer, and H. Klages, “Spectral resolved measurement of the nitrogen fluorescence emissions in air induced by electrons,” *Astroparticle Physics*, vol. 29, no. 3, pp. 205–222, 2008.
- [36] M. M. Fraga, A. Onofre, L. Pereira, N. Castro, F. Veloso, F. Fraga, R. F. Marques, M. Pimenta, and A. Policarpo, “Temperature-dependent quenching of UV fluorescence of N_2 ,” *Nuclear Instruments and Methods in Physics Research Section A*, vol. 597, no. 1, pp. 75 – 82, 2008. Proceedings of the 5th Fluorescence Workshop.
- [37] M. Zubek, “Excitation of the $C^3\Pi_u$ state of N_2 by electron impact in the near-threshold region,” *Journal of Physics B: Atomic, Molecular and Optical Physics*, vol. 27, no. 3, p. 573, 1994.
- [38] J. T. Fons, R. S. Schappe, and C. C. Lin, “Electron-impact excitation of the second positive band system ($C^3\Pi_u \rightarrow B^3\Pi_g$) and the $C^3\Pi_u$ electronic state of the nitrogen molecule,” *Physical Review A*, vol. 53, no. 4, pp. 2239–2247, 1996.
- [39] G. Poparic, M. Vicic, and D. Belic, “Vibrational excitation of the $C^3\Pi_u$ state of N_2 by electron impact,” *Chemical Physics*, vol. 240, no. 1-2, pp. 283 – 289, 1999.
- [40] F. Blanco and F. Arqueros, “The role of secondary electrons in some experiments determining fluorescence emission from nitrogen $C^3\Pi_u$ levels,” *Physics Letters A*, vol. 345, no. 4-6, pp. 355 – 361, 2005.
- [41] Y. Itikawa, “Cross sections for electron collisions with nitrogen molecules,” *Journal of Physical and Chemical Reference Data*, vol. 35, no. 1, pp. 31–53, 2006.
- [42] W. L. Borst and E. C. Zipf, “Cross section for electron-impact excitation of the (0,0) first negative band of N_2^+ from threshold to 3 keV,” *Physical Review A*, vol. 1, no. 3, pp. 834–840, 1970.
- [43] I. Tatischeff, “Specific excitation of N_2 and specific ionization by 4.3 MeV α particles,” *The Journal of Chemical Physics*, vol. 52, no. 2, pp. 503–508, 1970.
- [44] F. Arqueros, F. Blanco, and J. Rosado, “Analysis of the fluorescence emission from atmospheric nitrogen by electron excitation, and its application to fluorescence telescopes,” *New Journal of Physics*, vol. 11, no. 6, p. 065011, 2009.
- [45] F. R. Gilmore, R. R. Laher, and P. J. Espy, “Franck–Condon factors, r-centroids, electronic transition moments, and Einstein coefficients for many nitrogen and oxygen band systems,” *Journal of Physical and Chemical Reference Data*, vol. 21, no. 5, pp. 1005–1107, 1992.

- [46] J. Danielak, U. Domin, R. Ke, M. Rytel, and M. Zachwieja, "Reinvestigation of the emission γ band system ($A^2\Sigma^+ - X^2\Pi$) of the NO molecule," *Journal of Molecular Spectroscopy*, vol. 181, no. 2, pp. 394–402, 1997.
- [47] L. Elterman, "UV, visible, and IR attenuation for altitudes to 50 km," Defense Technical Information Center document, Air Force Cambridge Research Laboratories, Hanscom (US), 1968.
- [48] "ASTM G173-03, standard tables for reference solar spectral irradiances: Direct normal and hemispherical on 37° tilted surface," standard, ASTM International, West Conshohocken, PA, 2012.
- [49] O. P. Ivanov, V. E. Stepanov, S. Smirnov, and A. Volkovich, "Development of method for detection of alpha contamination with using UV-camera "DayCor" by OFIL," in *Nuclear Science Symposium and Medical Imaging Conference, 2011 IEEE*, pp. 2192–2194, 2011.
- [50] M. D. Roberts, "Detection of ionizing radiation using solar blind air fluorescence," report, Defence Science and Technology Organisation, 2013.
- [51] J. Sand and K. Peräjärvi, "Interim report from the solar blind region spectral response studies," deliverable 1.1.1 of MetroDecom project, European Metrology Research Programme, 2016.
- [52] F. Kakimoto, E. C. Loh, M. Nagano, H. Okuno, M. Teshima, and S. Ueno, "A measurement of the air fluorescence yield," *Nuclear Instruments and Methods in Physics Research Section A*, vol. 372, no. 3, pp. 527–533, 1996.
- [53] M. Nagano, K. Kobayakawa, N. Sakaki, and K. Ando, "Photon yields from nitrogen gas and dry air excited by electrons," *Astroparticle Physics*, vol. 20, no. 3, pp. 293 – 309, 2003.
- [54] P. Colin, A. Chukanov, V. Grebenyuk, D. Naumov, P. Nedelec, Y. Nefedov, A. Onofre, S. Porokhovoi, B. Sabirov, and L. Tkatchev, "Measurement of air and nitrogen fluorescence light yields induced by electron beam for UHECR experiments," *Astroparticle Physics*, vol. 27, no. 5, pp. 317 – 325, 2007.
- [55] G. Lefeuvre, P. Gorodetzky, J. Dolbeau, T. Patzak, and P. Salin, "Absolute measurement of the nitrogen fluorescence yield in air between 300 and 430 nm," *Nuclear Instruments and Methods in Physics Research Section A*, vol. 578, no. 1, pp. 78–87, 2007.
- [56] R. Abbasi, T. Abu-Zayyad, K. Belov, J. Belz, Z. Cao, M. Dalton, Y. Fedorova, P. Huntmeyer, B. Jones, C. Jui, *et al.*, "Air fluorescence measurements in the spectral range 300-420 nm using a 28.5 GeV electron beam," *Astroparticle Physics*, vol. 29, no. 1, pp. 77 – 86, 2008.
- [57] J. Rosado, F. Blanco, and F. Arqueros, "Comparison of available measurements of the absolute air-fluorescence yield," *Astroparticle Physics*, vol. 34, no. 3, pp. 164 – 172, 2010.
- [58] A. E. Grün and E. Schopper, "Über die Fluoreszenz von Gasen bei Anregung durch α -Teilchen," *Zeitschrift Naturforschung Teil A*, vol. 6, no. 11, pp. 698–700, 1951.

- [59] G. Ortner and S. Salim, "Light emission from polonium," *Nature*, vol. 169, pp. 1060–1061, 1952.
- [60] J. B. Birks and J. W. King, "The luminescence of air, glass and quartz under α -particle irradiation," *Proceedings of the Physical Society. Section B*, vol. 66, no. 2, p. 81, 1953.
- [61] A. Grün, "Die Fluoreszenz von Gasen bei der Abbremsung schneller Teilchen. Spektroskopische Untersuchungen," *Zeitschrift Naturforschung Teil A*, vol. 9, no. 1, pp. 55–63, 1954.
- [62] A. Ward, "The emission of light in the passage of alpha particles through gases," *Proceedings of the Physical Society. Section A*, vol. 67, no. 9, p. 841, 1954.
- [63] R. W. Nicholls and E. M. Reeves, "Luminescence produced in air by polonium-210 alpha-particles," *Nature*, vol. 180, pp. 1188–1189, 1957.
- [64] R. C. Axtmann and J. T. Sears, "Excitation of nitrogen gas by alpha particles and fission fragments," *The Journal of Chemical Physics*, vol. 44, no. 9, pp. 3279–3283, 1966.
- [65] S. Dondes, P. Harteck, and C. Kunz, "A spectroscopic study of alpha-ray-induced luminescence in gases: Part I," *Radiation Research*, vol. 27, no. 2, pp. 174–210, 1966.
- [66] J. Birks, *The Theory and Practice of Scintillation Counting*. International Series of Monographs in Electronics and Instrumentation, Pergamon Press, Frome (UK), 1964.
- [67] G. Davidson and R. O'Neil, "Optical radiation from nitrogen and air at high pressure excited by energetic electrons," *The Journal of Chemical Physics*, vol. 41, no. 12, pp. 3946–3955, 1964.
- [68] J. Sand, V. Hannuksela, S. Ihantola, K. Peräjärvi, H. Toivonen, and J. Toivonen, "Remote optical detection of alpha radiation," in *Symposium on International Safeguards*, no. IAEA-CN-184/23, 2010.
- [69] D. L. Chichester and S. M. Watson, "Multispectral UV-visual imaging as a tool for locating and assessing ionizing radiation in air," in *Nuclear Science Symposium Conference Record, 2010 IEEE*, pp. 447–453, IEEE, 2010.
- [70] L. Koch and R. Lesueur, "Quelques resultats concernant la fluorescence de gaz excites par des particules chargees de grande energie (some results on the fluorescence of gases excited by high-energy charged particles)," report, Commissariat a l'Energie Atomique, Paris, 1958.
- [71] A. G. Wright, "Absolute calibration of photomultiplier based detectors—difficulties and uncertainties," *Nuclear Instruments and Methods in Physics Research Section A*, vol. 433, no. 1, pp. 507–512, 1999.
- [72] Ludlum Measurements Inc., *Alpha Detector - Model 43-1*, 2016.
- [73] P. Gooda and W. Gilboy, "High resolution alpha spectroscopy with low cost photo-diodes," *Nuclear Instruments and Methods in Physics Research Section A*, vol. 255, no. 1, pp. 222 – 224, 1987.

- [74] R. D. Horansky, J. N. Ullom, J. A. Beall, G. C. Hilton, K. D. Irwin, D. E. Dry, E. P. Hastings, S. P. Lamont, C. R. Rudy, and M. W. Rabin, "Superconducting calorimetric alpha particle sensors for nuclear nonproliferation applications," *Applied Physics Letters*, vol. 93, no. 12, 2008.
- [75] H. O. Anger, "Scintillation camera," *Review of Scientific Instruments*, vol. 29, no. 1, pp. 27–33, 1958.
- [76] H. O. Anger and D. J. Rosenthal, "Scintillation camera and positron camera," *Medical radioisotope scanning*, vol. 19, pp. 59–75, 1959.
- [77] J. Katz, G. Seaborg, and L. Morss, *Chemistry of the actinide elements*. Methuen, New York (US), 2 ed., 1987.
- [78] C. Mahé, F. Lamadie, and C. Le Goaller, "Recent advances in low-level nuclear measurements at the CEA - 9212," in *Waste Management Conference, Phoenix, Arizona USA*, 2009.
- [79] C. Mahé, "Alpha imaging: recent achievements and glove box characterization," in *Decommissioning, Decontamination, and Reutilization Topical Meeting, Idaho Falls, Idaho, USA*, 2010.
- [80] C. Mahé and C. Chabal, "Recent improvement of measurement instrumentation to supervise nuclear operations and to contribute input data to 3D simulation code," in *Waste Management Conference, Phoenix, Arizona USA*, 2013.
- [81] T. Cousins and D. S. Haslip, "Stand and deliver," *CBRNe World*, pp. 56–59, Winter 2006.
- [82] E. Inrig, V. Koslowsky, B. Andrews, M. Dick, P. Forget, H. Ing, R. Hugron, and L. Wong, "Development and testing of an air fluorescence imaging system for the detection of radiological contamination," in *Conference Proceedings – American Institute of Physics*, vol. 1412, pp. 393–400, 2011.
- [83] E. Inrig, L. Erhardt, V. Koslowsky, B. Andrews, H. Ing, M. Dick, E. Forget, Patrick and P. Forget, "An air fluorescence imaging system for the detection of radiological contamination," *SPIE Defense, Security, and Sensing Conference, Orlando*, vol. 8018, pp. 80180G–80180G–6, 2011.
- [84] E. Inrig, I. Watson, V. Koslowsky, M. Dick, and P. Forget, "Design and preliminary testing of the multi-spectral imaging system for the detection of radiological contamination," Technical Memorandum DRDC Ottawa TM 2011-195, Defence R&D Canada, 2011.
- [85] US Congress, "Atomic energy act of 1954," 1954.
- [86] W. A. Seidler, M. Zukic, E. L. Fry, C. H. Hill, and W. Blackwell, "Remote detection of fissile material," 2002. US Patent 6,448,562.
- [87] Defense Advanced Research Projects Agency, "Request for information: Indirect detection of special nuclear materials at standoff (SNMS)," 2009. DARPA-SN-09-50.
- [88] R. K. Harrison, J. B. Martin, D. Wiemann, J. Choi, and S. Howell, "New radiological material detection technologies for nuclear forensics: Remote optical imaging and graphene-based sensors," report SAND2015-7567, Sandia National Laboratories, 2015.

- [89] D. Chichester, S. Pozzi, E. Seabury, J. Dolan, M. Flaska, J. Johnson, S. Watson, and J. Wharton, “FY09 Advanced instrumentation and active interrogation research for safeguards,” report INL/EXT-09-16611, Idaho National Laboratory (INL), 2009.
- [90] J. S. Feener, *Fluorescence Imaging for Nuclear Arms Control Verification*. PhD thesis, Texas A & M University, 2014.
- [91] J. Feener and W. Charlton, “Warhead verification using nuclear fluorescence,” in *Institute of Nuclear Materials and Management Taos Technical Meeting*, May 2011.
- [92] J. S. Feener and W. S. Charlton, “Initial results of nuclear fluorescence imaging for arms control verification,” in *Institute of Nuclear Materials Management 54th Annual Meeting*, July 2013.
- [93] J. S. Feener and W. S. Charlton, “Preliminary results of nuclear fluorescence imaging of alpha and beta emitting sources,” in *Advancements in Nuclear Instrumentation Measurement Methods and their Applications, 2013 3rd International Conference on*, pp. 1–8, IEEE, 2013.
- [94] J. Campbell, *Manual on Safety Aspects of the Design and Equipment of Hot Laboratories*. International Atomic Energy Agency, Austria, 1969.
- [95] V. I. Arbutov, N. Z. Andreeva, N. A. Leko, S. I. Nikitina, N. F. Orlov, and Y. K. Fedorov, “Optical, spectral, and radiation-shielding properties of high-lead phosphate glasses,” *Glass Physics and Chemistry*, vol. 31, pp. 583–590, 2005.
- [96] S. Yamamoto, M. Komori, S. Koyama, and T. Toshito, “Luminescence imaging of water during alpha particle irradiation,” *Nuclear Instruments and Methods in Physics Research Section A*, vol. 819, pp. 6 – 13, 2016.
- [97] M. Ave, M. Bohacova, B. Buonomo, N. Busca, L. Cazon, S. Chemerisov, M. Conde, R. Crowell, P. D. Carlo, C. D. Giulio, *et al.*, “Measurement of the pressure dependence of air fluorescence emission induced by electrons,” *Astroparticle Physics*, vol. 28, no. 1, pp. 41 – 57, 2007.
- [98] A. E. Leybourne, S. Creasey, J. Dixon, J. Lee, G. Messer, S. Neal, G. H. Rayborn, D. Speaks, J. Stephens, T. Strange, C. D. Walker, W. C. West, H. F. Woodruff, and C. B. Winstead, “Long range detection of radiation-induced air fluorescence,” in *Proceedings of the Institute of Nuclear Materials Management*, 2010.
- [99] National Physical Laboratory, “NPL builds long range Alpha Detector.” Online, 2010. Available at www.npl.co.uk/news/npl-builds-long-range-alpha-detector.
- [100] W. C. West, *Background UV in the 300 to 400 nm region affecting the extended range detection of radioactive material*. PhD thesis, University of Alabama, 2010.
- [101] L. A. Currie, “Limits for qualitative detection and quantitative determination. application to radiochemistry,” *Analytical chemistry*, vol. 40, no. 3, pp. 586–593, 1968.
- [102] C. Ganguly, *Characterisation and Quality Control of Nuclear Fuels*. Allied Publishers, New Delhi (India), 2004.

- [103] J. Lacquement, H. Boussier, A. Laplace, O. Conocar, and A. Grandjean, “Potentialities of fluoride-based salts for specific nuclear reprocessing: Overview of the R&D program at CEA,” *Journal of Fluorine Chemistry*, vol. 130, no. 1, pp. 18 – 21, 2009.
- [104] Labsphere Inc., “Optical-grade Spectralon reflectance material,” datasheet, 2015.
- [105] M. Basunia, “Nuclear data sheets for $A = 237$,” *Nuclear Data Sheets*, vol. 107, no. 8, pp. 2323 – 2422, 2006.
- [106] J. Turunen, *Novel methods for analysis of radioactive samples using position-sensitive detectors, coincidence techniques and event-mode data acquisition*. PhD thesis, Univeristy of Jyväskylä, 2013.
- [107] E. V. D. van Loef, P. Dorenbos, C. W. E. van Eijk, K. Krämer, and H. U. Güdel, “High-energy-resolution scintillator: Ce^{3+} activated $LaBr_3$,” *Applied Physics Letters*, vol. 79, no. 10, pp. 1573–1575, 2001.
- [108] Saint-Gobain Crystals, *BrilLanCe 380 Scintillation Material*, 2004.
- [109] P. Dorenbos, J. T. M. de Haas, and C. W. E. van Eijk, “Gamma ray spectroscopy with a $\varnothing 19 \times 19 \text{ mm}^3$ $LaBr_3: 0.5\% Ce^{3+}$ scintillator,” *IEEE Transactions on Nuclear Science*, vol. 51, no. 3, pp. 1289–1296, 2004.
- [110] B. D. Milbrath, R. C. Runkle, T. W. Hossbach, W. R. Kaye, E. A. Lepel, B. S. McDonald, and L. E. Smith, “Characterization of alpha contamination in lanthanum trichloride scintillators using coincidence measurements,” *Nuclear Instruments and Methods in Physics Research Section A*, vol. 547, no. 2, pp. 504–510, 2005.
- [111] United Nations Scientific Committee on the Effects of Atomic Radiation, *Sources and effects of ionizing radiation UNSCEAR 2008 Report to General Assembly with Scientific Annexes*, vol. 1. United Nations, 2008.
- [112] R. Pöllänen, ed., *Säteily ympäristössä*. Säteilyturvakeskus – Radiation and Nuclear Safety Authority, 2003.
- [113] N. Grossblatt, ed., *Health Effects of Exposure to Radon: BEIR VI*. Committee on Health Risks of Exposure to Radon, Board on Radiation Effects Research, Commission on Life Sciences, National Research Council, 1999.
- [114] M. Tirmarche, J. Harrison, D. Laurier, F. Paquet, E. Blanchardon, and J. Marsh, “ICRP publication 115 – Lung cancer risk from radon and progeny and statement on radon,” *Annals of the ICRP*, vol. 40, no. 1, pp. 1 – 64, 2010.
- [115] L. Vaillant and C. Bataille, “Management of radon: a review of ICRP recommendations,” *Journal of Radiological Protection*, vol. 32, no. 3, p. R1, 2012.
- [116] National Nuclear Data Center, Brookhaven National Laboratory, “Chart of nuclides,” online database, 2016. Available at <http://www.nndc.bnl.gov/chart/>.
- [117] Saphymo GmbH, *AlphaGUARD Short description*, 2015.
- [118] H. F. Lucas, “Improved low level alpha scintillation counter for radon,” *Review of Scientific Instruments*, vol. 28, no. 9, pp. 680–683, 1957.

- [119] D. Cester, M. Lunardon, G. Nebbia, L. Stevanato, G. Viesti, S. Petrucci, and C. Tintori, "Pulse shape discrimination with fast digitizers," *Nuclear Instruments and Methods in Physics Research Section A*, vol. 748, no. 0, pp. 33 – 38, 2014.
- [120] K. Carr, "Integrating sphere theory and applications Part I: Integrating sphere theory and design," *Surface Coatings International Part B: Coatings Transactions*, vol. 80, no. 8, pp. 380–385, 1997.
- [121] J. Kirk, "Modeling the performance of an integrating-cavity absorption meter: theory and calculations for a spherical cavity," *Applied Optics*, vol. 34, no. 21, pp. 4397–4408, 1995.
- [122] W. A. Baum and L. Dunkelman, "Horizontal attenuation of ultraviolet light by the lower atmosphere," *Journal of the Optical Society of America*, vol. 45, no. 3, pp. 166–175, 1955.
- [123] SARAD GmbH, *Radon Scout PMT*, 2015.
- [124] *Regulations for the Safe Transport of Radioactive Material, Safety Standards Series No. TS-R-1*. International Atomic Energy Agency, Austria, 2005.
- [125] D. E. Groom, N. V. Mokhov, and S. I. Striganov, "Muon stopping power and range tables 10 MeV–100 TeV," *Atomic Data and Nuclear Data Tables*, vol. 78, no. 2, pp. 183–356, 2001.
- [126] ET Enterprises Ltd, "Understanding photomultipliers," 2011.
- [127] H. Krall, "Extraneous light emission from photomultipliers," *IEEE Transactions on Nuclear Science*, vol. 14, no. 1, pp. 455–459, 1967.
- [128] R. J. Riley and A. G. Wright, "The effect of photomultiplier afterpulses in coincidence systems," *Journal of Physics E: Scientific Instruments*, vol. 10, no. 9, p. 873, 1977.
- [129] A. G. Wright, "An investigation of photomultiplier background," *Journal of Physics E: Scientific Instruments*, vol. 16, no. 4, p. 300, 1983.
- [130] M. Jiménez-Ramos, R. García-Tenorio, I. Vioque, G. Manjón, and M. García-León, "Presence of plutonium contamination in soils from Palomares (Spain)," *Environmental Pollution*, vol. 142, no. 3, pp. 487–492, 2006.
- [131] O. Lind, B. Salbu, K. Janssens, K. Proost, M. Garcia-Leon, and R. Garcia-Tenorio, "Characterization of U/Pu particles originating from the nuclear weapon accidents at Palomares, Spain, 1966 and Thule, Greenland, 1968," *Science of the Total Environment*, vol. 376, no. 1, pp. 294–305, 2007.
- [132] J. C. Mankins, "Technology readiness levels," white paper, Advanced Concepts Office, Office of Space Access and Technology, NASA, 1995.

Publications

Publication I

J. Sand, S. Ihanola, K. Peräjärvi, H. Toivonen, and J. Toivonen

“Radioluminescence yield of alpha particles in air”

New Journal of Physics, vol. 16, p. 053022, 2014.

© 2014 IOP Publishing Ltd and Deutsche Physikalische Gesellschaft.

Creative Commons Attribution 3.0 License.

Radioluminescence yield of alpha particles in air

J Sand¹, S Ithantola², K Peräjärvi², H Toivonen² and J Toivonen¹

¹Tampere University of Technology, Optics Laboratory, PO Box 692, FI-33101 Tampere, Finland

²STUK—Radiation and Nuclear Safety Authority, PO Box 14, FI-00881 Helsinki, Finland
E-mail: johan.sand@tut.fi

Received 27 January 2014, revised 25 March 2014

Accepted for publication 9 April 2014

Published 9 May 2014

New Journal of Physics **16** (2014) 053022

doi:[10.1088/1367-2630/16/5/053022](https://doi.org/10.1088/1367-2630/16/5/053022)

Abstract

Alpha particles can be detected by measuring the radioluminescence light which they induce when absorbed in air. The light is emitted in the near ultraviolet region by nitrogen molecules excited by secondary electrons. The accurate knowledge of the radioluminescence yield is of utmost importance for novel radiation detection applications utilizing this secondary effect. Here, the radioluminescence yield of an alpha particle is investigated as a function of energy loss in air for the first time. Also, the total radioluminescence yield of the particle is measured with a carefully calibrated ²³⁹Pu emitter used in the experiments. The obtained results consistently indicate that alpha particles generate 19 ± 3 photons per one MeV of energy released in air at normal pressure (temperature 22 °C, relative humidity 43%) and the dependence is found to be linear in the studied energy range from 0.3 MeV to 5.1 MeV. The determined radioluminescence yield is higher than previously reported for alpha particles and similar to the radioluminescence yield of electrons at comparable energies. This strengthens the evidence that the luminescence induced by charged particles is mostly proportional to the energy loss in the media and not very sensitive to the type of primary particle.

Keywords: radioluminescence, air fluorescence, alpha particles, optical detection



Content from this work may be used under the terms of the [Creative Commons Attribution 3.0 licence](https://creativecommons.org/licenses/by/3.0/).

Any further distribution of this work must maintain attribution to the author(s) and the title of the work, journal citation and DOI.

1. Introduction

The alpha-induced luminescence of air can be utilized for remote detection of open alpha emitting radioactive sources [1–5]. The motivation for the optical approach arises from the fact that luminescence light can convey decay information far beyond the range of an alpha particle. This enables remote and safe detection of highly hazardous alpha emitters by photon counting devices and sensitive cameras. Since the optical method is not limited by the range of the particle, significant advancements can be achieved in decontamination and safety inspection applications. Furthermore, it is possible to monitor contamination through ultraviolet (UV) transmitting materials such as plexi and lead glass, without breaching the containment [5, 6]. The technique has been demonstrated in field tests by independent research units and it has the potential to evolve into an industry-standard procedure in the future [3–5, 7]. An important design parameter for all promising applications is the luminescence efficiency of air, which is widely studied for electrons, but publications regarding alpha particles are few in number.

Light emission induced by alpha particles in air was first observed by Sir William and Lady Huggins in the early years of the 20th century [8]. At the time, the emission spectrum was recorded with a film spectrometer and found to be coincident with the band spectrum of nitrogen. It was concluded that the radioluminescence mostly originates from 2P and 1N band systems of molecular and ionized nitrogen, which are known to emit light in the spectral region from 300 nm to 430 nm [9]. In the 1950s, the recently invented photomultiplier tube (PMT) catalyzed further studies on the scintillation properties of different materials and the effect was widely examined in noble gases but also in nitrogen and air [10–12]. One of the earliest reports to quantify the number of photons generated by a single alpha particle in air is described by Duquesne and Kaplan in 1960 [13]. The result of 60 photons per one 4.6 MeV particle was achieved with a PMT equipped with a quartz window. More recently in 2004, Baschenko used UV-sensitive film for the measurement which resulted in 30 photons per alpha particle from a highly active ^{239}Pu emitter [1]. In 2011, Chichester and Watson concluded that the yield is between 20 and 200 photons per one alpha particle in the 4–5 MeV energy range [2]. In this retrospect, quantitative studies on alpha particle luminescence yield are fairly rare, mainly due to the fact that practical implementations for detection purposes have only recently started to emerge.

The physics of electron-induced luminescence in air is widely studied by the astrophysics community [14–20]. The comprehensive set of knowledge acquired from electron experiments can be directly applied to alpha particle studies, since emission characteristics and de-excitation of nitrogen molecules are independent of the preceding interactions. However, the excitation efficiency should be studied independently for alpha and beta particles, since there are differences in the mass and charge of the initial particle. It is noteworthy that the luminescence is mostly induced by collisions with secondary electrons and nitrogen molecules in both cases [20].

In this work, the absolute radioluminescence yield of alpha particles is studied with two conceptually simple experiments which are designed for accuracy and repeatability. First, the optical emission from a calibrated point source is observed with a PMT as a function of source-to-detector distance (SDD). This result is then used to calculate the total luminescence yield along the alpha particle track. Second, a passivated implanted planar silicon (PIPS) detector is

Table 1. Activities of different isotopes in the emitter. The method of measurement is indicated in the first column. Note that the activity of ^{241}Pu is calculated from the atomic ratio of $^{241}\text{Pu}/^{239}\text{Pu}$ in the original solution.

Method	^{239}Pu (kBq)	^{240}Pu (kBq)	^{238}Pu (kBq)	^{241}Am (kBq)	^{241}Pu (kBq)
PIPS	$48.3 \pm 3.1\%$	$4.0 \pm 3.1\%$	$0.41 \pm 3.1\%$	$1.2 \pm 6.5\%$	$20.1 \pm 3.1\%$
HPGe	$49.1 \pm 4.1\%$	$3.1 \pm 20\%$	—	$1.32 \pm 3\%$	—

utilized to record a UV-gated alpha spectrum. This enables the measurement of luminescence yield as a function of deposited energy, reported here for the first time. In addition, a brief supplementary experiment was conducted to investigate the effect of humidity on the luminescence yield. The obtained results are summarized to give a precise and up-to-date estimate of alpha particle radioluminescence yield in air.

2. Experimental methods

2.1. Calibrated alpha emitter

The ^{239}Pu alpha emitter used in the experiments was prepared from a nitrate solution by electrodeposition on a steel planchet. The work was conducted by the radiochemistry laboratory of the Finnish Radiation and Nuclear Safety Authority and the solution was certified by the Institute for Reference Materials and Measurements. The solution contained mostly ^{239}Pu and had minute amounts of ^{238}Pu , ^{240}Pu , ^{241}Pu , ^{241}Am , and ^{242}Pu as impurities. The 15 mm diameter planchet was uniformly covered to a 1 mm distance from the edge with the active material, and it was left uncoated to achieve a sharp energy peak and uniform emission of alpha particles.

The alpha source was carefully studied by alpha and gamma spectroscopic measurements to verify the surface emission rate and the amount of active material. The alpha measurement was performed with a PIPS detector in a vacuum and the gamma analysis was conducted with an HPGe detector (Canberra, BE5030). A summary of the results is presented in table 1. The activity of ^{241}Pu is estimated from the atomic ratio of $^{241}\text{Pu}/^{239}\text{Pu}$ in the original solution since, as a weak beta emitter, it could not be measured directly. It is assumed that the atomic ratio of the original solution is not affected by the electrodeposition process.

As presented in table 1, the vast majority of alpha particles are emitted by ^{239}Pu . The total alpha activity of the emitter is 53.9 ± 1.7 kBq, which is calculated according to the PIPS measurements, since they are the best to represent the surface emission rate. In addition, the data imply that activity-weighted average alpha decay energy of the emitter is 5.1 MeV. The plutonium source also contains a significant quantity of beta-particle-emitting isotope ^{241}Pu . Fortunately, the total energy deposited to air by these low-energy beta particles (average energy 5.2 keV [21]) is over 2600 times smaller than the energy deposited by the alpha particles. Thus, their contribution to the total light emission can be neglected.

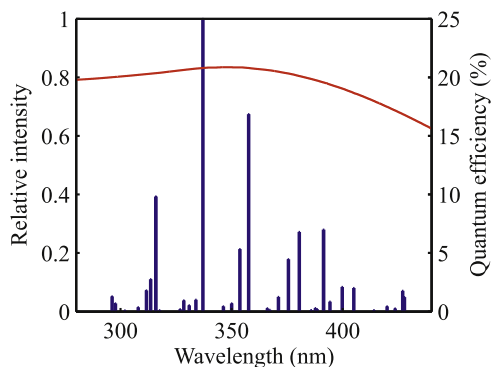


Figure 1. Relative intensities of nitrogen emission bands and smooth quantum efficiency curve of the photomultiplier tube. The intensities of nitrogen bands are measured by Ave *et al* [9].

2.2. Measurements with calibrated point alpha emitter

The total luminescence yield along the alpha particle track can be measured by placing a single-photon sensitive detector at a known distance from a radiation source. The alpha particles ionize air in a half-sphere that has a radius equivalent to their range in air. This scintillating hemisphere can be observed as an optical point source from a sufficient distance. The emission of photons is isotropic, and therefore, the photon flux spreads evenly over the full solid angle. Under these conditions, the luminescence yield can be measured from every direction that is not subtended by the source itself.

In this experiment, a channel photomultiplier (Perkin Elmer, MP-1982P) with a low-noise bi-alkali photocathode was used to count the luminescence photons. This module exhibits an extremely low dark count rate (below 0.5 s^{-1}) making it suitable for measuring low photon flux signals while still maintaining a large, 15 mm diameter active area. The detector is sensitive to photons at a wavelength range from 165 nm to 650 nm, and the quantum efficiency is calibrated by the vendor to be 18.3% at 410 nm. The average quantum efficiency for nitrogen emission was estimated to be 20.3%. The value was obtained by adjusting the catalogue spectral response curve with the efficiency reported by the vendor and weighting the value with the relative intensities of the main nitrogen emission bands. The emission intensities are quoted as in the work of Ave *et al* [9] and these are presented together with the quantum efficiency curve in figure 1. A traceable, end-to-end calibration of the photon counting module was not performed, but the spectral response data provided by Perkin Elmer are in good agreement with state-of-the-art calibration techniques [22].

For the measurements, the radiation source was placed on a steel pole so that the PMT observes the scintillating volume from the side (see figure 2 (a)). This geometry minimizes the contribution of the photons that are reflected from the emitter planchet to the detector. Furthermore, the emitter pole was attached to a remote-controlled slide so that the SDD could be varied from 200 mm to 600 mm. The whole assembly was enclosed in a cardboard box to protect it from external light. The inner surfaces of the box were covered with matte black aluminum foil to prevent the reflection of light. Also, a 30 mm iris was positioned in front of the photomultiplier to further reduce the contribution of scattered photons. The iris was positioned

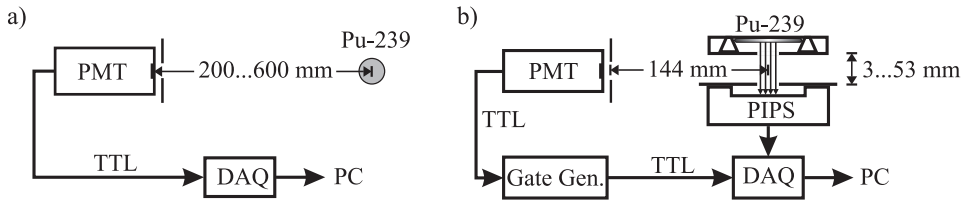


Figure 2. (a) Photon counting setup with variable source-to-detector distance. (b) Setup for UV-gated alpha energy measurement. The distance between emitter and PIPS detector was adjustable.

close enough to the detector (25 mm) for the photocathode to act as a limiting aperture (field stop) in this system. Lastly, a remote-controlled shutter plate was placed in front of the iris to enable the measurement of the detector dark count rate.

2.3. Measurements with alpha-UV coincidence

The radioluminescence yield as a function of alpha particle energy loss in air was measured using alpha-photon coincidences. The alpha emitter was attached vertically to a holder on a translation stage, and a PIPS alpha detector was placed on the opposite side of the emitter planchet (see figure 2(b)). Both the emitter and the detector were covered with a circular diaphragm made of black foil (Acktar, Vacuum Black) to mitigate reflections. The 5 mm diameter aperture of the diaphragms collimated the alpha beam to a cylindrical shape and therefore, the size of the optical source was significantly smaller than given by the total light-yield measurement.

The PMT was placed at a 150 mm distance from the center of the optical source. The distance was chosen so that the point-source approximation is valid while maintaining a sufficiently high photon count rate. A 10 mm diameter aperture was placed close to the PMT window to reduce the acceptance angle of the detector. The distance between the surfaces that cover the alpha emitter and the PIPS detector was adjustable from 3 mm to 53 mm (figure 2(b)). As in the first experiment, the whole measurement setup was enclosed in a light-tight box with black matte aluminum foil lining the inner surfaces.

The alpha detection system consisted of a PIPS detector (Canberra) and a multichannel analyzer. This instrumentation was used to record the alpha energy spectrum in both singles and gated mode. The gate signal was generated from the digital PMT output pulse by introducing a short delay and extending it to 1 μ s. The acquired spectra were analyzed to reveal the average count rate and mean energy of detected alpha particles. At each measured point, the calculation was limited to those particles that were included in a 200 keV wide energy window around the main alpha peak.

The energy loss along the track of an alpha particle is described by the Bragg curve, presented in figure 3. This curve was used to estimate the amount of energy that is absorbed in the field of view of the PMT. The photons generated just after the emitter and just before PIPS are not visible to the PMT due to mechanical collimation of the alpha beam. The amount of energy that is producing detectable luminescence emission was calculated by subtracting the losses and the measured residual energy from the assumed initial particle energy.

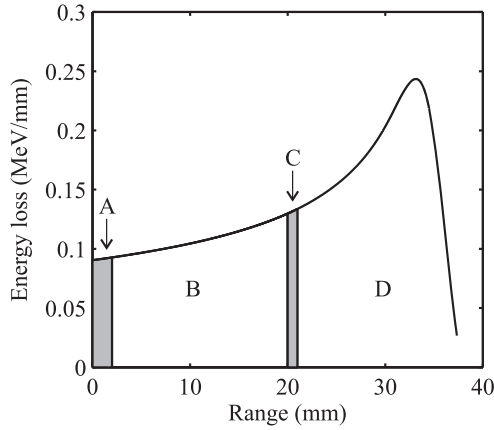


Figure 3. Principle of alpha particle energy loss calculation in UV-gated PIPS measurement. Short ranges just after the emitter (A) and before PIPS (C) detector are not visible to the PMT due to mechanical collimation of the alpha beam. The residual energy (D) is absorbed in PIPS detector and used to estimate the energy loss (B) in the field of view of the PMT. The Bragg curve shown here represents the energy loss of a 5.1 MeV alpha particle in air and it is calculated using the stopping power reported in the NIST Astar database [23].

3. Determination of radioluminescence yield

3.1. Radioluminescence yield of calibrated point alpha emitter

Alpha-particle-induced photons are emitted in an isotropic manner from the vicinity of the radiation source. This point emitter can be approximated as an optical point source if observed from a long distance. Under this assumption, the probability that one alpha particle is detected with the PMT is

$$P = Y \cdot QE \cdot \Omega. \quad (1)$$

Here, Y represents the luminescence yield in photons per particle, QE is the detective quantum efficiency of the PMT, and Ω is the geometrical efficiency of the setup. The latter can be estimated from the ratio of detector window area and the surface area of a sphere that has a radius equivalent to SDD. The absorption of air at these wavelengths is low and can therefore be neglected in the analysis.

The probability of detection can be used to estimate the photon count rate in an experiment where an alpha emitter is observed with a PMT. Now, the alpha emitter surface emission rate A_s has to be included in the equation together with the background count rate N_B . The total count rate is expressed as

$$N_{s+B} = A_s \cdot Y \cdot QE \cdot \Omega + N_B. \quad (2)$$

This equation can be solved for Y to estimate the luminescence yield. In this work, the equation is fitted into experimental data using Y and N_B as free parameters.

The measured net photon count rate (i.e. corrected for the dark counts) is shown as a function of SDD in figure 4. At each point, the gross and dark count rate were determined

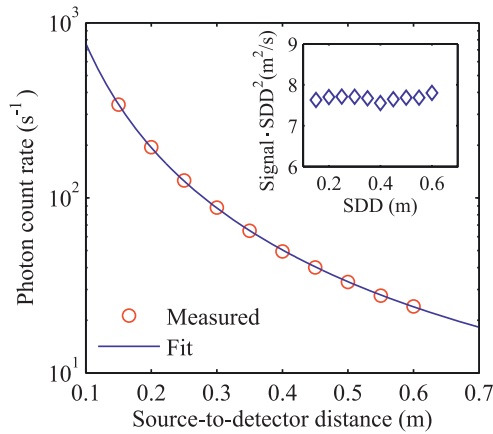


Figure 4. Photon count rate as a function of source-to-detector distance. The values are corrected for the detector dark counts. Inset: net photon count rate multiplied by the square of SDD. The constant value verifies the applicability of equation (2).

separately with the help of the remote-controlled shutter. The acquisition time was adjusted so that the combined statistical uncertainty of the net count rate is less than 0.5% at each point. A nonlinear least squares method was used to fit equation (2) to the data. The resulted yield was 99 photons per alpha particle, and the background count rate was 2.7 pulses per second. This implies that the 5.1 MeV alpha particles observed here produce 19.4 photons per each MeV of energy released in air. A detailed uncertainty analysis is presented in section 4.

The measured points and the fitted curve are in good agreement in figure 4. This verifies that equation (2) describes the signal evolution reliably as a function of SDD. It is necessary to notice that the presented count rates are free from the intrinsic detector background but not totally free from the contribution of scattered photons. These photons give rise to the background term in equation (2) and its average value is revealed by letting N_b float freely in the fitting process. With this method, the effect of reflections is minimal to the value of the luminescence yield estimate Y . The weakness is that only the average count rate of reflections is evaluated and therefore, it is necessary to assume that the contribution is similar irrespective of the position of the radiation source. The validity of this approximation can be tested by using the product of true net count rate and the square of the SDD as a figure of merit. The inset in figure 4 shows the product over the span of different SDDs and the value stays constant. This verifies that the point source approximation is valid and the amount of reflections is reliably estimated.

3.2. Radioluminescence yield as function of deposited energy

In the gated setup, the PIPS detector is triggered only after the detection of an optical photon. This enables the coincident measurement of luminescence yield and the residual kinetic energy of the particle that is absorbed in the detector. With this information, it is possible to estimate the energy that the trigger particle deposited to air. The calculation is based on knowledge of the initial alpha particle energy and stopping power of air, acquired from the NIST database [23].

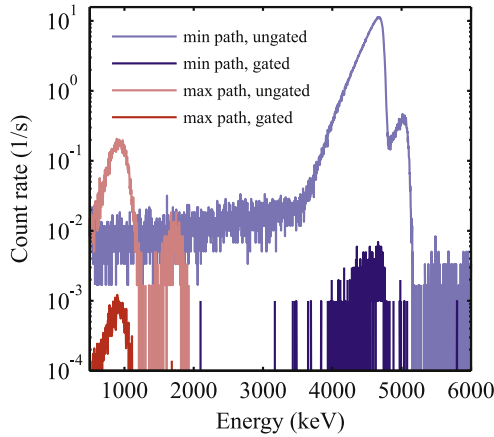


Figure 5. The alpha particle energy spectra in the UV-gated experiment. Both the singles and UV-gated spectra are shown for two measurement points which correspond to the longest and shortest alpha particle path length in air.

In this experiment, the energy loss in air was adjusted by varying the emitter-to-detector distance with a linear translation stage. To demonstrate the effect of UV gating and distance adjustment, the energy spectra of alpha particles in the first and last measurement point are shown in figure 5. The detection efficiency of the PMT was calculated from this information by dividing the alpha peak areas in UV-gated and un-gated singles alpha measurement. The alpha particle luminescence yield is related to this detection efficiency with equation (1).

It is noteworthy that this experiment does not require emitter activity calibration and no assumptions are made on the geometrical distribution of emitted particles. All the observed alpha particles are confined to the cylindrical volume by virtual collimation. The particles that are detected by the PMT but do not hit the PIPS detector are not affecting the result, since they are not included in either spectrum. Instead, a random coincidence between an uncorrelated photon and alpha particle can be recorded. The rate of these events is described with the equation

$$N_{\text{random}} = N_{\text{pmt}} \cdot N_{\text{pips}} \cdot \tau, \quad (3)$$

where N_{pmt} is the count rate of PMT, N_{pips} is the singles count rate of PIPS detector, and τ is the length of coincidence window. According to this model, the expected contribution of random events was always less than 2% of the total count rate at each measured point. The equation was applied in the analysis to correct the measured data for random coincidences.

The photon detection efficiency was measured at nine different emitter-to-PIPS-detector distances, which all represent different energy loss in air. This information was used to calculate the luminescence yields at corresponding energies. Only the part of the alpha track that is visible to the PMT is included in the energy loss calculation (see section 2.3). The resulted data are presented in figure 6 as a function of deposited energy. Linear regression shows that the number of generated photons increases with a slope of 18.5 photons per each MeV of energy released. The constant term in the regression analysis is 1.7 photons per alpha particle which may be attributed to the scattering of photons and systematic uncertainties in the energy

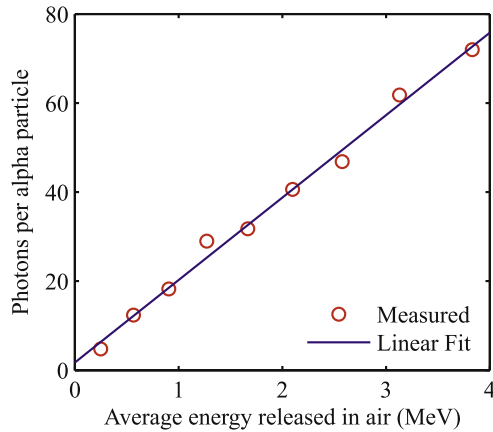


Figure 6. Number of photons as a function of alpha particle energy loss in air. The slope of the fitted line is 18.5 photons per each MeV of energy released in air.

calculation. The result is in good agreement with results obtained in section 3.1, where the yield was measured to be 19.4 photons per MeV. Therefore, it can be concluded that the energy transfer into optical photons is linear in the whole examined range from 0.3 MeV to 5.1 MeV.

3.3. The effect of gas atmosphere

During the experiments above, the humidity, temperature and pressure of the laboratory air were monitored with appropriate instruments (Vaisala, HMP75 and MKS Instruments, A900 PiezoSteel). The relative humidity was measured to be $43 \pm 5\%$ at a 22 ± 0.5 °C temperature and the total pressure was close to 99 000 Pa. The variation in temperature and pressure in indoor environment is expected to be too small to have significant effect on the radioluminescence yield. However, humidity can affect the results, since water molecules, together with oxygen, are effective quenchers for excited nitrogen molecules [15].

In this work, the effect of humidity was briefly investigated with a similar setup as described in section 3.1. Here, a 13 kBq ^{241}Am alpha emitter was placed in an air-tight steel casing and the photon flux was measured through a UV-fused silica window with the PMT. The casing was evacuated with a vacuum pump between experiments and a mass flow controller was used to provide 21 min^{-1} gas flow through the chamber to ascertain gas purity during acquisition. The dimensions of the chamber were too small for absolute yield measurements, but the relative signal strength was recorded in three different gases including laboratory air (RH 46%), dry air (21.4% O_2 in N_2 , Aga gas) and pure nitrogen (99.9999%, Aga gas). All the gases were measured at 21 °C temperature.

The photon count rate of this experiment was intentionally kept low by adjusting SDD to 15 cm and by using a metallic collimator on top of the emitter to reduce the number of particles reaching the field-of-view of the detector. Furthermore, the metallic collimator provided a shield from gamma rays which could induce scintillations in the silica window. The SDD used here ensured that the average number of photoelectrons created per particle was below 0.04 in nitrogen. In this case, the Poisson statistics prove that more than 98% of detected events consist

Table 2. Relative light yield in different gas atmospheres at 21 °C temperature.

Gas	Net count rate (s ⁻¹)	Relative signal
Room air	14.3 ± 0.2	1.00
Dry air	15.3 ± 0.2	1.07
Nitrogen	85.8 ± 0.6	6.00

Table 3. Systematic uncertainties of the experiments.

Source	Uncertainty	Yield uncertainty (3.1)	Yield uncertainty (3.2)
QE of PMT	±12%	±12%	±12%
Radius of detector area	±0.20 mm	±5.4%	±8.1%
Source-to-detector distance	±2 mm	±2.8%	±2.8%
Surface emission rate	±3.2%	±3.2%	—
Total		±14%	±15%

of single photoelectron emissions. Hence, the linear dependence of single photon count rate and photon yield is well justified for all the gases in the analysis. The background-subtracted net count rates are presented in table 2.

The obtained results confirm that the strongest luminescence is observed in nitrogen, which is due to the lack of humidity and oxygen. Secondly, dry air provides 7% more signal than humid room air. However, the difference may be even higher, since the dry air used here had slightly elevated oxygen content. More detailed studies on quenching properties can be found in the literature [15, 20].

4. Uncertainty analysis

The uncertainties of the experiment consist of a systematic and a statistical part. The statistical error in the photon counting experiment of section 3.1 was kept below 0.5% by using long acquisition times. In the gated experiment, a small statistical uncertainty arises from the random occurrence of alpha-photon coincidence events. The total uncertainty due to statistical factors is expected to be small, since best-fit methods are used to unveil the luminescence yield in both analyses.

The most significant systematic uncertainties result from the calibration of the photon counting unit and from the determined geometrical factors. The detective quantum efficiency of the PMT is assumed to have an uncertainty of ±12%. This figure considers the accuracy of typical absolute calibration methods but also leaves marginal for errors that arise from the multispectral composition of nitrogen emission [24]. The geometrical aspects include the radius of the detector active area and source-to-detector distance which together define the photon collection efficiency. In addition, the calibration of the alpha emitter introduces a small uncertainty together with the assumption of uniform alpha emission. However, this does not affect the UV-gated measurement as the optical efficiency is estimated from the ratio of detected alpha particle events. Each systematic uncertainty is presented in table 3 and the total is the sum in quadrature of all the contributions.

In the previous analysis, the photon absorption is considered to be negligible at these wavelengths and short distances. Also within the ionization volume, the absorption is small, since excited molecules are rare and short-lived. Reflections from the emitter planchet are not included because the surface is oriented perpendicularly to the detector window and its reflectivity is fairly low. The good agreement of results further implies that neither emitter reflections nor beta luminescence are a concern in section 3.1. In conclusion, the most significant uncertainty is related to the calibration of the photon counting module.

5. Discussion

On average, the two different experiments show that each MeV of energy released creates 19 photons in normal air with 43% relative humidity. These photons originate mostly from 2P and 1N band systems of nitrogen and they are emitted in the near UV region from 300 nm to 430 nm. The total conversion efficiency from kinetic energy into luminescence is 6.7×10^{-5} if a representative wavelength of 350 nm is chosen for all photons. The obtained radioluminescence yield is higher than in the previous studies [1, 13, 25].

It is known that the role of the primary particle is minor in the final excitation of nitrogen molecules. The absorption of charged particles in air is a process where the initial kinetic energy is transferred to low-energy secondary electrons via a cascade of collisions. These electrons induce the luminescence and their emission cross-sections are known to peak at low energies. The major bands of 2P system are best excited by 15 eV electrons and the emission cross-section effectively vanishes for energies exceeding 100 eV [26, 27]. On the other hand, the excitation of 1N(0,0) band is most efficient at 100 eV and has some tail to above 1 keV [27]. Despite this, the most photons are due to low energy electrons and 2P bands, since the contribution of 1N system is small in the total light yield under normal pressure. For these reasons, it is apparent that luminescence is excited only after a significant number of electron–electron interactions.

The light yield in dry air would be 20 photons per one MeV of energy released, when the measured luminescence efficiency is corrected for the humidity of room air. For comparison, recent studies on electron beams in dry atmospheric air estimate that the luminescence efficiency is between 17.6 and 20.8 UV photons per one MeV of energy released [17–19]. These values are obtained with electron energies ranging from 0.85 MeV up to 50 GeV, and it has been reported that the conversion efficiency is constant over a broad energy range [28]. Given that alpha particles release comparable amounts of energy and through similar interactions as electrons in cited investigations, the similarity of the results is evident. Consequently, these results strengthen the evidence that luminescence yield at high particle energies is first and foremost proportional to the energy loss in air.

6. Conclusions

The aim of this study was to accurately measure alpha particle radioluminescence yield in air. To do so, two independent experiments were conducted, consistently indicating that alpha particles generate 19 ± 3 photons per one MeV of energy released under typical indoor conditions. A linear dependency between photon yield and energy loss is well adopted for electrons in astrophysics and here, it is experimentally confirmed for alpha particles in the

studied energy range from 0.3 MeV to 5.1 MeV for the first time. Furthermore, the determined radioluminescence yield is on the same level with the results of recent electron beam experiments and thus, higher than previously reported for alpha particles. The obtained results are essential for all emerging applications that utilize the UV method for the detection of alpha radiation.

Acknowledgments

The authors would like to thank Kaisa Vaarala for preparing the alpha emitter used in this work, and Seppo Klemola and Roy Pöllänen for the thorough calibration of the emitter. The work was supported in part by Alphamon, a project mainly financed by Tekes, the Finnish Funding Agency for Technology. Other Alphamon funders are Outokumpu Stainless Oy, Rautaruukki Oyj, FNsteel Oy Ab, Senya Oy, Mirion Technologies (RADOS) Oy, and EnviroNics Oy.

References

- [1] Baschenko S M 2004 Remote optical detection of alpha particle sources *J. Radiol. Prot.* **24** 75–82
- [2] Chichester D L and Watson S M 2011 Multispectral UV-visual imaging as a tool for locating and assessing ionizing radiation in air *IEEE Trans. Nucl. Sci.* **58** 2512–8
- [3] Cousins T and Haslip D S 2006 Stand and deliver *CBRNe World Winter* 56–59
- [4] Inrig E, Koslowsky V, Andrews B, Dick M, Forget P, Ing H, Hugron R and Wong L 2011 Development and testing of an air fluorescence imaging system for the detection of radiological contamination *AIP Conf. Proc.* **1412** 393–400
- [5] Lamadie F, Delmas F, Mahe C, Girones P, Goaller C Le and Costes J R 2005 Remote alpha imaging in nuclear installations: new results and prospects *IEEE Trans. Nucl. Sci.* **52** 3035–9
- [6] Ihtantola S, Sand J, Peräjärvi K, Toivonen J and Toivonen H 2013 Fluorescence-assisted gamma spectrometry for surface contamination analysis *IEEE Trans. Nucl. Sci.* **60** 305–9
- [7] Leybourne A E *et al* 2010 Long range detection of radiation-induced air fluorescence *Proc. Inst. Nucl. Mater. Management*
- [8] Huggins W and Huggins L 1903 On the spectrum of the spontaneous luminous radiation of radium at ordinary temperatures *Proc. R. Soc. Lond.* **72** 196–9
- [9] Ave M, Bohacova M, Buonomo B, Busca N, Cazon L, Chemerisov S D, Conde M E, Crowell R A, Di Carlo P, Di Giulio C *et al* 2007 Measurement of the pressure dependence of air fluorescence emission induced by electrons *Astropart. Phys.* **28** 41–57
- [10] Nicholls R W and Reeves E M 1957 Luminescence produced in air by polonium-210 α -particles *Nature* **180** 1188–9
- [11] Birks J B and King J W 1953 The luminescence of air glass and quartz under α -particle irradiation *Proc. Phys. Soc. Sect. B* **66** 81
- [12] Brown L O and Miller N 1957 α -ray induced luminescence of gases *Trans. Faraday Soc.* **53** 748–59
- [13] Duquesne M and Kaplan I 1960 Mesure de la luminescence induite par le rayonnement α du ^{210}Po dans l'air et dans l'eau *J. Physique et le Radium* **21** 708–16
- [14] Bunner A N 1967 Cosmic ray detection by atmospheric fluorescence *PhD Thesis* Cornell University
- [15] Waldenmaier T 2006 Spectral resolved measurement of the nitrogen fluorescence yield in air induced by electrons *PhD Thesis* Forschungszentrum Karlsruhe
- [16] Davidson G and O'Neil R 1964 Optical radiation from nitrogen and air at high pressure excited by energetic electrons *J. Chem. Phys.* **41** 3946–55

- [17] Colin P, Chukanov A, Grebenyuk V, Naumov D, Ndlec P, Nefedov Y, Onofre A, Porokhvoi S, Sabirov B and Tkatchev L 2007 Measurement of air and nitrogen fluorescence light yields induced by electron beam for uhecr experiments *Astropart. Phys.* **27** 317–25
- [18] Lefeuvre G, Gorodetzky P, Dolbeau J, Patzak T and Salin P 2007 Absolute measurement of the nitrogen fluorescence yield in air between 300 and 430 nm *Nucl. Instrum. Methods Phys. Res. A* **578** 78–87
- [19] Abbasi R, Abu-Zayyad T, Belov K, Belz J, Cao Z, Dalton M, Fedorova Y, Hntemeyer P, Jones B F, Jui C C H *et al* 2008 Air fluorescence measurements in the spectral range 300–420 nm using a 28.5 GeV electron beam *Astropart. Phys.* **29** 77–86
- [20] Fraga M M, Onofre A, Pereira L, Castro N, Veloso F, Fraga F, Ferreira Marques R, Pimenta M and Policarpo A 2008 Temperature-dependent quenching of UV fluorescence of N₂ *Nucl. Instrum. Methods Phys. Res. A* **597** 75–82
- [21] van Wyngaardt W M, Simpson B R S, van Staden M J and Lubbe J 2012 Absolute standardization of ²⁴¹Pu by the TDCR technique and effect of the beta spectral shape *Appl. Radiat. Isot.* **70** 2188–94
- [22] Cheung J Y, Chunnillal C J, Thomas P J, Mountford J R and Fox N P 2007 Photon-counting: measurement challenges *Proc. SPIE 6583* **55** 65830G–12
- [23] Berger M J, Coursey J S, Zucker M A and Chang J 2005 *ESTAR, PSTAR, and ASTAR: Computer Programs for Calculating Stopping-Power and Range Tables for Electrons, Protons, and Helium Ions* version 1.2.3 (Gaithersburg, MD: NIST Physics Laboratory) available online at <http://physics.nist.gov/Star> (accessed 20 January 2014)
- [24] Wright A G 1999 Absolute calibration of photomultiplier based detectors—difficulties and uncertainties *Nucl. Instrum. Methods Phys. Res. A* **433** 507–12
- [25] Bachelor P, Jordan D, Harper W, Cannon B and Finn E 2009 Self-absorption effects on alpha-induced atmospheric nitrogen fluorescence yield *J. Radioanal. Nucl. Chem.* **282** 873–6
- [26] Zubeck M 1994 Excitation of the C₃Π_u state of N₂ by electron impact in the near threshold region *J. Phys. B: At. Mol. Opt. Phys.* **27** 573
- [27] Itikawa Y 2006 Cross sections for electron collisions with nitrogen molecules *J. Phys. Chem. Ref. Data* **35** 31–53
- [28] Ave M, Bohacova M, Buonomo B, Cazon L, Chemerisov S D, Conde M E, Crowell R A, Carlo P Di, Giulio C Di, Doubrava M *et al* 2008 Energy dependence of air fluorescence yield measured by AIRFLY *Nucl. Instrum. Methods Phys. Res. A* **597** 46–49

Publication II

J. Sand, S. Ihantola, A. Nicholl, E. Hrnccek, K. Peräjärvi, H. Toivonen, and
J. Toivonen

“Imaging of alpha emitters in a field environment”

Nuclear Instruments and Methods in Physics Research Section A, vol. 782,
pp. 13-19, 2015.

© 2015 Elsevier B.V.

Reproduced with permission.



Contents lists available at ScienceDirect

Nuclear Instruments and Methods in Physics Research A

journal homepage: www.elsevier.com/locate/nima

Imaging of alpha emitters in a field environment



Johan Sand ^{a,*}, Sakari Ihantola ^{b,1}, Kari Peräjärvi ^b, Adrian Nicholl ^c, Erich Hrnccek ^c, Harri Toivonen ^b, Juha Toivonen ^a

^a Tampere University of Technology, Department of Physics, P.O. Box 692, FI-33101 Tampere, Finland

^b STUK – Radiation and Nuclear Safety Authority, P.O. Box 14, FI-00881 Helsinki, Finland

^c European Commission, Joint Research Centre, Institute for Transuranium Elements, P.O. Box 2340, DE-76125 Karlsruhe, Germany

ARTICLE INFO

Article history:

Received 4 December 2014

Received in revised form

22 January 2015

Accepted 26 January 2015

Available online 3 February 2015

Keywords:

Radioluminescence

Air fluorescence

Imaging of alpha emitters

Optical detection of alpha emitters

Stand-off detection of alpha emitters

ABSTRACT

Cameras sensitive to ultraviolet light can be applied to detection of surface contamination induced by alpha particle emitters. When absorbed in air, alpha particles excite nitrogen molecules and the radiative relaxation creates a faint light emission. This radioluminescence can be used for detection purposes, provided that background lighting levels are low. In this work, three low-light sensitive camera technologies (CCD, EMCCD and ICCD) were utilized in a nuclear facility, and their performance in detecting alpha emitters was investigated. The results show that low readout noise is essential for the detection of radioluminescence, as it allows short exposure times to be used. The ICCD camera was found to perform slightly better than the EMCCD camera in the field, while both enable the detection of MBq level alpha activities in 100 s in the test configuration (camera-target distance 0.5 m). Overall, the cameras and techniques used in this study are shown to be effective in detecting alpha emitters in a standard glovebox. This technology can be applied to nuclear security, safety and safeguards, when stand-off detection of alpha emitters is required.

© 2015 Elsevier B.V. All rights reserved.

1. Introduction

Detection of alpha-particle-emitting sources via radioluminescence of air has recently gained increasing interest [1–8]. The technique suits the optical measurement of all ionizing radiations but is especially useful for the detection of alpha particles. This is due to their short range and high ionization capability, which cause the air in the proximity of an emitter to luminesce. Hence, an image taken in total darkness will reveal point emitters as small scintillating hemispheres, whereas widespread surface activity emits light more evenly. The technique is attractive for safety and security purposes, since it enables convenient and remote detection of alpha-particle-emitting materials that are highly hazardous but tedious to detect with conventional means.

The radioluminescence imaging is based on observing optical photons which are induced during the passage of charged particles through air. The most intense light emission occurs in the near ultraviolet (UV) region, between 300 nm and 400 nm, due to the

radiative relaxation of nitrogen molecules [9]. The conversion efficiency of alpha particle kinetic energy into optical radiation is of the order of 20 photons per MeV released in dry air at normal pressure [10]. For this reason, the light emission of alpha emitters is always rather weak, but still strong enough for detection purposes, provided that the level of background UV lighting is sufficiently low. Because the signal is at single photon levels, the intrinsic noise level of the camera sensor has to be low to allow long exposures times. Additionally, high-end readout electronics are required for detection. For these reasons, scientific grade cameras need to be utilized to achieve the desired noise performance and high UV sensitivity.

An emerging method to investigate an area for alpha contamination is to acquire two images, one conventional image under normal lighting and another UV image in complete darkness. Then, the images are processed and superimposed so that the alpha emitters, revealed in the UV image, are seen as bright spots on top of the conventional daylight photograph [3]. The conventional image provides coordinates for the contamination and the UV image contains quantitative information on the activity of the alpha emitter, since the intensity of radioluminescence is proportional to the total energy loss in air of the alpha particles emitted [10]. However, accurate quantitative measurements require exact knowledge of the background lighting level, and therefore, they are best suited for applications where complete darkness is ensured. Also, the self-absorption of the emitter affects the

* Corresponding author. Tel.: +358 50 3777719; fax: +358 3 3115 3015.

E-mail addresses: johan.sand@tut.fi (J. Sand), sakari.ihantola@iki.fi (S. Ihantola), kari.perajarvi@stuk.fi (K. Peräjärvi), adrian.nicholl@ec.europa.eu (A. Nicholl), erich.hrnccek@ec.europa.eu (E. Hrnccek), harri.toivonen@stuk.fi (H. Toivonen), juha.toivonen@tut.fi (J. Toivonen).

¹ Current address: University of Oxford, Department of Physics, Denys Wilkinson Building, Keble Road, OX1 3RH, Oxford, UK.

radioluminescence yield and has to be accounted for when quantitative measurements are conducted [11].

The alpha imaging concept was originally proposed and demonstrated by using conventional film photography techniques [1,2]. Yet the pioneering in-field measurements were published by Lamadie et al., using charge-coupled device (CCD) camera for the purpose [3]. Lamadie et al. applied the method at nuclear facilities at various phases of the nuclear fuel cycle, and also, the characterization of gloveboxes was demonstrated by Mahé from the same group [12]. The imaging detector technology itself has been rigorously developed by Cousins, Ingrid, and others with the focus on security applications [4,6]. Additionally, Chichester et al. have addressed the topic for nuclear safeguards [13] while Feener and Carlton have studied the potential of radioluminescence imaging in nuclear warhead verification [8]. It is evident that the camera-based detection methods have potential users throughout the whole nuclear field, and the decommissioning of old facilities will further emphasize the need for efficient alpha-screening practices in the future. Still, more research and development are needed to facilitate the adoption of optical techniques into widespread use since the method is limited to dim environments.

This work presents the first side-by-side comparison of the most promising camera technologies for imaging alpha-particle-emitting materials. The camera technologies selected are an electron-multiplying (EM) and an intensified (I) CCD, both known to perform well in low-light imaging. Additionally, the conventional CCD readout option is compared with the EM amplifier of the EMCCD camera. To test the true in-field capability of the techniques, the experiments were conducted at a nuclear facility where complete darkness could not be guaranteed. The radioactive samples illustrating the method include mixed-oxide (MOX) nuclear fuel pellets and plutonium nitrate, whereas the quantitative investigations were conducted with well-characterized alpha emitters.

2. Experimental methods

2.1. Camera technology

The electron-multiplying camera selected for this work was iXon3 897 and the intensified camera was iStar 320T, both from Andor Corporation. The cameras utilize a CCD for the imaging sensor but they use a different approach to amplify the initial charge induced by a photon. The EMCCD technology relies on signal amplification on the silicon chip, while the ICCD is based on a traditional image intensifier.

The EMCCD camera has two different output amplifiers. The conventional readout enables the device to be used as a traditional scientific CCD camera when long exposure times can be applied. The EM readout is suited for the measurement of minute amounts of light very rapidly. The detection of weak signals is based on impact ionization during charge transfer in the EM amplifier and it is voltage controlled. The optimum multiplication factor is just high enough to make the number of noise electrons of analogue-to-digital (AD) conversion process negligible compared to the number of signal electrons. For this reason, the most significant noise contributions in this camera type are dark current of the sensor head and electron emission during charge transfer process. The latter can be optimized by selecting high transfer speed to obtain less spurious electrons at the cost of reduced charge transfer efficiency. The camera uses multi-stage thermoelectric cooling to counter dark current and the sensor temperature varied between $-85\text{ }^{\circ}\text{C}$ and $-95\text{ }^{\circ}\text{C}$ during the experiments. Only air cooling was used and the ambient temperature in the laboratory was between $22\text{ }^{\circ}\text{C}$ and $28\text{ }^{\circ}\text{C}$.

The ICCD technology is based on the photoelectric effect. In this camera type, a photoelectron emitted from the photocathode is multiplied in the micro-channel plate (MCP) and the resulting electron cloud produces light in the adjacent phosphor. The image is then acquired with a CCD that is optically connected to the phosphor. The gain of the intensifier is controlled with the voltage applied to the MCP. This camera also utilizes cooling of the sensor to reduce dark current, but the temperature requirements are not as stringent as with the EMCCD, since the signal is already amplified before the CCD. Instead, the most significant noise contribution is the thermal emission of electrons from the photocathode and therefore, the best noise reduction would be achieved by cooling the photocathode. During the experiments, no photocathode cooling was applied but the sensor was electrically cooled to $-35\text{ }^{\circ}\text{C}$.

The major difference between the two cameras is that the EMCCD is based on a silicon sensor (model UVB) which has higher sensitivity to UV light than the photocathode-based ICCD (photocathode model Gen 2 (W-AGT, -E3)). On the other hand, the ICCD reaches its maximum sensitivity in the UV region and cuts off already at 900 nm, whereas the EMCCD exhibits the highest response in the visible region and the tail extends up to 1100 nm. This broad response can be a hindrance, if filters need to be utilized to suppress natural light. The quantum efficiency (QE) curves of the cameras are presented in Fig. 1a together with highlighted near UV region (300–400 nm), where the most intense nitrogen emission takes place. The spectral lines of nitrogen, based on the relative intensity measurements of Ave et al. [9], are shown in more detail in Fig. 1b. According to the data, the average QE for the total radioluminescence signal of nitrogen is 38% and 20% for the EMCCD and ICCD, respectively. Both cameras have high sensitivity to visible light, which is not desirable for UV selectivity, but can be well used to produce conventional photographs to locate radioactive sources.

The imaging lens systems used in this work are a commercially available UV objective and a variety of lens combinations specifically designed for the task. The simple objectives were constructed of plano-convex and aspheric fused silica lenses (e.g. 49-695, Edmund Optics) and used in the demonstrative imaging. These single and two lens configurations provide a good light throughput with a limited field-of-view (FOV). A camera objective (UV1228CM, Kogaku) was acquired for the side-by-side comparison of the cameras. This objective has a focal length of 12 mm and good image quality, but fairly low light collection efficiency (F/2.8).

2.2. Imaging procedure and radioactive samples in-field

The images presented in this work were captured during two different measurement campaigns at the Institute for Transuranium Elements in Karlsruhe, Germany. There, the imaging

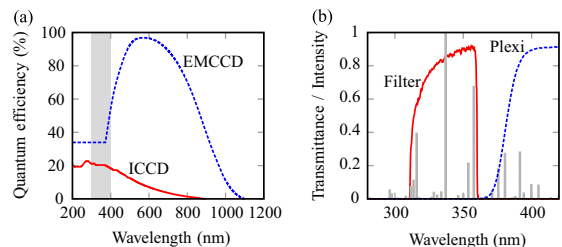


Fig. 1. (a) Quantum efficiency curves of the cameras. The most intense radioluminescence emission is observed in the gray-colored area, at 300–400 nm wavelengths. (b) Transmittance of the glovebox plexiglass and interference filter (Semrock, 334/40). The main nitrogen emission bands are illustrated with gray bars [9].

technique was applied for the analysis of nuclear material in a standard plexiglass glovebox that was not specifically designed for the purpose. The only modification done was the replacement of one glove with a quartz window (Sico Technology GmbH, SQ1). This ensured that at least 90% of the alpha-particle-induced UV light is transmitted through the window. The imaging could also have been conducted through the plexiglass, but this would have attenuated the signal by 80%. The transmittance of the plexiglass was measured with a spectrophotometer (Shimadzu, UV-3600) and it is presented in Fig. 1b.

The light shielding of the glovebox was conducted by using black rubberized fabric (Thorlabs, BK5). A very thorough approach was needed to minimize leaks in the shielding and at least two layers of fabric were required to suppress light from penetrating the fabric. Given that the laboratory had to have some fluorescent lights on all the time, and photons could penetrate the fabric, darkness was not totally ensured. Still, it can be stated that all the images presented here were acquired in a very dark environment.

The radioactive samples imaged during the field experiments included two MOX pellets, one dried Pu nitrate powder sample, a 2 kBq calibration source (Pu-239, Am-241, Cm-244) and a collection of thin planchettes prepared by evaporation of aliquots of Pu-239 solution. The weights of the MOX pellets were 6.4 g and 6.8 g, consisting mainly of UO_2 and PuO_2 with a U to Pu mass ratio of 25.5. The total alpha activities of the pellets were 4.0 GBq and 4.3 GBq at the time of experiments. The Pu nitrate powder was prepared from 80 mg of Standard Reference Material NBS SRM 946 (NIST) by dissolution in HNO_3 and evaporation in a borosilicate glass tube. This sample had a total alpha activity of 0.52 GBq and had a powdery consistency, yielding the brightest radioluminescence emission observed in this work. The surface emission rates of these highly active emitters are not well known because of their thickness, but it is understood that only surface layers can emit alpha particles into air. Hence, the quantitative experiments were

conducted using planchettes which had a thin layer of Pu-239 evaporated on them. The activities of these emitters, verified by alpha spectroscopic measurement in vacuum, were 106 kBq, 280 kBq, 515 kBq, 2.79 MBq, and 5.15 MBq.

2.3. Image processing and analysis

The main steps of image processing are the preparation of UV image and superimposition with conventional photograph. First, all pixels saturated by interactions with gamma and cosmic rays are corrected in the UV image. These pixels are detected with local standard deviation analysis and replaced with intensities equal to their nearest neighbors. Then, a circular averaging filter (diam. 7 pixels) and Gaussian filter ($\sigma=5$) are applied to the UV image in order to smoothen the pixel fluctuations. Finally, an adequate threshold value is selected and exceeding pixel intensities are presented over a grayscale image with a color map that shows the UV intensity. A good threshold value for the minimum color map encoding is usually one to five times the median of all pixels in the UV image, depending on the exposure time and camera parameters. The process is currently automated to a high degree with a Matlab script.

The SNR analysis is done with a method similar to one that is used by Lamadie et al. [3]. In the initial step, the baseline added by the camera software is removed, and signal and no-signal areas are selected from image under investigation. The signal is measured straightforwardly as mean of pixels in the signal area, but the noise figure is extracted through a two-step process. First, a Gaussian-filtered ($\sigma=5$) image is subtracted from the original to leave only high frequency pixel variation present in the image matrix. Then, the standard deviation of all pixels in the no-signal area of the resulted matrix is selected to represent noise. The ratio of these numbers is the definition of signal-to-noise ratio (SNR). All calculations are performed using original data and the aforementioned smoothing techniques are used only for illustrative purposes.

3. Imaging results

In order to visualize the air scintillation in the vicinity of an alpha emitter, a thin 50 kBq Pu-239 sample was imaged with the EMCCD camera before field testing, as shown in Fig. 2a. The electrodeposited sample was placed on top of a steel pole so that the alpha particles fly into the hemisphere just above. The image was acquired in total darkness with a total 3 h exposure time using an EM gain of 50. In addition, a nitrogen purge was used to increase the light emission. The graph paper behind the pole provides a size reference and was removed before the UV exposure. The optically observed range of particles is approximately 38 mm, which is consistent with the range of the 5.1 MeV alpha particles in air. The contours in the image represent UV intensity with an exponentially growing step. Despite the fairly large size of the scintillation bubble, the brightest area is rather small with a radius of 10 mm. The slight elongation in the horizontal direction is due to 13 mm diameter of the emitter active area. Therefore, only the vertical direction is selected to illustrate the relation of UV intensity and distance from the source in Fig. 2b.

The intensity distribution of the experimental UV image was also confirmed by simulating the alpha particle energy loss in the hemisphere above the emitter. The model of random alpha particle tracks is presented in Fig. 2c, where each point has a color encoding that represents the energy transfer of a particle at that point, in accordance with the Bragg curve of Fig. 2d. In order to produce the modeled intensity profile, a 2D projection was calculated from the energy loss point cloud. The profile is similar to experimental result and differs significantly from the Bragg

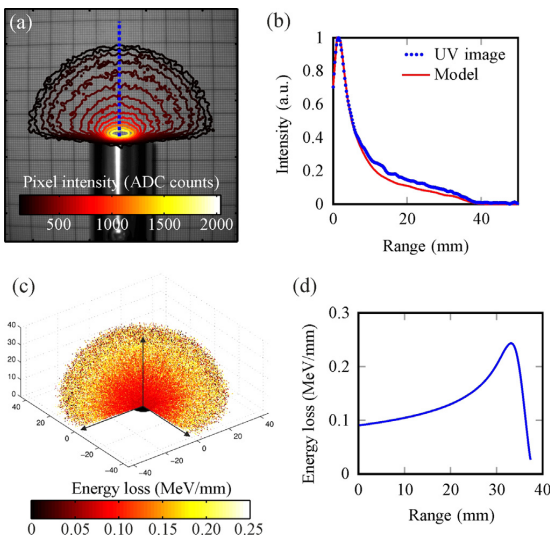


Fig. 2. (a) Scintillation bubble of a 50 kBq Pu-239 emitter imaged under nitrogen purge with 3 h exposure time. (b) The UV signal intensity as a function of vertical distance from the emitter surface, along the dashed line in (a). (c) The energy loss of simulated alpha particle tracks is shown in the vicinity of a 13 mm diameter emitter. The modeled intensity profile in (b) is based on a 2D projection of this energy loss point cloud. (d) Bragg curve of 5.1 MeV alpha particles [14]. (For interpretation of the references to color in this figure caption, the reader is referred to the web version of this article.)

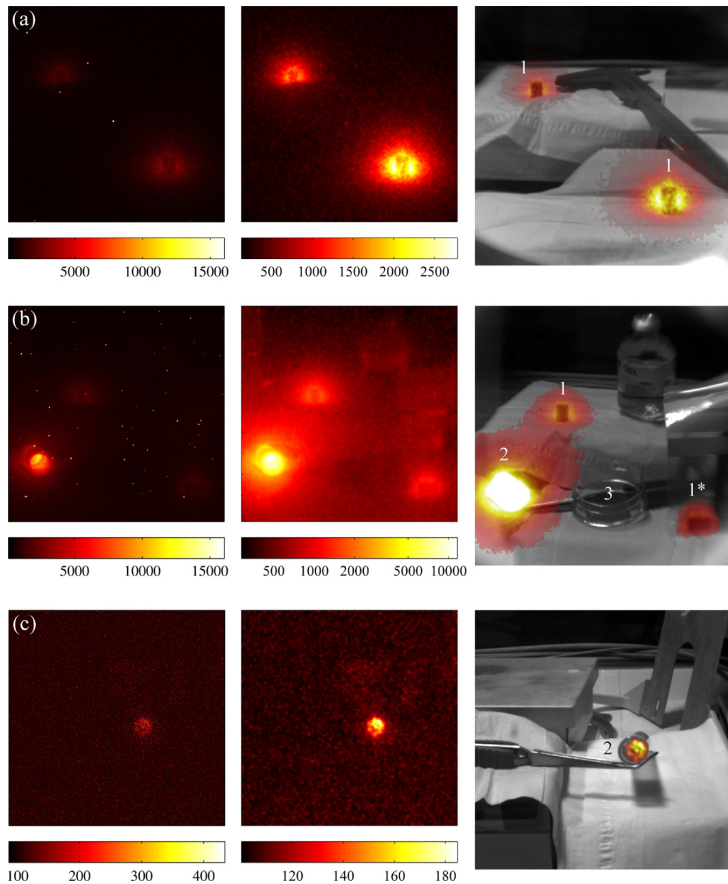


Fig. 3. Images of alpha emitters with EMCCD camera. Left: original images acquired in darkness. Center: same images after processing. Right: superimposition of daylight image and processed UV image. The emitters imaged here are MOX pellets (1), Pu-nitrate in a test tube (2) and 2 kBq alpha calibration source (3). (a) MOX pellets imaged in darkness with 30 s exposure and EM gain of 1000. (b) MOX pellets, Pu-nitrate tube and 2 kBq alpha emitter imaged simultaneously. An EM gain of 300 was used for 100 s exposure. The pellet in the plastic bag (1*) is clearly visible but the 2 kBq alpha emitter is not resolved. (c) Pu-nitrate tube imaged with 0.5 s exposure and EM gain of 1000.

curve due to the higher number of alpha particle tracks per unit volume close to the source. Overall, these observations verify that the imaging technique enables pinpointing of alpha emitters with a spatial resolution better than one centimeter.

3.1. Glovebox imaging

The demonstrative EMCCD imaging of alpha emitters in a glovebox is shown in Fig. 3, together with all major steps of image processing. In the raw images, the small white dots are pixels saturated by interactions with gamma and cosmic rays. These are removed and the smoothing filters are applied to create visually pleasant UV images. Finally the images are superimposed to a conventional photograph for visual presentation of alpha activity.

In Fig. 3a, the MOX pellets are imaged with a 30 s exposure and 1000 EM gain. The light creation close to the pellet surface is brightly visible. Small intensity fluctuations are noticeable because of the high gain and short exposure time used. To demonstrate the dynamics of the method, the plutonium nitrate powder sample was imaged together with the MOX pellets in Fig. 3b. One of the pellets was placed in a plastic bag and the 2 kBq calibration source was added to the area. The UV image was acquired using an EM

gain of 300 for the single 100 s exposure. This yielded an image which is clearly smoother than the previous image with pellets only. The signal intensity of the Pu-tube was 73% of the pixel saturation level. However, the overlaid UV color map presents only 25% of the maximum intensity over the Pu-tube to highlight the details of other emitters, but the intensities can be compared in the UV image. The peak signal of the pellets is 10% of the pixel saturation level, and both are clearly visible in the image. As expected, the low-activity emitter is not resolved at all, since the Pu-tube overwhelms the nearby surfaces with scattered photons. In practical work, the strongest emitters should be removed before significantly weaker sources can be detected. In Fig. 3c, the test tube is imaged alone using a short exposure time of 0.5 s and maximal EM gain. This shows that strong alpha emitters can be revealed very rapidly and safely with a suitable camera.

The setting of Fig. 3c was used to compare the conventional and EM readout options available in the EMCCD camera. Numerous images were captured and three different exposure times (1 s, 10 s and 100 s) are shown for both readout modes in Fig. 4. Additional exposures are included in the presented SNR curves. The gain was set to 300 for the EM amplifier. The net signal of an image consists of values greater than 100 counts, which is the baseline added by

the camera software to mitigate negative pixel values. Visual examination shows that the emitter is barely visible even in the 1 s image with the conventional readout. Yet the benefit of EM amplifier is evident and even more so if weaker emitters are to be investigated, which is also confirmed by the SNR calculations.

The interactions of high-energy gamma rays with the camera sensor create unwanted signal spikes which need to be corrected for the final image, as was done in Fig. 3. The number of the spikes is more pronounced under elevated gamma background and therefore, it can be beneficial to acquire images by summing a number of frames to a single image. This approach reduces the need for post-processing, since frames with saturated pixels can be rejected on-the-fly. Moreover, the summing should not significantly affect the SNR, since the contribution of sensor read noise is low for optimally configured EM- and ICCD cameras. The accumulation of frames is demonstrated in Fig. 5, where (a) and (b) represent images with EM- and ICCD cameras, respectively. Here, the five thin Pu-239 samples were imaged simultaneously. The image series for both cameras consisted of one hundred 1 s exposures. A maximal EM gain of 1000 could be used for the EMCCD, since the average number of photons per pixel was low in

one exposure. The MCP gain voltage of the ICCD camera was adjusted to 3644 V out of the maximum 4000 V.

Only the 5.15 MBq and 2.79 MBq emitters were resolved from the background after the total 100 s exposure time in Fig. 5. The weaker emitters could have been distinguished by increasing the total exposure time and by improving the light shielding, which was likely the main source of background here. In order to get quantitative information on the camera performance, the SNR of the strongest emitter was calculated. The EMCCD camera was able to distinguish this emitter with a SNR of 3 while the ICCD reached 14. The weaker performance of the EMCCD camera may be attributed to its high sensitivity for visible light, which permeated into the glovebox during acquisition. Moreover, it appears that the 1 Hz readout rate had a negative effect on the performance of the EMCCD camera, because the SNR of a single 100 s exposure was shown to be 6 with similar camera parameters (see Fig. 6a). These results validate that both camera types perform well in the experiment, but complete darkness must be ensured to achieve sub MBq detection limits.

The same UV objective was used for both cameras in Fig. 5 and therefore, the difference in FOV is related to the size of imaging

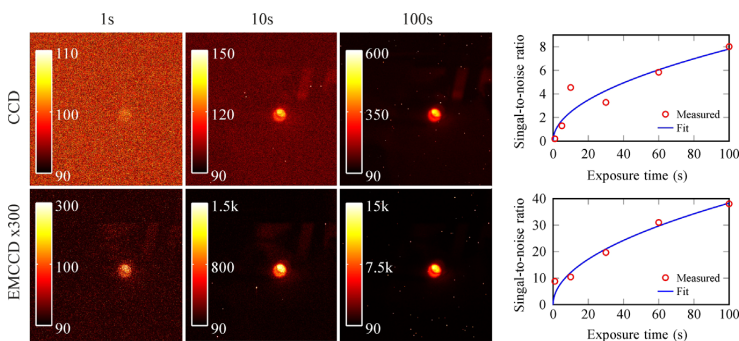


Fig. 4. Test tube containing plutonium nitrate imaged with conventional CCD readout (top row) and with EM gain of 300 (bottom row). The statistical quality of SNR is dominated by gamma-ray-induced spikes especially at short exposure times.

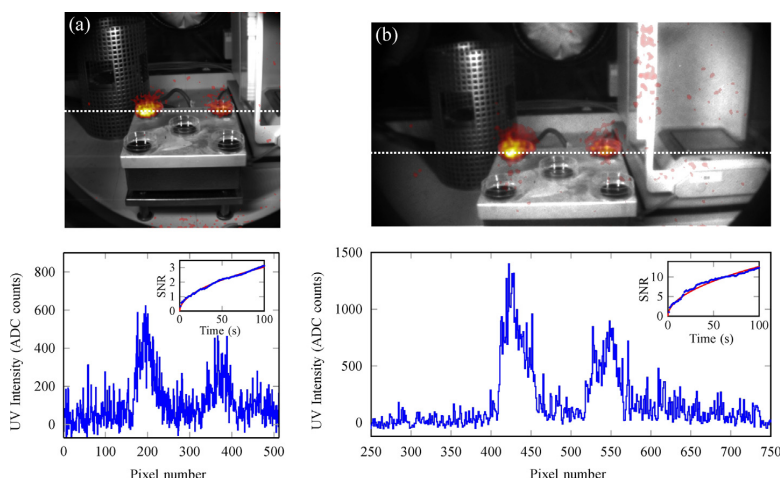


Fig. 5. Alpha emitters deposited on planchettes and imaged with (a) EMCCD and (b) ICCD camera. The exposure time was 100×1 s in both images. The intensity of UV signal along the dashed line is presented below both images. The graphs describe mean value of three vertically adjacent pixels along the line. The insets show the accumulation of SNR over time for the 5.6 MBq emitter, together with best fit lines (\sqrt{t} dependence). Light leaks are visible on white surfaces in both images. Note that the ICCD image has been cropped to half in horizontal direction. The activities are as follows: top left 5.15 MBq, top right 2.79 MBq, front left 515 kBq, front right 280 kBq, and center 106 kBq.

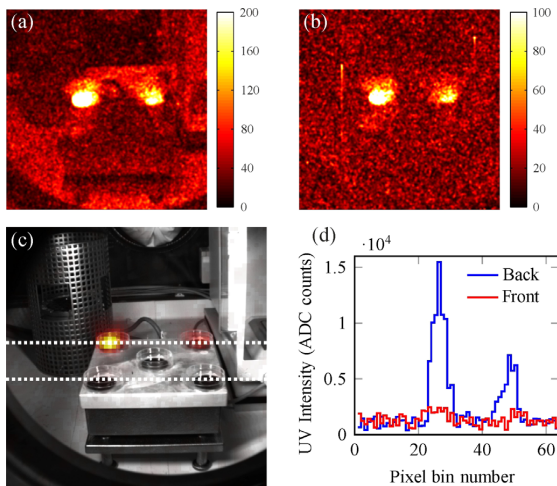


Fig. 6. Alpha emitters imaged with the EMCCD camera and single 100 s exposure. The UV image, when no filters are used, is shown in (a) and with a UV band-pass filter in (b). A smoothing filter has been applied and color maps are adjusted to present only the lower half of the full dynamics of images (a) and (b). The filter decreases the signal level but also the pattern of backlight, visible in (a), is not observed. Figure (c) shows the final superimposition, when a 8-by-8 on-chip pixel binning and the filter was used to enhance SNR. The intensity of UV signal along the dashed lines is presented in (d). (For interpretation of the references to color in this figure caption, the reader is referred to the web version of this article.)

sensor. The ICCD utilizes a rectangular sensor (6.6 mm by 26.6 mm), designed for spectroscopy, whereas the EMCCD has a square sensor (8.2 mm by 8.2 mm). The relation of sensor size and FOV is evident in the ICCD image where horizontal span is increased and vertical span is reduced due to the differences in sensor dimensions. Both cameras have a smaller sensor area when compared with the typical digital single lens reflex cameras. When a large FOV is preferred for inspection purposes, the ICCD technology has the competitive edge since large sensors are readily available. Additionally, the image area can be widened by the selection of input optics, but often at the cost of reduced light throughput or image quality.

3.2. Methods to improve signal-to-noise ratio

The field tests showed that sealing the glovebox from external light is possible but minor light leaks may still occur. Therefore, it is beneficial to add a band pass filter to the imaging system. This can make the acquisition process more selective for radioluminescence light since the spectrum of room illumination is intense in the visible wavelengths and only a small part of the light is in the UV region. The best interference filters can provide several orders of magnitude suppression in the visible range while maintaining high transmittance in the near UV, which can have a drastic effect on background level in low light environment. However, using these filters to suppress full daylight is challenging because of required blocking level and broadness of the spectral range.

A visual example of light leaks is presented in Fig. 6a, where patterns of backlight are clearly present. The color scaling indicates that the magnitude of faint light leaks is comparable to the level of UV light produced by the weakest alpha emitters of the image. Under these conditions, it is beneficial to use additional filtering and here, an interference filter (FF01-334/40, Semrock) was selected for the purpose. The transmittance curve of the filter is presented in Fig. 2b according to vendor specification. Importantly, the pass bands of the filter and plexiglass do not coincide

and hence, the plexi walls of the glovebox operate as an additional filter against UV background. Moreover, three main peaks of the nitrogen emission just fit to the pass band of the UV filter which ensures sufficient signal level. Fig. 6b shows the same sample setting imaged through the filter using original acquisition parameters. Although SNR was now decreased from 6 to 3, due to the calculation method and lower signal level, a visual examination reveals the benefit of filtering. The filter suppressed the pattern of backlight which verifies that it is not scattered UV light from the alpha emitters. This shows that interference filters can be useful for the field work when absolute darkness is difficult to achieve.

A method to increase low-light sensitivity of a camera is to use large pixels which collect more photons. The increased light collection capability comes at the cost of reduced image resolution, but this is acceptable in alpha imaging, since the method is already limited by the size of the scintillation bubble. The cameras of this study have a clear difference in the pixel size as the ICCD sensor has $26 \mu\text{m}$ by $26 \mu\text{m}$ square pixels and the EMCCD sensor has $16 \mu\text{m}$ by $16 \mu\text{m}$ square pixels. The influence of this size difference was not experimentally investigated in this work, but instead, the binning of pixels was demonstrated. This means that multiple pixels are read in one batch. This effectively increases the amount of charge which is passed to the AD conversion unit and also only one read-noise contribution is added to the total charge collected by the pixel bin. The technique is demonstrated in Fig. 6c where the alpha emitters are imaged with the EMCCD camera using a single 100 s exposure, interference filter and 8 by 8 binning of pixels. This increases the SNR of the strongest emitter from 6 to 11 and it also reveals the 515 kBq emitter in the left in front row. When applying the method, optimal results are obtained by taking the conventional images at maximum resolution, and large pixel bins can be used for the UV images to enhance detection limits.

The caveats of pixel binning are the high energy particles which render the affected pixel bin useless for alpha detection. This can be a problem if a single bin represents a significant part of the image area. Moreover, a sum of pixels contains more charge and therefore, the maximum limit of the AD conversion unit is reached more easily. Together these issues indicate that the binning technique works best with accumulation mode, in which the final image is a sum of multiple short exposures. Software methods can only be used to filter large saturated bins if the exposure time is short. Otherwise, they would increase the risk of false negatives.

4. Discussion

The acquired results show that the imaging of alpha emitters in a standard glovebox can be successfully conducted at a nuclear facility. The method can detect emitters rapidly from a safe distance and without exposing personnel or devices to the radiation field. With further development, the technique could be used for streamlined generation of an alpha-specific radiological map at a target facility. This offers new possibilities for a multitude of decommissioning tasks, which are imminent in the near future. The same technology could be directly applied in safety inspection of operational gloveboxes, hot cells and buildings. Moreover, security officials need detection tools for crime scene investigation involving possible radiological contamination, and first responders could utilize similar technology to improve situational awareness.

The radiological map can also advance the work of regulatory authorities. The technique is sensitive to surface activity of alpha emitters, which are hard to detect by other means because of low gamma yields. In nuclear safeguards, an alpha particle specific camera could be used to identify areas favorable for sampling. Imaging could also be used to verify the operational or non-operational status of workspaces at declared facilities to reveal

potential discrepancies. Furthermore, stand-off detection of Pu contamination and material hold up are prospective field applications, as also proposed by Chichester et al. [13].

It is important to note that the existing camera technology is suitable for the aforementioned applications, as long as complete darkness is ensured. Therefore, attention should be paid to decrease daylight sensitivity of the technique in the future. The sensor response characteristics play a key role here and should be tailored for the purpose. The so-called solar blind cameras have a good rejection of daylight but their quantum efficiency overlaps poorly with the strongest nitrogen emission bands. However, these cameras have been demonstrated for the purpose [15]. A novel gallium nitride (GaN) based photocathode is a very promising choice for the detection of alpha emitters since it can exhibit a good quantum efficiency up to 360 nm and then drop rapidly [16]. Together with a carefully designed filtering system, this sensor could provide both high UV sensitivity and good rejection of visible light. Currently, the first GaN based image intensifiers are commercially available [16].

It is clear that more research and development is needed before the method can become a standard inspection tool. While it is not an all-around solution for alpha particle detection yet, it has significant implications related to laboratory analysis of radioactive samples. First of all, the optical method can deliver quantitative information on the surface emission rate of a sample if total light shielding is successfully implemented. Secondly, alpha particles can be detected even under high gamma background, provided that the sensor is well protected. Thirdly, it can do so without direct interaction with the particles, which enables remote measurements and detection through translucent materials. A dedicated laboratory setup could take advantage of these features and also ensure light-tightness. This approach suits to the analysis of medium to high surface activities and to examination of unknown or potentially dangerous samples, packed in UV transparent cases.

5. Conclusions

The superimposition of air radioluminescence image on top of a visible light image is a viable technique to locate and analyze alpha emitting radioactive sources. The method is shown to be applicable at a nuclear facility for the detection of MBq level emitters in a standard glovebox. EMCCD, ICCD and conventional CCD camera technologies have been successfully applied for the purpose, and the SNR and methods to improve it have been studied. The findings show that a sum of short exposures together with on-chip binning and optical filtering is a versatile method to image alpha emitters. It is likely that the rapid development of visible-blind UV sensors will significantly advance the applicability of the method in the near future.

Acknowledgements

The authors would like to acknowledge IAEA task JNT A 1628 MSSP Umbrella Task (Support for Novel Technologies), Cheos Oy, and Andor Technology PLC for providing the cameras used in this work. Special thanks are extended to people at ITU and IAEA for fruitful discussions on the topics listed in the paper.

References

- [1] G. Imbard, J.-F. Pineau, Remote α Source Location Device and Method, US Patent 6,281,502, 2001.
- [2] S.M. Baschenko, Journal of Radiological Protection Volume 24 (2004) 75. <http://dx.doi.org/10.1088/0952-4746/24/1/006>.
- [3] F. Lamadie, F. Delmas, C. Mahe, P. Girones, C. Le Goaller, J.R. Costes, IEEE Transactions on Nuclear Science NS-52 (6) (2005) 3035. <http://dx.doi.org/10.1109/TNS.2005.862911>.
- [4] T. Cousins, D.S. Haslip, Stand and Deliver, CBRNe World Winter, 2006, pp. 56–59.
- [5] A.E. Leybourne, S. Creasey, J. Dixon, J. Lee, G. Messer, S. Neal, G.H. Rayborn, D. Speaks, J. Stephens, T. Strange, C.D. Walker, W.C. West, H.F. Woodruff, C.B. Winstead, Long range detection of radiation-induced air fluorescence, in: Proceedings of the Institute of Nuclear Materials Management, 2010.
- [6] E. Inrig, V. Koslowsky, B. Andrews, M. Dick, P. Forget, H. Ing, R. Hugron, L. Wong, AIP Conference Proceedings 1412 (1) (2011) 393–400, <http://dx.doi.org/http://dx.doi.org/10.1063/1.3665340>.
- [7] D.L. Chichester, S.M. Watson, IEEE Transactions on Nuclear Science NS-58 (5) (2011) 2512. <http://dx.doi.org/10.1109/TNS.2011.2163825>.
- [8] J.S. Feener, W.S. Carlton, Preliminary results of nuclear fluorescence imaging of alpha and beta emitting sources, in: Advancements in Nuclear Instrumentation Measurement Methods and their Applications 3rd Conference, Marseille, France, 23–27 June 2013, pp. 1186–1193, <http://dx.doi.org/10.1109/ANIMMA.2013.6728086>.
- [9] M. Ave, M. Bohacova, B. Buonomo, N. Busca, L. Cazon, S. Chemerisov, M. Conde, R. Crowell, P.D. Carlo, C.D. Giulio, et al., Astroparticle Physics 28 (1) (2007) 41 <http://dx.doi.org/http://dx.doi.org/10.1016/j.astropartphys.2007.04.006>.
- [10] J. Sand, S. Ihantola, K. Peräjärvi, H. Toivonen, J. Toivonen, New Journal of Physics 16 (2014) 053022. <http://dx.doi.org/10.1088/1367-2630/16/5/053022>.
- [11] P. Bachelor, D. Jordan, W. Harper, B. Cannon, E. Finn, Journal of Radioanalytical and Nuclear Chemistry 282 (2009) 873. <http://dx.doi.org/10.1007/s10967-009-0331-0>.
- [12] C. Mahé, Alpha imaging: recent achievements and glove box characterization, in: Decommissioning, Decontamination, and Reutilization Topical Meeting, Idaho Falls, Idaho, USA, 29 August–2 September 2010.
- [13] D.L. Chichester, S.A. Pozzi, E.H. Seabury, J.L. Dolan, M. Flaska, J.T. Johnson, S.M. Watson, J. Wharton, FY09 Advanced Instrumentation and Active Interrogation Research for Safeguards, Technical Report, Idaho National Laboratory, 2009, <http://dx.doi.org/10.2172/974754>.
- [14] M.J. Berger, J.S. Coursey, M.A. Zucker, J. Chang, ESTAR, PSTAR, and ASTAR: Computer Programs for Calculating Stopping-power and Range Tables for Electrons, Protons, and Helium Ions (Version 1.2.3), Online, 2005, URL (<http://physics.nist.gov/Star>) (accessed 20.01.14).
- [15] O.P. Ivanov, V.E. Stepanov, S. Smirnov, A. Volkovich, Development of method for detection of alpha contamination with using UV-camera “DayCor” by OFIL, in: IEEE Nuclear Science Symposium and Medical Imaging Conference (NSS/MIC), 2011, pp. 2192–2194, <http://dx.doi.org/10.1109/NSSMIC.2011.6154448>.
- [16] Photonic Devices Catalogue, Hamamatsu Photonics, 2014.

Publication III

J. Sand, A. Nicholl, E. Hrnccek, H. Toivonen, J. Toivonen and K. Peräjärvi

“Stand-off radioluminescence mapping of alpha emitters under bright lighting”

IEEE Transactions on Nuclear Science, vol. 63, no. 3, pp. 1777-1783, 2016.

© 2016 IEEE.

Reproduced with permission.

Stand-Off Radioluminescence Mapping of Alpha Emitters under Bright Lighting

Johan Sand, Adrian Nicholl, Erich Hrnccek, Harri Toivonen, Juha Toivonen and Kari Peräjärvi

Abstract—Remote detection of alpha emitters is achieved by measuring the secondary radioluminescence light (air fluorescence) that is induced by alpha particles when absorbed in air. A telescope was used to collect the radioluminescence photons to a photomultiplier tube, which is operated in the photon counting mode. Careful matching of photocathode response and filter pass-band allows the sensing of a faint radioluminescence emission in a brightly illuminated environment, which is essential for operative use. A minimum detectable alpha activity of 4 kBq was reached at 1 m distance in 10 s time, when ultraviolet-free lighting is present, and 800 kBq under bright fluorescent lighting. These sensitivities are realized using an ultra-bialkali and cesium-telluride photocathodes in the aforementioned environments respectively. The presented approach is a robust and affordable solution to remotely detect and localize moderate alpha activities in a field environment, providing a means for automated alpha contamination mapping. Moreover, it is shown that a signal increase of more than two orders of magnitude (150-420) can be achieved in deep ultraviolet (close to 260 nm), if nitrogen or argon purge are used to enhance the detection.

Index Terms—radioluminescence, air fluorescence, alpha-particle detectors, optical devices.

I. INTRODUCTION

Effective detection of alpha contamination is a challenge for nuclear safety, security and safeguards (3S). Conventional measurement techniques require direct interaction with alpha particles, which limits the range of detection to a few centimeters. This constraint can be overcome by utilizing the radioluminescence light that alpha particles induce in air. The effect has been known for more than a century now [1], but only since 2001 it has been applied for remote detection purposes by several research groups around the world [2]–[11]. The development of novel, remote alpha detection technologies responds to the increased demand in the fields of 3S. Topical examples of the need for advanced remote sensing are decommissioning of nuclear facilities, as well as detection of radioactive materials at crime scenes [12].

The radioluminescence light of air consists of ultraviolet (UV) photons which are emitted by nitrogen molecules [13].

J. Sand and K. Peräjärvi are with the STUK—Radiation and Nuclear Safety Authority, FI-00881 Helsinki, Finland (e-mail: Johan.Sand@stuk.fi; Kari.Perajarvi@stuk.fi).

A. Nicholl and E. Hrnccek are with the European Commission, Joint Research Centre, Institute for Transuranium Elements, DE-76125 Karlsruhe, Germany (e-mail: Adrian.Nicholl, Erich.Hrnccek@ec.europa.eu).

H. Toivonen was with the STUK—Radiation and Nuclear Safety Authority, FI-00881 Helsinki, Finland. He is now with HT Nuclear Ltd., Notkokuatu 4, FI-05880 Hyvinkää, Finland. (e-mail: Harri.Toivonen@htnuclear.fi).

J. Toivonen is with the Department of Physics, Tampere University of Technology, FI-33101 Tampere, Finland (e-mail: Juha.Toivonen@tut.fi).

Digital Object Identifier 10.1109/TNS.2016.2562359

On average, a single 5 MeV alpha particle creates 100 photons [14] and most of them are observed at the near UV region between 300 nm and 400 nm [13]. The strongest emission lines of nitrogen overlap with the spectrum of sunlight and with typical fluorescent lights, which imposes a strict limitation to wide application of the technique. For this reason, the most demonstrations have been performed in a dark operating environment only. However, light-emitting diode (LED) lamps, low pressure sodium lamps and selected fluorescent lights have adequately low UV emission to allow optical alpha detection in environments which are bright for the human eye. Moreover, the so-called solar blind region shows promise for the detection under normal illumination [15]. The characteristic feature of this wavelength region (220-280 nm) is that the background lighting levels are extremely low. This is explained by the absorption of solar radiation by ozone in the upper atmosphere [16], and by glass absorption, which suppresses deep UV emissions of common light sources.

This work presents a field-capable device that can be used for radioluminescence mapping in an illuminated environment. The device is constructed of commercial off-the-shelf components to achieve a high detection efficiency at a moderate cost. As opposed to several recent alpha imaging studies, the selected approach is to use a narrow-angle, non-imaging configuration. This allows a high light throughput for the optical system and a photomultiplier tube (PMT) to be used as single pixel detector. The device produces radioluminescence maps by scanning its narrow field-of-view (FOV) over the user-defined region of interest while recording the photon count rate point-by-point.

II. DETECTION SYSTEM DESCRIPTION

The optical system is based on the Galilean telescope design to achieve a compact length. The telescope was first designed with a ray-tracing software (FRED, Photon Engineering LLC) and the final assembly was optimized on an optical bench. The objective lens has a diameter of 100 mm and all lenses are made of UV fused silica. The telescope is optimized for high light throughput, and to operate with standard 25 mm diameter filters. The filters are placed between the eyepiece lens and a focusing lens which collects the light onto a PMT photocathode. Figure 1a shows the telescope on top of a motorized pan-tilt head which is used for scanning. The ray-tracing model is shown in Figure 1b to illustrate the locations of the optical components within the telescope.

The optimization of the filter solution is the key element in the current detector design. Optical alpha particle

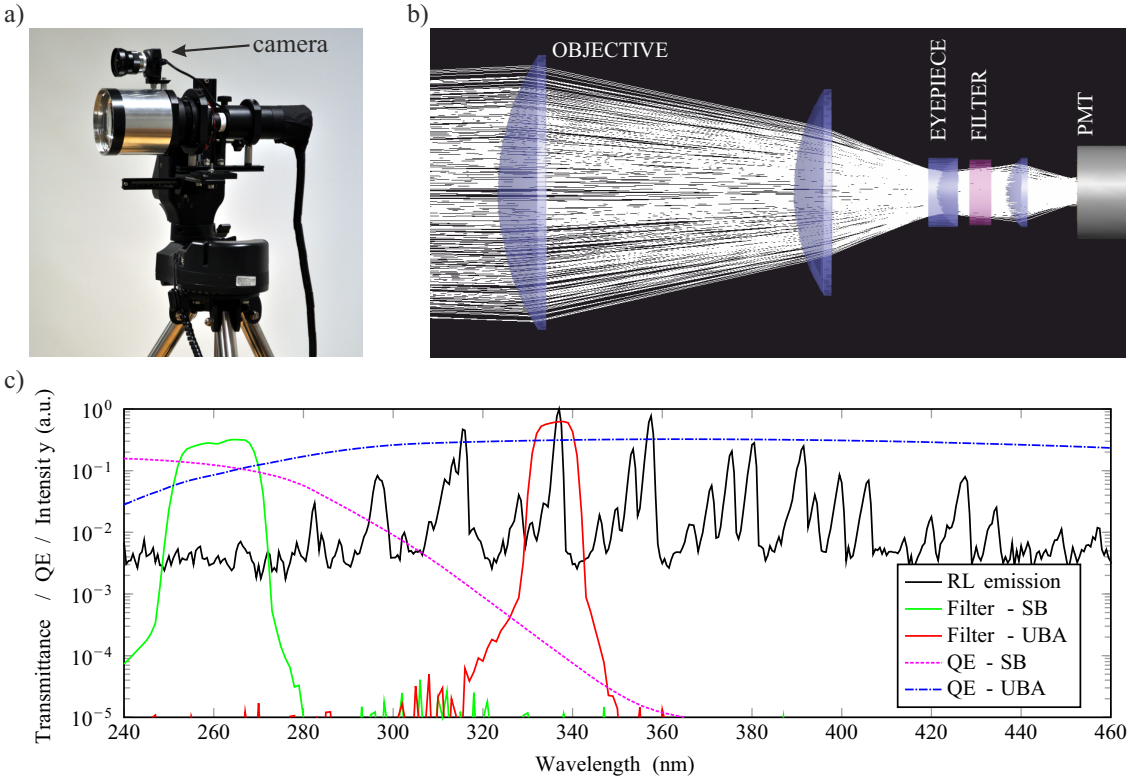


Fig. 1. a) A photograph of the alpha scanning system. The telescope is used for radioluminescence detection while the small camera records visible light images of the scene. b) The ray-tracing model used for telescope design, directly represents the final assembly. c) The radioluminescence (RL) emission spectrum of air excited by Am-241 alpha particles is presented [17]. The emissions below 300 nm are weak but not overlapped by normal light sources. The measured transmittance spectra of filters are shown together with manufacturer-specified quantum efficiency (QE) curves of both PMTs.

detection requires visible light to be heavily attenuated (in excess of 10^{10}) so that the working environment can be kept illuminated during the measurements. Yet the filter should provide a high transmittance at selected UV wavelengths to allow photon counting. Here, this requirement is fulfilled by utilizing multiple consecutive interference filters to achieve the desired rejection in the visible region while maintaining a high transmission of UV light. Two different filter stacks were developed for different environments. The first stack has the transmission center wavelength at 335 nm (FF01-340/12-25 and 2 x FF01-335/7-25, Semrock Inc) and it can be used when artificial, UV-free lighting is available. The other filter set is designed to be used under full fluorescent light and it has the pass-band close to 260 nm (3 x FF01-260/16-25, Semrock Inc). The transmissions of the filter stacks were measured with a spectrophotometer (UV-3600, Shimadzu Corp.) and they are shown in Figure 1c. The spectrophotometer's dynamic range limits the measurement of stop-band blocking level to 10^{-6} although the actual value certainly exceeds 10^{-10} .

The system response depends on the combined efficiency of the filters and photodetectors. Two different PMTs were selected to provide a good match for the selected filter sets.

The near UV detection was performed with a novel ultra-bialkali (UBA) detector (H10682-210, Hamamatsu), which has a quantum efficiency (QE) exceeding 30 % for this wavelength region. Since this photocathode has a high sensitivity also for visible wavelengths, it is important that sufficient stop-band blocking performance is achieved with the filter. A cesium-telluride photocathode PMT (H11870-09, Hamamatsu) was used for the detection in deep UV wavelengths. This photocathode type has a minimal response to wavelengths above 320 nm, and therefore, it is often referred as a solar-blind (SB) detector. The quantum efficiencies are plotted in Figure 1c to emphasize the relation of detector response and filter transmittance. In addition to the photocathode material, the selected PMTs have different size of active area. Therefore, the SB detector (21 mm diameter) has a slightly wider FOV of 3.4° (full width at half maximum, FWHM) compared to the UBA detector (8 mm diameter) which has a FOV of 2.5° (FWHM), with the telescope used. The angles correspond to areas of 28 cm^2 and 15 cm^2 at 1 m distance, respectively.

Both of the PMT modules produce a digital pulse once a photon is detected. Therefore, a counter input of a data-acquisition card and a custom made LabVIEW program were

used for data collection. The LabVIEW program also controls the movement of the pan-tilt system.

III. RESULTS

A. Device calibration

The performance of alpha particle detection was studied using well-characterized alpha emitters at the Institute for Transuranium Elements (ITU, Germany). In total, seven different alpha sources were manufactured for device calibration. The alpha emitter solutions used were calibrated by evaporating an aliquot of the solution on a stainless steel disk and measuring it by alpha spectrometry. Calibration of the alpha spectrometer was done with a certified reference source (AMR.43, Amersham, UK) in the same geometry. Five of the samples had Pu-239 as the main active material and two samples with the highest activity contained Am-241. The measured activities were 0.11 MBq, 0.28 MBq, 0.52 MBq, 2.8 MBq, and 5.2 MBq for Pu-239 samples, and Am-241 activities were 13 MBq and 36 MBq.

A special chamber, originally designed for UV imaging in darkness, was used in the calibration. The chamber is integrated to a glovebox and it has a quartz glass window (SQ1, Sico Technology GmbH) that provides UV transmission to below 200 nm wavelengths. Despite its good transmission, the window causes an estimated light loss of 8 % due to reflections at the interfaces. For the measurements, the planchettes were positioned so that alpha particles interact with air molecules only. The first lens of the detector was kept at 1 meter distance and a counting time of 300 s was used for each sample. The SB measurements were performed without light shielding, whereas the UBA system was isolated from ambient lighting during the experiments.

The measured count rates are shown for UBA detector in Figure 2a and for SB detector in Figure 2b. The data points are corrected for detector dark counts and background, which is present in the SB data only. Moreover, since two radionuclides with different decay energies were used in the experiments, the count rates are scaled to equal 5 MeV alpha particles by using average alpha particle energies for these nuclides (Pu-239: 5.15 MeV and Am-241: 5.48 MeV). The scaling is based on the linear dependance of light yield and energy loss at these energies [14]. A weighted least-squares linear fit (lsqcov, Matlab) was used for the response calibration. The analysis shows that the sensitivity of UBA detector is 820 cps/MBq and the measured background with empty chamber was 4 cps. For the SB detector, the sensitivity is 3.2 cps/MBq, while the measured background without alpha source was 2.4 cps. The observed photon count rates increase linearly with the alpha activity of the source and the goodness of fit (R^2) exceeds 0.99 for both data sets.

B. Radioluminescence mapping

The presented single pixel detector can be used to obtain radioluminescence maps by moving it with the pan-tilt mount. These experiments were performed at ITU with the SB configuration and also at Tampere University of Technology (TUT, Finland), where UV-free lighting is available and both

PMTs could be utilized for scanning. At TUT, a collection of alpha sources with activities of 4.2 kBq, 9.9 kBq, 13 kBq and 32 MBq were used in the experiments.

Figure 3a shows the glovebox-integrated measurement chamber that was used for device calibration at ITU (section III-A). In this Figure, the 36 MBq emitter is placed on a foam stand for a scan demonstration shown in Figure 3b. For the measurement, the telescope was placed at a distance of 1 m from the source and it was programmed to scan over the alpha source with a step resolution of one degree. This step size allows some overlap of adjacent points since the FOV is 3.4° with the SB PMT. The acquisition time per point was 10 s and the obtained average count rate (cps) is presented with colored circles. The circles are overlaid with an image taken with the camera of the scanner system. The experiment was performed under bright fluorescent lighting (450 lux next to the alpha source) and notably, the data show minimal response to the visible light, while the alpha active planchette is clearly revealed by the secondary UV photons.

In order to compare the performance of the selected photocathodes in radioluminescence detection, the telescope system was utilized for additional scan experiments at TUT. The laboratory was equipped with normal fluorescent lighting and one yellow fluorescent light (Osram, L36W/62 Lumilux Chip Control) was used for illumination during the measurements with UBA PMT. This lamp emits very little light at wavelengths below 500 nm [18], [19]. The sample setup is shown in Figure 4a, where sample 1 is a 9.9 kBq smoke detector ionizer and sample 2 is a 5 cm long stripe containing an activity of 32 MBq (both Am-241). The latter is placed into a gas tight chamber which has a UV fused silica window. Sample 3 is a diffusively reflective control surface, coated with Spectralon [20]. It is used to confirm that the ambient light reflected from the sources is insignificant with respect to the radioluminescence emission. It should be noted that these alpha sources were calibrated only by using gamma spectrometry and they have protective surface layers which reduce the energy of alpha particles.

Figure 4b and 4c show the scan results with SB and UBA PMTs, respectively. An integration time of 10 s was used at each point and the figures show radioluminescence maps, which are created by cubic interpolation (interp2, Matlab) from the measured points. As expected, the SB PMT is able to detect activities in the MBq range without being sensitive to fluorescent light (220 lux), but it does not resolve the 9.9 kBq source from the background. In contrast, the UBA PMT offers much higher signal count rate, but it does not tolerate white fluorescent light. Therefore, the yellow light (50 lux) was used for illumination. The combined effect of dark counts and background under this lamp was 5.7 cps on average (in the rightmost third of the scan area), which confirms that the sensitivity for the yellow light is minimal. Moreover, this PMT was able to detect the 9.9 kBq source, which would be better resolved with a different color-scaling. The bright spot at (0,-7) in both Figures 4b and 4c is a reflection from the high level source. These specular reflections can be identified either by polarizing filters or by viewing from another position, but diffuse components may require that high level sources are

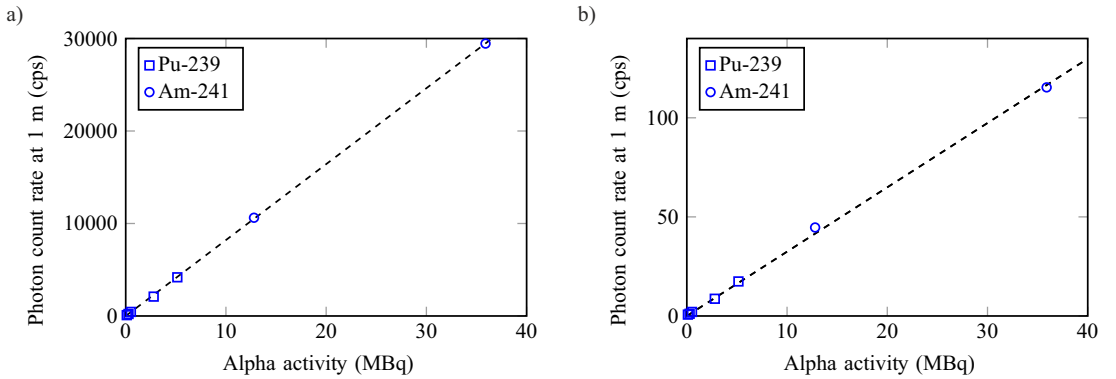


Fig. 2. a) Photon count rate as function of source activity with the detection system using UBA PMT. The slope of the linear fit is 820 cps/MBq. The measured detector dark count rate (4 cps) is subtracted from the data points. b) Photon count rate with SB PMT using same sources. The sensitivity is 3.2 cps/MBq and the combined effect of detector dark counts and background lighting (2.4 cps) is subtracted.

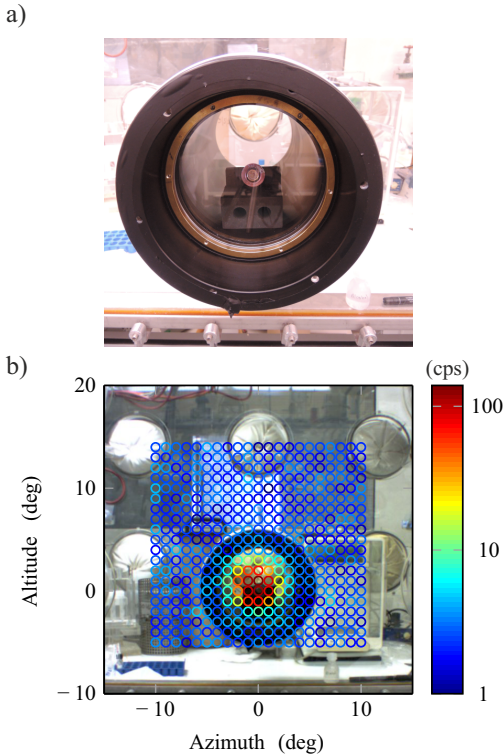


Fig. 3. a) A photograph of the glovebox-integrated measurement chamber containing 36 MBq Am-241 alpha source positioned on stand. A quartz window provides transmission for deep UV light. b) Radioluminescence scan over the alpha source from 1 m distance with 1° steps and 10 s integration. The UV count rate is visualized with the colored circles at each measured point and the points have some overlap since the total field-of-view is 3.4° . The experiment was performed under bright fluorescent lighting with the SB PMT system.

TABLE I
RELATIVE SIGNAL ENHANCEMENT FACTOR IN NITROGEN AND ARGON

	Nitrogen	Argon
UBA (330-340 nm)	10	< 0.2
SB (250-270 nm)	150	420

removed before significantly weaker can be detected.

The detection of kBq level activities was investigated in another experiment with the UBA PMT only. The environment and scan parameters were kept as before, but two additional alpha sources (13 kBq and 4.2 kBq) were used instead of the 32 MBq stripe. The result is shown in Figure 5 where two highest activities are clearly visible but the 4.2 kBq source is at the detection limit. Also, the contribution of the room illumination is more clearly observed in this data set.

C. Effect of gas atmosphere

It is widely known that the radioluminescence emission increases in the absence of oxygen and in noble gases. Therefore, the detector response was briefly studied in nitrogen and argon, which are affordable and used in the nuclear industry. The 32 MBq source, shown in Figure 4, was used for this purpose since it has the required connectors and a gas-tight casing. The source-to-detector distance was 1 m and the yellow fluorescent light was used for illumination. The chamber was flushed with each gas for several minutes before the measurements and a counting time of 300 s was used with a continuous flow. A round 10 mm aperture was added in front of the source for the UBA detector to prevent excessive count rate. The multiplicative enhancements of the observed net photon count rates are shown in Table I with respect to normal air.

In nitrogen, the light emission at 337 nm is increased due to lack of oxygen quenching [13], whereas in the 260 nm region the signal enhancement is likely related to the emission spectrum of nitric oxide, which arises from trace amounts of water in the system. In pure argon, the nitrogen emission at 337 nm is not present, but some photons are still observed

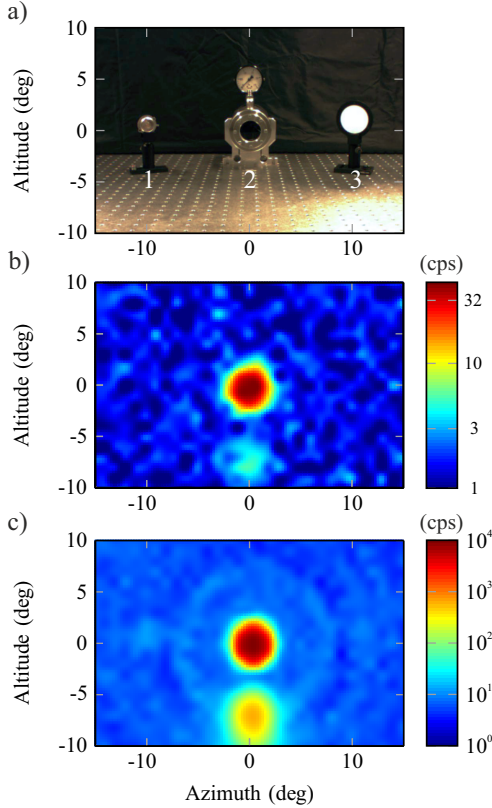


Fig. 4. a) Alpha sources imaged with the scanning system camera. The Am-241 activities are 9.9 kBq (1) and 32 MBq (2). Sample (3) is a control surface for reflected light. b) The above scene was scanned using SB PMT at 1 m distance with 1° steps and 10 s integration per point. The scan data were interpolated with grid resolution of 0.25° and the final radioluminescence map is presented. c) Radioluminescence map with similar parameters using UBA PMT. The 9.9 kBq source gives a weak signal at (-10,0), but it is not well-resolved next to the three orders of magnitude more active source. A specular reflection of source (2) is seen on the table surface at (0,-7).

due to nitrogen impurities in the system. Although argon does not increase the signal for the UBA PMT, its continuum-like emission between 200 nm and 270 nm [21] is very pronounced for the SB detector.

IV. MDA CALCULATION

The minimum detectable activities (MDAs) are presented in table II. The calculations are based on Currie's method [22], when background and sample are measured with 10 s integration time and background count rates are as in section III-A. For nitrogen and argon, the MDAs are calculated by combining the results of sections III-A and III-C. Although only point sources were used for device calibration, the response for homogenous surface contamination is estimated by dividing the point source activities with the area of the device's field-of-view at one meter distance. Furthermore, the calculations suggest that low detection limits of 1-2 Bq/cm²

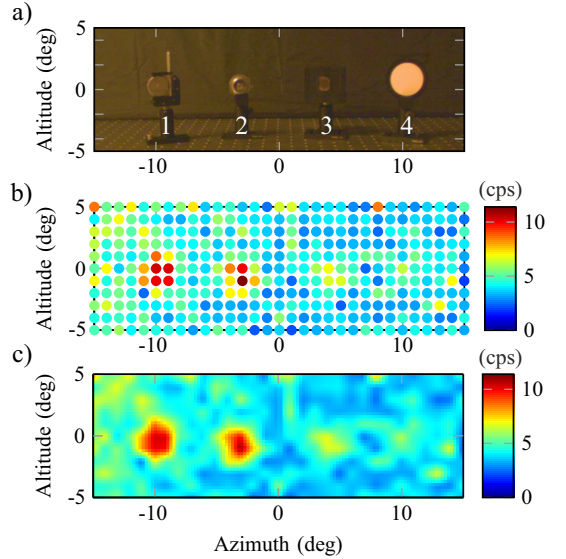


Fig. 5. a) Alpha sources imaged under yellow fluorescent light with the scanning system camera. The samples are 13 kBq (1), 9.9 kBq (2), 4.2 kBq (3), and a diffusely reflective reference surface (4). b) Individual scanned points and their average UV count rates are visualized. The scan was performed with the UBA PMT and 10 s integration. c) The raster of measured points was interpolated with 0.25° grid resolution to create a radioluminescence map.

TABLE II
MDA ESTIMATES AT 1M DISTANCE

	Air	Nitrogen	Argon	
UBA	4 / 0.3	0.4 / 0.03	-	kBq / kBq/cm ²
SB	800 / 30	6 / 0.2	2 / 0.07	kBq / kBq/cm ²

are within the reach of both PMTs if a long integration time of 3 h and a suitable gas environment (UBA: N₂, SB: Ar) are used to enhance the detection. However, the detection of low activities is subject to stability of PMT dark count rate and changes in ambient illumination.

V. DISCUSSION

The results presented in this study demonstrate that faint radioluminescence emissions can be exploited for the remote sensing of alpha sources in a brightly illuminated environment. The goal of the work is to seek options to adapt the technique to the prevalent conditions at nuclear and other facilities to advance translation into operative use. The light sources used in this work are among the most challenging for the technique if direct sunlight (high brightness) and dedicated UV lamps (spectral overlap) are not considered. Importantly, white fluorescent lights are common and they can be replaced with yellow alternatives to obtain more sensitivity for the method. Furthermore, the structure of the demonstration device allows rapid adaptation to any illumination by selecting the filter and PMT accordingly. In short, the sensitivity can be increased for

detection in dim environments and more tolerance for visible light can be achieved at the cost of reduced sensitivity.

The tolerance for visible light was achieved by stacking interference filters to create sufficient blocking of out-of-band wavelengths. However, the filter stacks are not suited for imaging due to multiple reflective layers, and therefore, they are best used with a narrow FOV telescope. A telescope enables high light-throughput and is well-suited for rapid inspection of small areas and items, but screening applications require time. The duration of a scan can be calculated by summing the integration time and settling time of the pan-tilt head (1-3 s) and then multiplying with the number of measurement points. Thus, the combination of integration time, scanning method, and FOV should be optimized in future works.

The scanning procedure is undoubtedly slow because of the narrow FOV of the telescope, but on the other hand, an industrial solar blind camera (DayCor SuperB, Ofil Ltd, Israel) has only slightly wider FOV of $5^\circ \times 3.75^\circ$ than the telescope used here (3.4° diameter with SB PMT). This camera was used by Ivanov et al. [15] to demonstrate the detection of two adjacent 50 kBq alpha sources at 3 m distance with 500 s acquisition, but more data would be beneficial for the analysis of detection limits. When compared with *in situ* measurements at nuclear facilities with UV-sensitive cameras [4], [11], the SB scanning system delivers similar detection performance in the MBq range, but without time consuming light shielding efforts. The limitation of solar blind techniques is that they can be applied only in an open space whereas UV-sensitive scientific-grade cameras enable imaging through most materials that provide at least some transmission of UV light.

To date, the most advanced wide-angle detector operating in near UV wavelengths is called Multi-spectral Imaging System for the Detection of Radiological Contamination (MISDORC) [7]. It is an alpha imaging prototype utilizing multipixel PMTs and a diagonal FOV of 34° . Detection of a 21 kBq alpha source has been demonstrated with this system at 1.5 m distance in 10 s integration time with a good signal-to-background ratio. The prototype has an absorptive filter (UG11, Schott AG) which provides broad transmission (275-375 nm) for several nitrogen emission peaks, but it is also susceptible to even dim LED lighting [23]. Using the relative intensities of nitrogen emissions [24] and manufacturer specifications of the UG11 filter, a signal increase by a factor of 4 for the UBA PMT can be estimated. Furthermore, by utilizing continuous pan at 1.5 m distance with 4 cm/s speed on target, the FOV of MISDORC (0.66 m x 0.66 m) could be scanned with the center FOV of 1.5° in less than five minutes. This ensures a minimum integration time of 1 s on every point of the surface. Considering the enhanced transmission of the filter and losses due to increased distance, a detection limit of 9 kBq for point sources can be expected. The main conclusion of the comparison is that a wide FOV is beneficial for screening purposes but filters suited for imaging are not readily available with desired characteristics.

The effective stand-off detection range of optical detection systems is defined by the photon flux intensity of the radiation source, ambient optical background, and the intrinsic background of the detector. At ground level, the atmospheric

transmission of UV light is sufficient for long range detection at distances of at least hundreds of meters [16]. Therefore, the presented technique is capable of detecting alpha sources at distances much greater than 1 m, provided that the activities are high enough to compensate the photon flux reduction due to geometric scaling ($1/R^2$), as shown in previous studies [3], [5]. It should be noted that the range benefit can be of interest in the detection of other radiations too, since beta particles and gamma rays also cause radioluminescence in the atmosphere. However, their detection is challenging since the energy loss per unit length is significantly smaller than that of alpha particles. Advanced systems for long distance detection with alpha, beta, and gamma sources are presented by Cousins and Haslip in [5].

In the nuclear field, automated alpha scanning is well suited for initial inspection of facilities and installations during decommissioning. Furthermore, the capability to measure through transparent materials enables alpha screening of gloveboxes and some shielded cells from outside the containment [25], provided that the material characteristics are favorable for detection wavelengths close to 400 nm. For these applications, the feasibility has to be investigated separately at each site. Optical monitoring as described in this paper could benefit procedures for the handling of contaminated materials or open sources. In security applications, it could be used for crime scene investigations and radiological reconnaissance during severe incidents. For these purposes, integration to a robotic system is a feasible option, since the system can be made compact and relatively inexpensive.

VI. CONCLUSION

Radioluminescence mapping with a scanning PMT system is an effective method to localize alpha contamination. The results presented in this paper show that point sources of 4 kBq, or homogenous surface contamination of 300 Bq/cm², can be detected under UV-free lighting from 1 m distance in 10 s time. It is also shown that the solar blind region enables detection of MBq activities under bright fluorescent lighting with similar parameters. These detection limits can be significantly enhanced by extending the integration time and by applying a nitrogen or argon purge. If a reduced spatial resolution is acceptable, the sensitivity for homogenous surface contamination could also be improved by increasing the field-of-view of the optical system. The demonstrated scanning system is affordable when compared with scientific-grade UV cameras and its application is straightforward since light shielding requirements are not stringent. Furthermore, the number of peripheral devices is low and it can be operated with little training.

ACKNOWLEDGMENT

The authors would like to thank Ari Laitinen from Tampere University of Technology for support with the 32 MBq americium source. GIFT CBRN project (EU FP7 grant agreement no: 608100) is acknowledged for funding.

REFERENCES

- [1] W. Huggins and L. Huggins, "On the spectrum of the spontaneous luminous radiation of radium at ordinary temperatures," *Proc. R. Soc. Lon.*, vol. 72, no. 477-486, pp. 196-199, 1903.
- [2] G. Imbard, "Remote α source location device and method," US Patent 6 281 502, 2001.
- [3] S. M. Baschenko, "Remote optical detection of alpha particle sources," *J. Radiol. Prot.*, vol. 24, pp. 75-82, 2004.
- [4] F. Lamadie, F. Delmas, C. Mahe, P. Girones, C. Le Goaller, and J. R. Costes, "Remote alpha imaging in nuclear installations: new results and prospects," *IEEE Trans. Nucl. Sci.*, vol. 52, no. 6, pp. 3035-3039, 2005.
- [5] T. Cousins and D. S. Haslip, "Stand and deliver," *CBNe World*, vol. Winter, pp. 56-59, 2006.
- [6] National Physical Laboratory. (2010) NPL builds long range Alpha Detector. Date of access 19.11.2015. [Online]. Available: <http://www.npl.co.uk/news/npl-builds-long-range-alpha-detector>
- [7] E. Inrig, V. Koslowsky, B. Andrews, M. Dick, P. Forget, H. Ing, R. Hugron, and L. Wong, "Development and testing of an air fluorescence imaging system for the detection of radiological contamination," in *AIP Conf. Proc.*, vol. 1412, no. 1. AIP, 2011, pp. 393-400.
- [8] D. L. Chichester and S. M. Watson, "Multispectral UV-visual imaging as a tool for locating and assessing ionizing radiation in air," *IEEE Trans. Nucl. Sci.*, vol. 58, no. 5, pp. 2512-2518, 2011.
- [9] N. Kume, K. Takakura, K. Nakayama, H. Kuroda, M. Izumi, and N. Mukai, "Remote detector of alpha-ray using ultraviolet ray emitted by nitrogen in air," in *Nuclear Science Symp. and Medical Imaging Conf. (NSS/MIC)*. IEEE, 2013, pp. 1-6.
- [10] J. S. Feener and W. S. Charlton, "Preliminary results of nuclear fluorescence imaging of alpha and beta emitting sources," in *3rd Int. Conf. on Advancements in Nuclear Instrumentation Measurement Methods and their Applications (ANIMMA)*. IEEE, 2013, pp. 1-8.
- [11] J. Sand, S. Ihanola, K. Peräjärvi, A. Nicholl, E. Hrnccek, H. Toivonen, and J. Toivonen, "Imaging of alpha emitters in a field environment," *Nucl. Instrum. Meth. A*, vol. 782, no. 0, pp. 13 - 19, 2015.
- [12] R. B. McFee and J. B. Leikin, "Death by polonium-210: lessons learned from the murder of former Soviet spy Alexander Litvinenko," *Seminars in Diagnostic Pathology*, vol. 26, pp. 61 - 67, 2009.
- [13] T. Waldenmaier, "Spectral resolved measurement of the nitrogen fluorescence yield in air induced by electrons," Ph.D. dissertation, Forschungszentrum Karlsruhe, 2006.
- [14] J. Sand, S. Ihanola, K. Peräjärvi, H. Toivonen, and J. Toivonen, "Radioluminescence yield of alpha particles in air," *New J. Phys.*, vol. 16, p. 053022, 2014.
- [15] O. P. Ivanov, V. E. Stepanov, S. Smirnov, and A. Volkovich, "Development of method for detection of alpha contamination with using UV-camera "DayCor" by OFIL," in *Nuclear Science Symp. and Medical Imaging Conf. (NSS/MIC)*. IEEE, 2011, pp. 2192-2194.
- [16] L. Elterman, "UV, visible, and IR attenuation for altitudes to 50 km," Air Force Cambridge Research Laboratories, Hanscom AFB MA (DTIC Document), Tech. Rep., 1968.
- [17] J. Sand and K. Peräjärvi, "Interim report from the solar blind region spectral response studies," Deliverable 1.1.1 of MetroDecom project. European Metrology Research Programme., Tech. Rep., to be published in 2016.
- [18] Osram GmbH, *Technical application guide. Double capped fluorescent lamps: T8, T5 HE and T5 HO, T5 short and single capped fluorescent lamps: T5 FC. Part 1: Products and Technology*, 03.2014 ed., date of access 1.4.2016. [Online]. Available: <http://www.osram.com/media/resource/HIRES/349830/7129720/single-and-double-capped-fluorescent-lamps-english-part-1.pdf>
- [19] —, *Technical application guide. Double capped fluorescent lamps: T8, T5 HE and T5 HO, T5 short and single capped fluorescent lamps: T5 FC. Part 2: Attachments*, 08.2013 ed., date of access 1.4.2016. [Online]. Available: <http://www.osram.com/media/resource/HIRES/349832/6144757/single-and-double-capped-fluorescent-lamps-attachments-english-part-2.pdf>
- [20] Labsphere Inc. Optical-grade Spectralon® reflectance material. Date of access 17.11.2015. [Online]. Available: <https://www.labsphere.com/site/assets/files/2551/a-guide-to-integrating-sphere-theory-and-applications.pdf>
- [21] T. Strickler and E. Arakawa, "Optical emission from argon excited by alpha particles: Quenching studies," *J. Chem. Phys.*, vol. 41, no. 6, pp. 1783-1789, 1964.
- [22] L. A. Currie, "Limits for qualitative detection and quantitative determination. Application to radiochemistry," *Anal. Chem.*, vol. 40, no. 3, pp. 586-593, 1968.
- [23] S. Ihanola, J. Sand, K. Peräjärvi, J. Toivonen, and H. Toivonen, "Fluorescence-assisted gamma spectrometry for surface contamination analysis," *IEEE Trans. Nucl. Sci.*, vol. 60, no. 1, pp. 305-309, 2013.
- [24] M. Ave, M. Bohacova, B. Buonomo, N. Busca, L. Cazon, S. Chemerisov, M. Conde, R. Crowell, P. D. Carlo, C. D. Giulio *et al.*, "Measurement of the pressure dependence of air fluorescence emission induced by electrons," *Astroparticle Physics*, vol. 28, no. 1, pp. 41 - 57, 2007.
- [25] C. Mahé, "Alpha imaging: recent achievements and glove box characterization," in *Decommissioning, Decontamination, and Reutilization Topical Meeting, Idaho Falls, Idaho, USA*, 2010.

Publication IV

S. Ihantola, J. Sand, K. Peräjärvi, J. Toivonen, and H. Toivonen

“Principles of UV-gamma coincidence spectrometry”

Nuclear Instruments and Methods in Physics Research Section A, vol. 690,
pp. 79-84, 2012.

© 2012 Elsevier B.V.

Reproduced with permission.



Contents lists available at SciVerse ScienceDirect

Nuclear Instruments and Methods in Physics Research A

journal homepage: www.elsevier.com/locate/nima

Principles of UV–gamma coincidence spectrometry

Sakari Ihantola ^{a,*}, Johan Sand ^b, Kari Peräjärvi ^a, Juha Toivonen ^b, Harri Toivonen ^a^a STUK–Radiation and Nuclear Safety Authority, P.O. Box 14, FI-00881 Helsinki, Finland^b Tampere University of Technology, Optics Laboratory, P.O. Box 692, FI-33101 Tampere, Finland

ARTICLE INFO

Article history:

Received 12 March 2012

Received in revised form

18 June 2012

Accepted 18 June 2012

Available online 4 July 2012

Keywords:

Remote alpha detection

UV fluorescence

UV–gamma coincidence

Focused spectrometry

ABSTRACT

With conventional methods, samples containing alpha-particle-emitting nuclides are difficult to detect and characterize from distances greater than a few centimetres. One promising technique is to observe alpha particles indirectly by utilizing alpha-induced ultraviolet (UV) photons. While absorbing in air, the energy of alpha particles is transferred to atmospheric molecules, leading to their ionization and excitation. In this work, UV photons generated in the relaxation of nitrogen molecules were used to trigger a gamma-ray spectrometer. This UV approach allows the focusing of gamma-ray measurements on a certain point containing alpha emitters. The present paper demonstrates that the new measurement principle works and has the potential to be developed for both in-field and laboratory applications.

© 2012 Elsevier B.V. All rights reserved.

1. Introduction

Alpha decay primarily populates states with low excitation energy. Therefore, the resulting gamma photons are of low energy, and low-energy photons are easily masked by background radiation. Reliable alpha spectroscopy requires laboratory measurements in vacuum and advanced alpha spectrum deconvolution software [1,2]. In addition, the quality of the sample is crucial, and destructive chemical pre-processing is needed [3]. With an alpha–gamma coincidence approach, the requirements for the sample quality can be loosened [4]. However, this technique is also limited by the range of alpha particles in air. As a result, these isotopes are difficult to detect and identify from distances greater than a few centimeters.

A promising technique for detecting alpha-particle-emitting radionuclides is to measure secondary UV radiation [5]. This radiation is produced when alpha particles are absorbed in air. Each alpha particle generates several UV photons that travel long distances in the air. Unfortunately, two problematic issues remain. First, although photomultipliers provide the best size-to-noise ratio of optical photon detectors, the dark count rate is still relatively high, even in complete darkness [6,7]. Second, the energy of the UV photons does not depend on the energy of the absorbed alpha particle, making identification of the nuclides impossible.

In this work, we demonstrate how these problems can be overcome by combining UV detection with gamma-ray measurement.

Initial tests for this UV–gamma coincidence technique are carried out in both natural- and high-gamma backgrounds. For comparison, the same measurements are repeated with a singles gamma detector, singles UV detector and UV-gated gamma detector. In addition, the possibility to use UV to focus a gamma measurement on a single point in the presence of multiple alpha-particle-emitting sources is investigated.

2. Alpha-induced UV

When alpha particles travel in air, the Coulombic interaction with electrons leads to the ionization of atmospheric molecules. Furthermore, part of the initial alpha particle energy is transferred to the kinetic energy of the ionization-induced free electrons, which in turn produce more ionization and lead to the excitation of atmospheric molecules. Part of these excited states decay by radiating photons, which can be observed as a faint optical emission in the vicinity of an alpha emitter. The excitation mechanism is very similar to that in the northern lights.

Most of the alpha-induced light is emitted in the near-UV region between 300 and 400 nm [8]. This is due to nitrogen molecules, the fluorescence properties of which are well known and have been investigated by several authors [9,10]. Fluorescence emission wavelengths of diatomic nitrogen are determined by the electronic, vibrational and rotational states of the molecule. Under normal atmospheric conditions and after collisional excitation, the 2P and 1N band systems are usually observed. These consist of vibronic (electronic–vibrational) transitions of neutral and ionized nitrogen, respectively. The most intense band heads are at wavelengths of 316, 337, 358 and 391 nm [10].

* Corresponding author. Tel.: +358 9 75988591; fax: +358 9 75988498.

E-mail address: sakari.ihantola@stuk.fi (S. Ihantola).

The fluorescence radiation from nitrogen is effectively quenched by atmospheric oxygen and water vapor [9,10]. Consequently, the reported fluorescence efficiencies for alpha particles are on the order of 10^{-5} in air [11]. However, if a pure nitrogen or noble gas environment is introduced to the measurement, the fluorescence yield will be significantly higher [7,9]. About 30–120 photons in total can be expected when a 5.5 MeV alpha particle is fully absorbed in air [12]. It is difficult to determine the fluorescence yields precisely in different gaseous environments. Such studies are underway, but they are out of the scope of the present paper.

3. Methods used in the analysis

3.1. Comparison of the measurements through peak significance

Two measurements can be compared by calculating the ratio of the peak significances (S). $S=1$ refers to the *a posteriori* decision level according to Currie [13]. An increase in peak significance indicates that the method is more capable of distinguishing small peaks from the background. For two measurements (measurement 0 and measurement 1), the ratio of the peak significances is

$$s = \frac{S_1}{S_0} = \frac{A_1/A_0}{\sqrt{B_1/B_0}} \quad (1)$$

Here, A_0 and A_1 are the areas of the same peak in measurement 0 and 1. B_0 and B_1 refer to the background areas in the energy domain of the peaks. Thus, to increase the capability to detect small peaks, we must increase the ratio of the peak area to the square root of the background area.

To compare the relative power of two different measurement types, we are interested in the ratio of the peak significances when an equal acquisition time is used. This can be done even if the initial acquisition times of the two measurements differ. To calculate this ratio r , both A_i and B_i must be normalized with the measurement time t_i :

$$r = \frac{m}{\sqrt{n}} \quad (2)$$

where

$$m = \frac{A_1 t_0}{A_0 t_1} \text{ and } n = \frac{B_1 t_0}{B_0 t_1} \quad (3)$$

Note that the ratio r defined in this way only depends on the count rates, and is thus independent of the measurement times. If the measurements 0 and 1 are equally long, ratios r and s are identical.

When only relative values of the peak significance are used, the method for determining the areas A and B is arbitrary as long as the same method is used for each spectrum. For the gamma-ray measurements in this study, the peak areas A were obtained by analyzing the spectra with Aatami radionuclide analysis software [14]. The software estimates the true peak area by fitting. The background area B is simply the number of counts at a 1.5–3.0 FWHM distance from the peak center i.e. the sum of counts between 56.0–57.8 keV and 61.3–63.1 keV for a 59.5 keV Am-241 peak.

3.2. Detection efficiency from coincidence measurement

By using the coincidence technique, the detection efficiency for an alpha-particle measurement can be calculated from the peak areas in an alpha-gated gamma measurement and singles gamma measurement. No knowledge of the source is required. Therefore, the uncertainties related to the activity of the source do not contribute to the calculated alpha efficiency.

The number of emitted photons depends on the source activity (a), gamma-ray emission probability (y_γ) and measurement time (t). In a singles gamma spectrum, the peak area (A_γ) is simply the number of gamma rays emitted by the source multiplied by the detection efficiency (ε_γ):

$$A_\gamma = ay_\gamma \varepsilon_\gamma t_\gamma \quad (4)$$

In alpha-gated gamma measurement, only those photons are accepted that are detected simultaneously with an alpha particle. Thus, the peak area ($A_{\alpha\gamma}$) also depends on the alpha-particle detection efficiency (ε_α):

$$A_{\alpha\gamma} = ay_{\alpha\gamma} \varepsilon_\gamma \varepsilon_\alpha t_{\alpha\gamma} \quad (5)$$

Combining Eq. 4 and 5, and knowing that $y_{\alpha\gamma} = y_\gamma$ for nuclides that only decay through alpha-particle emission, ε_α can be expressed as

$$\varepsilon_\alpha = \frac{A_{\alpha\gamma} t_\gamma}{A_\gamma t_{\alpha\gamma}} \quad (6)$$

3.3. Background categories in alpha-gated gamma-ray spectra

The background in alpha-gated gamma measurements is caused by events in true coincidence (B_{true}) and by events in random coincidence (B_{random}):

$$B = B_{\text{true}} + B_{\text{random}} \quad (7)$$

Background events in true coincidence can be further divided into two categories ($B_{1,2}$) and events in random coincidence into four categories ($B_{1,2,3,4}$) with different origins. The first category, B_1 , for both true and random background describes the background originating from the source itself. The second category, B_2 , is fully independent of the source, and it consists of counts caused by the external radiation or detector noise. The categories B_3 and B_4 represent the random coincidences between the signal from the source and the signals of external origin; the B_3 background is produced when the source triggers the alpha detector and the gamma detector instantaneously sees an external gamma photon. B_4 originates, for example, from the random coincidence of alpha detector noise and gamma radiation from the source.

Formally, the equations for the background in true and random coincidence can be written as

$$B_{\text{true}} = c \underbrace{a^S y_{\alpha\gamma}^S \varepsilon_\alpha^S \varepsilon_\gamma^S t}_{B_1} + a^e \underbrace{y_{\alpha\gamma}^e \varepsilon_\alpha^e \varepsilon_\gamma^e t}_{B_2} \quad (8)$$

and

$$B_{\text{random}} = \underbrace{(a^S y_\alpha^S \varepsilon_\alpha^S)(a^S y_\gamma^S \varepsilon_\gamma^S) \tau t}_{B_1} + \underbrace{(a^e y_\alpha^e \varepsilon_\alpha^e)(a^e y_\gamma^e \varepsilon_\gamma^e) \tau t}_{B_2} + \underbrace{(a^S y_\alpha^S \varepsilon_\alpha^S)(a^e y_\gamma^e \varepsilon_\gamma^e) \tau t}_{B_3} + \underbrace{(a^e y_\alpha^e \varepsilon_\alpha^e)(a^S y_\gamma^S \varepsilon_\gamma^S) \tau t}_{B_4} \quad (9)$$

Here, c is a gamma-detector-specific constant, a is the activity, of which a portion y takes place through a particular emission, and ε is the detection efficiency. The superscripts S and e refer to the source and external radiation, respectively. The subscript α in the branching ratios (y) denotes alpha-particle emission, γ gamma-photon emission and $\alpha\gamma$ alpha-particle emission followed by a gamma-photon emission (true coincidence). In efficiencies, the subscripts α and γ specify the detector type. τ is the coincidence resolving time, which is proportional to the length of the gate pulse t is the acquisition time.

The most dominant baseline type depends on the measurement. The external baseline typically dominates in singles gamma measurement without a proper lead shield. In contrast, the detection of alpha particles from external sources is easy to

prevent in alpha-gated gamma measurement due to the short range of alpha particles. Therefore, the background categories depending on ε_x^2 are typically close to zero (B_2 and B_4). In a gated measurement, the baseline categories in random coincidence (B_{random}) also depend on the coincidence resolving time τ . Thus, by using a small enough gate time, these categories become negligible. The only category that cannot be decreased by the coincidence technique is $B_{1,\text{true}}$.

4. Measurements

The measurement setup consists of a UV- and gamma-photon detection system. The UV detector is enclosed inside a cardboard box ($600 \times 250 \times 220 \text{ mm}^2$) together with the radioactive sources. The box is needed to shield the UV detector against external light. During the measurements, the box is connected to a supply of pure nitrogen providing a constant flow rate of $15 \text{ dm}^3/\text{min}$. Before measurements, the count rates recorded by the UV detector were monitored to verify the saturation of the nitrogen concentration inside the box. Pure nitrogen was used to enhance the UV signal, but the effect of room air on the signal was also tested. The gamma detector is located outside the light shield. The geometry of the measurement setup without the light shield is presented in Fig. 1.

A channel photomultiplier (MH-982P, Perkin Elmer) with a low-noise bialkali photocathode is used to detect the alpha-induced UV emission. The manufacturer's stated value for quantum efficiency of this detector is 18% at 410 nm and the quartz glass window has a high transmission down to 165 nm. The diameter of the window is 8.5 mm. The channel structure enables photon counting with a measured average dark count rate of less than 2 counts per second. The collection efficiency of the system is further improved with a 50.8 mm diameter lens (LA4464, Thorlabs), which guides incoming UV rays to the photocathode with a focal length of 60 mm. The internal transmission of this UV-fused silica lens is better than 90% at relevant wavelengths, and reflection losses of about 4% are expected on both surfaces. The photomultiplier tube

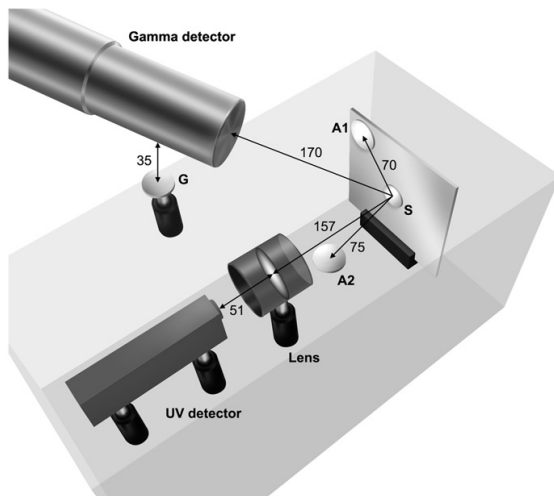


Fig. 1. Geometry of the measurement setup. S, G, A1 and A2 refer to sources described in Table 1, and they were only used in some measurements. The box used for light shielding is illustrated with transparent walls. The distances are in millimeters with an uncertainty of $\pm 1 \text{ mm}$.

is operated in the photon counting regime (2400 V), and after detecting a photon, an 8 μs step signal is passed to a pulse counter and to the gate of the gamma detection system.

The gamma detection system consists of a coaxial HPGe detector (30% efficiency), preamplifier, linear amplifier and multi-channel analyzer. During the experiment, a 1.5 μs shaping time was chosen as a trade-off between the spectrum resolution and anomalies on high count rates. A longer shaping time also increases the length of the gate pulse required, resulting in a higher probability for random UV-gamma coincidences. Depending on the measurement, the multichannel analyzer is set to record either all pulses or only those pulses in coincidence with the gate signal.

The properties of the radioactive sources used in the measurements are presented in Table 1 and their positions during the measurements in Fig. 1. The source S is the actual source of interest, and it is located in the focus of the UV detection system. Am-241 emits 59.5 keV gamma photons in coincidence with 5.5 MeV alpha particles. The gamma branching ratios of the other nuclides present in the source S are negligible, and they can therefore be considered as pure alpha emitters. Note that not all sources were in use in every measurement.

The following measurements with different measurement setups were performed:

1. *Singles UV.* In these measurements, the gamma detector was not utilized; instead, the performance of the UV detection system was tested alone. During the measurements, the cardboard box was either filled with pure nitrogen or normal room air. The measurements were performed both with and without the source S to evaluate the signal and the background.
2. *UV- γ coincidence in natural gamma-ray background.* The sample S was measured with the UV- γ coincidence setup in natural gamma background. Fig. 2b presents the UV-gated gamma spectrum obtained in a measurement of 3903 s, and Fig. 2a the corresponding singles gamma spectrum. The singles gamma measurement was stopped after 702 s of acquisition, since the 59.5 keV peak of Am-241 was already clearly visible. The dead-time of the measurements was less than 1%.
3. *UV- γ coincidence in an increased gamma-ray background.* The measurement described above was repeated in an elevated gamma background by adding the source G next to the gamma detector. Fig. 3 presents the measured gamma-ray spectrum without (a) and with (b) the UV gate. Due to the high gamma count rate, the dead-time of the measurements was almost 10%.
4. *UV- γ coincidence in the presence of multiple alpha sources.* To test the ability to focus gamma-ray measurements in a single point by using a UV gate, two extra Am-241 sources (A1 and A2) were added near the source S. The measurement was repeated both with and without the UV gate.
5. *Blank.* A singles gamma-ray measurement and UV-gated gamma-ray measurement were also performed without any

Table 1
Activities of the sources used in the measurements.

Source	Isotope	Activity (Bq)
S	Am-241	1720 ± 130
	Pu-239	1890 ± 140
	Cm-244	592 ± 55
	Ba-133	$\sim 90,000$
G	Cs-137	$\sim 300,000$
	Co-60	$\sim 30,000$
	Am-241	$\sim 10,000$
A2	Am-241	$\sim 10,000$

radioactive sources. In these background measurements, a 10 min acquisition time was used.

5. Analyses

Table 2 presents the Am-241 59.5 keV peak and baseline areas in the spectra. In singles UV measurements, the signal is the recorded number of counts minus the count rate without the source. The UV baseline areas were obtained from blank measurements. In a blank singles-gamma and UV-gated gamma measurement, the background

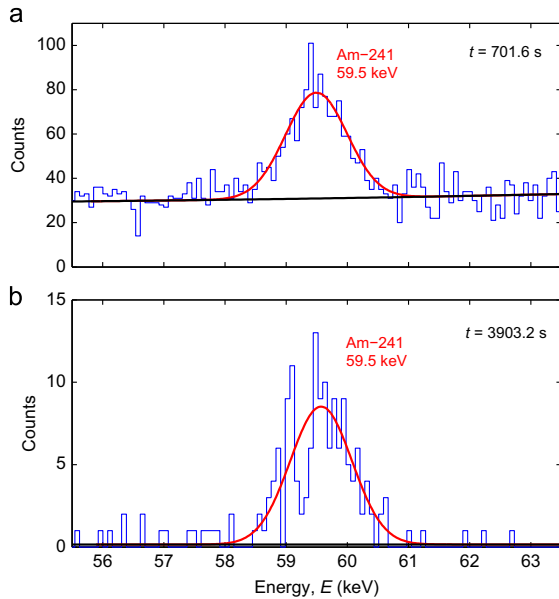


Fig. 2. Am-241 spectra measured in a natural gamma-ray background. (a) Singles gamma-ray spectrum. (b) UV-gated gamma-ray spectrum. For details, see Table 2.

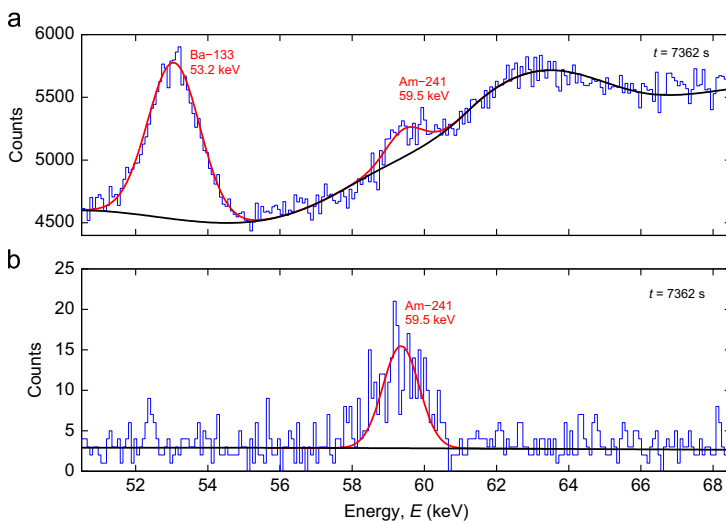


Fig. 3. Am-241 spectra measured in a high gamma-ray background generated with external sources. (a) Singles gamma-ray spectrum. (b) UV-gated gamma-ray spectrum. For details, see Table 2.

is given as the total number of counts from 10 to 300 keV due to the marginal number of counts in the gated spectrum.

5.1. Source detection with the UV detector alone

According to the tests carried out with the UV detector alone, the UV detection system clearly detected the source S. In nitrogen, the 4200 Bq source at a distance of 157 mm from the detector optics produced a UV signal over 150 times greater than the background signal measured without the source. Even in air, the signal was still clearly detectable, being over 30 times the background count rate. Chamber gas had no influence on the background signal of the UV photomultiplier tube.

Excellent alpha detection efficiency can be obtained by measuring secondary UV radiation. The probability of detecting a single alpha decay with the UV detector was calculated to be 0.036 ± 0.005 in nitrogen. The calculation was performed according to Eq. (6) by dividing the count rate at the 59.5 keV Am-241 peak in the gated gamma spectrum with the rate at the same peak in the singles spectrum. The calculated efficiency agrees with the value estimated by dividing the count rate of the UV detector with the total activity of the source. In air, the probability of detecting a single alpha decay was estimated to be 0.006 ± 0.001 . The high efficiency in nitrogen is caused by the large number of UV photons produced per alpha decay. For comparison, the solid angle of the lens from the source was only 0.08 sr (fractional area 0.006).

5.2. Influence of the UV gate on peak significance

Table 3 compares the peak areas in UV-gated and singles gamma measurement. In all measurements involving the UV gate, the baseline was reduced more than the peak. Thus, the signal-to-noise ratio was always enhanced ($m/n > 1$). This clearly shows that the UV gate is capable of discriminating the background. On the other hand, using the UV gate did not always increase the peak significance. In a natural background, the UV gate slightly reduced the peak significance. When the background level was increased with external gamma-ray emitting sources and the measurement was repeated, the use of the UV gate almost doubled the peak

Table 2
Acquisition real time (t), peak area (A) and baseline area (B) in different measurements.

Sources	Measurement type	t (s)	A	A/t (1/s)	B	B/t (1/s)
S	Singles UV (in air)	60	1510 ± 39	25.2 ± 0.6	49 ± 7	0.8 ± 0.1
S	Singles UV (in N2)	60	7485 ± 87	125 ± 1	48 ± 7	0.8 ± 0.1
S	Singles γ	702	706 ± 43	1.01 ± 0.06	$2\,039 \pm 45$	2.91 ± 0.06
S	UV- γ coincidence	3903	144 ± 13	0.037 ± 0.003	17 ± 4	0.004 ± 0.001
–	Singles γ	600	0	0	$118\,410 \pm 340$	197.4 ± 0.6
–	UV- γ coincidence	600	0	0	4 ± 2	0.007 ± 0.003
S,G	Singles γ	7362	4984 ± 1994	0.7 ± 0.3	$334\,932 \pm 580$	45.49 ± 0.08
S,G	UV- γ coincidence	7362	249 ± 21	0.034 ± 0.003	213 ± 15	0.029 ± 0.002
S,A1,A2	Singles γ	604	14210 ± 130	23.5 ± 0.2	2487 ± 50	4.12 ± 0.08
S,A1,A2	UV- γ coincidence	2762	119 ± 11	0.043 ± 0.004	10 ± 3	0.004 ± 0.001

Table 3
Ratios of different quantities between alpha-gated and singles gamma-ray spectra: m denotes peak areas, n baseline areas, m/n signal-to-noise ratios, and r peak significances. The values have been calculated from the data in Table 2 according to Eqs. (2) and (3).

Measurement setup	m	n	m/n	r
Natural background	0.037	0.0015	24	0.95
High background	0.047	0.00064	74	1.9

significance. Furthermore, the non-linear baseline caused by the external gamma emitters reduced the reliability of the Am-241 peak area analysis in singles gamma spectrum. In the UV-gated spectrum, the nonlinearity of the baseline stayed negligible.

The dominating baseline in UV gated measurement depends on the intensity of the background (see Eqs. 7–9). In an increased gamma background, the baseline categories in random coincidence (B_3 in particular) dominate. Thus, the UV gate can effectively reduce the background. According to the measurements performed without any sources, the UV gate reduces the external random background by a factor of 30,000. In a natural gamma background, the external background also dominates in the singles spectrum, but is not drastically larger than the baseline caused by the Compton continuum of the peak of interest. Since the coincidence technique has no influence on $B_{1,true}$, the UV gate reduces the baseline more effectively in a high-gamma background than in a natural gamma background.

5.3. Source location

The source-locating capability of an uncollimated gamma-ray detector is poor. When two extra Am-241 sources were added next to the germanium detector, the count rate on the 59.5-keV peak became 21 times higher. The activity of the extra sources was about 10 times higher compared to the activity of the original Am-241 source of interest. Thus, the gamma detector equally measured radiation from all sources present.

The UV-gated gamma-ray detector allowed the gamma-ray measurement to be focused on a single point. With the UV gate, the extra sources increased the count rate on the 59.5 keV peak only by about 20% compared to the measurement performed without the extra sources. The random coincidence rate is estimated to be 0.02 c/s by using B_3 in Eq. (9). This upper limit estimate has been obtained by using the length of the gate pulse as the coincidence resolving time ($\tau=8\ \mu\text{s}$), and it corresponds to an increase of about 60% in the Am-241 peak area. Therefore, the random coincidences between the alpha particles from the source of interest and gamma rays from the extra sources fully account

for the detected increase on the 59.5 keV peak count rate in the UV-gated spectrum.

6. Enhancement of the setup

The measurement setup used in the experiments was far from optimal. In particular, the background signal could be reduced in various ways. First, the gate time was longer than required. With the very same equipment, the gate time could be reduced from $8\ \mu\text{s}$ to $1\ \mu\text{s}$ without affecting the peak resolution or the risk of losing real pulses. Second, since the calibration source S contained three different isotopes (see Table 1), only about 40% of the alpha particles triggering the gate originated from Am-241. Therefore, using a pure Am-241 source would result in a lower background. These two changes alone would cut the most dominant background category (B_3) by a factor of 20. Consequently, the peak significance of a gated spectrum may become over four times higher.

By using different measurement equipment, the background level could be further decreased. A germanium detector with larger peak-to-Compton ratio would reduce the $B_{1,true}$ background that cannot be influenced by the coincidence technique. Using a photomultiplier with a lower dark count rate would only have a minor effect, since the pulse rate caused by the dark counts was already low compared to the pulse rate caused by the source.

The total signal level could be easily improved by increasing the UV detection efficiency (see Eq. (5)). With a larger lens and photomultiplier tube with a larger entrance window, the UV detection efficiency could be easily improved by a factor of five. On the other hand, the quantum efficiency of the photomultiplier tube was only 18%, which is about half of the quantum efficiency of the best tubes on the market [15]. Since the UV signal measured in nitrogen was about 5 times higher than the UV signal measured in air, these changes would allow the peak significances now measured in nitrogen to be achieved in normal room air. Note that the equipment required to achieve these improvements is available off-the-shelf. Although the gamma detector used was not efficient for Am-241 gamma rays, it has no influence on the relative results presented in this article, since it equally affects the singles and gated measurements.

7. Discussion and conclusions

The UV gate focuses the gamma-ray measurement on a single point, rejecting gamma radiation coming from other sources in the surroundings of the detector. Triggering the gamma detector with UV photons was shown to reduce the gamma-ray background. In the presence of a high gamma background, the peak

significance for alpha-particle-emitting radionuclides was larger in a UV-gated gamma-ray spectrum than in a singles gamma-ray spectrum measured with the same geometry. Therefore, the use of the UV gate helps in detecting small activities.

Even though the measurements were performed in complete darkness and in pure nitrogen, the technique has the potential to be developed for practical applications. Calculations showed that comparable performance could also be achieved in normal room air. In addition, by filtering the wavelength of the recorded UV radiation, the measurements could also be performed in dim LED lighting. An ideal optical alpha-detection filter would transmit the most intense emissions of nitrogen fluorescence spectrum at 316, 337 and 358 nm. Furthermore, this filter should have a superb blocking in the visible region. Suitable filters are commercially available off-the-shelf (for example Semrock FF01-320/40) or can be ordered custom made. This opens up the possibility to build portable devices relying on this technique.

Because the number of counts per second remains low in the coincidence measurement, the method is better suited for source characterization than for searching. On the other hand, when no isotope-specific information is needed, alpha detection based on UV alone works well. Thus, the UV signal could first be used to find locations containing alpha-emitting isotopes. Then, when these locations are found, the UV–gamma coincidence technique could be used for detailed analysis of the isotopes. The analyses can be performed in normal air pressure, simplifying both laboratory and in-field measurements.

Acknowledgements

The work was supported by Alphamon, a project mainly financed by Tekes. Other Alphamon funders are Outokumpu

Stainless Oy, Rautaruukki Oy, FNsteel Oy Ab, Senya Oy, Mirion Technologies (RADOS) Oy, and Environics Oy. Figure 1 was drawn by Nina Sulonen from STUK.

References

- [1] S. Ihantola, A. Pelikan, R. Pöllänen, H. Toivonen, Nuclear Instruments and Methods in Physics Research Section A: Accelerators, Spectrometers, Detectors and Associated Equipment 656 (2011) 55.
- [2] T. Siiskonen, R. Pöllänen, Nuclear Instruments and Methods in Physics Research Section A: Accelerators, Spectrometers, Detectors and Associated Equipment 558 (2006) 437.
- [3] R. Pöllänen, T. Siiskonen, S. Ihantola, H. Toivonen, A. Pelikan, K. Inn, et al., Applied Radiation and Isotopes 70 (2012) 733.
- [4] K. Peräjärvi, S. Ihantola, R. Pöllänen, H. Toivonen, J. Turunen, Environmental Science & Technology 45 (2011) 1528.
- [5] F. Lamadie, F. Delmas, C. Mahe, P. Girones, C. Le Goaller, J.R. Costes, IEEE Transactions on Nuclear Science NS52 (2005) 3035.
- [6] V. Hannuksela, Remote detection of alpha radiation by fluorescence of nitrogen, Master's thesis, Tampere University of Technology, 2009.
- [7] V. Hannuksela, J. Toivonen, H. Toivonen, J. Sand, Optical Remote Detection of Alpha Radiation, Third European IRPA Congress, 2010, 1750.
- [8] S.M. Baschenko, Journal of Radiological Protection 24 (2004) 75.
- [9] A.N. Bunner, Cosmic Ray Detection by Atmospheric Fluorescence, Ph.D. Thesis, Cornell University, 1967.
- [10] T. Waldenmaier, Spectral Resolved Measurement of the Nitrogen Fluorescence Yield in Air Induced by Electrons, Wissenschaftliche Berichte FZKA 7209, 2006.
- [11] P. Bachelor, D. Jordan, W. Harper, B. Cannon, E. Finn, Journal of Radio-analytical and Nuclear Chemistry 282 (2009) 873.
- [12] J. Sand, Properties and Applications of Alpha-Radiation-Induced Fluorescence of Air, Master's Thesis, Tampere University of Technology, 2012.
- [13] L.A. Currie, Analytical Chemistry 40 (1968) 586.
- [14] Radionuclide Analysis and Evaluation Software Aatami, Software Version 4.10, User's Manual, CTBTO Preparatory Commission, 2007.
- [15] R. Mirzoyan, M. Laatiaoui, M. Teshima, Nuclear Instruments and Methods in Physics Research Section A 567 (2006) 230.

Publication V

S. Ihantola, J. Sand, K. Peräjärvi, J. Toivonen, and H. Toivonen

“Fluorescence-Assisted gamma spectrometry for surface contamination analysis”

IEEE Transactions on Nuclear Science, vol. 60, no. 1, pp. 305-309, 2013.

© 2013 IEEE.

Reproduced with permission.

Fluorescence-Assisted Gamma Spectrometry for Surface Contamination Analysis

Sakari Ihanntola, Johan Sand, Kari Peräjärvi, Juha Toivonen, and Harri Toivonen

Abstract—A fluorescence-based alpha-gamma coincidence spectrometry approach has been developed for the analysis of alpha-emitting radionuclides. The thermalization of alpha particles in air produces UV light, which in turn can be detected over long distances. The simultaneous detection of UV and gamma photons allows detailed gamma analyses of a single spot of interest even in highly active surroundings. Alpha particles can also be detected indirectly from samples inside sealed plastic bags, which minimizes the risk of cross-contamination. The position-sensitive alpha-UV-gamma coincidence technique reveals the presence of alpha emitters and identifies the nuclides ten times faster than conventional gamma spectrometry.

Index Terms—Alpha-induced UV, coincidence technique, focused gamma measurement.

I. INTRODUCTION

ISOTOPES emitting alpha radiation pose a special safety and security concern in the proliferation of nuclear weapons, reactor accidents or through their direct criminal use [1]–[3]. Conventional techniques for the detection of alpha emitters are usually inefficient for two reasons. First, alpha particles are difficult to measure and analyze. Due to the short range of alpha particles in air, either the alpha detector must be very close to the source (around 1 cm) or a sample must be taken and measured in a vacuum. Distinguishing isotopes such as ^{239}Pu and ^{240}Pu is challenging, even in laboratory measurements for chemically prepared samples [4], [5]. Second, the gamma radiation produced in the decay is often weak and mainly of low energy. The detection of freshly purified materials cannot rely on progenies emitting intense gamma radiation. Low-energy gamma spectrometry is further complicated due to the presence of photons originating from other unstable nuclides.

These complications can be partly overcome by using an alpha detector to trigger a gamma measurement. In this alpha-gamma coincidence technique, only those gamma photons that are detected simultaneously with an alpha particle are recorded. The alpha-gated gamma spectra are almost free from external background, i.e., the gate rejects the gamma rays originating from beta-active isotopes in the source or

surroundings. Thus, gamma rays with the smallest yields are also detectable [6]. The alpha-gamma coincidence technique is not restricted to chemically prepared samples. However, the large stopping power of alpha particles in media between the contaminated surface and the detector limits the geometry of the conventional alpha-gamma technique.

In the present work, we resolve the alpha-particle range issue by using UV radiation to trigger the gamma measurement. The general principle of this UV-gamma coincidence approach has been presented in Ref. [7]. When absorbed in air, each alpha particle generates several UV photons within a time interval of 5 ns. These UV photons can be detected over long distances (see also [8]–[12]). The only criterion is a line-of-sight from the UV detector to the air where the alpha particles are absorbed. The fluorescent light is mainly emitted by molecular nitrogen at wavelengths of 316, 337, 358, 380 and 391 nm [13]. The energy of these UV photons does not depend on the energy of the alpha particle. The number of UV photons produced is generally considered to be directly proportional to the energy absorbed in air [10].

II. EXPERIMENT

A. Measurement setup

The UV-gamma coincidence setup is presented in Fig. 1. Unlike in the earlier experiments conducted in total darkness and in nitrogen surroundings [7], all measurements in this work were performed in dim red LED lighting and in normal room air. The LED lights enabled untroubled operation in the laboratory, and also the photograph in Fig. 1 has been taken in this lighting. The temperature and pressure of the air were not monitored during the experiment, but the conditions were close to SATP (25 °C, 100 kPa).

The optical photons used for the detection of alpha particles were collected with an objective and recorded with a channel photomultiplier (PMT, MP-1982P, Perkin Elmer). The objective consisted of two UV fused silica plano-convex lenses (75 mm & 50 mm, Thorlabs) and a broadband UV-transmitting filter (UG11, Schott Glass). This detector-filter combination maintains a good sensitivity in the near-UV region while suppressing most of the visible light. The discrimination level of the photomultiplier was optimized for photon counting, and it exhibited only few dark counts per second due to the low noise characteristic of the channel structure. The last part of the optical detection system was a gate generator that was triggered upon the detection of a photon to produce a 1.0 μs gate signal for the gamma detector.

The gamma detection system consisted of a broad-energy germanium detector (HPGe, crystal diameter 70 mm and

S. Ihanntola, K. Peräjärvi, and H. Toivonen are with STUK – Radiation and Nuclear Safety Authority, P.O. Box 14, FI-00881 Helsinki, Finland (e-mail: firstname.lastname@stuk.fi).

J. Sand, and J. Toivonen are with Optics Laboratory, Tampere University of Technology, P.O. Box 692, FI-33101 Tampere, Finland (e-mail: firstname.lastname@tut.fi).

Manuscript received July 10, 2012; revised November 20, 2012; accepted Month Date, 2012. The work was supported by Alphascan, a project mainly financed by Tekes. Other Alphascan funders are Outokumpu Stainless Oy, Rautaruukki Oyj, FNSteel Oy Ab, Senya Oy, Mirion Technologies (RADOS) Oy, and Environics Oy.

thickness 20 mm), a preamplifier, a linear amplifier and two multichannel analyzers. During the experiments, the amplifier shaping time was 1.0 μ s. One multichannel analyzer (MCA) was set to record all gamma pulses, whereas the other MCA accepted only those pulses in coincidence with the UV signal.

The UV-gate technique was investigated by measuring a weak ^{241}Am source (50 Bq) in high gamma background. The active area of the ^{241}Am source had a diameter of 5 mm, and it was located in the focus of the UV detection system. The distance from the source to the closest lens of the UV detector and entrance window of the gamma detector was 100 mm. It should be noted that the range of ^{241}Am alpha particles in air is only about 40 mm. To generate an elevated gamma background typical of safeguards measurements, a ^{133}Ba source of 76 kBq was set to a distance of 80 mm from the germanium detector.

B. Analyses

The analyses were based on measurements of 40 h performed both with and without the ^{241}Am source. Measurements without the source were performed to determine the background level. Due to the high gamma background, the extra background caused by the ^{241}Am source was negligible. The gamma spectrum analyses were based on the 59.5 keV gamma photons of ^{241}Am emitted in coincidence with 5.5 MeV alpha particles. For the analyses, the number of counts at an energy range 1.25 times the peak's FWHM (Full-Width at Half-Maximum) was summed. The peak area within this range covers 85.9% of the full peak.

The statistical detection limit analyses were performed with Currie's method [14]. In the analysis, a 5% risk level for type I (false positive) and type II (false negative) errors was used in the calculation of Currie's critical limit (L_c), peak significance and the minimum detectable activity (MDA). The peak significance is determined as the ratio of the peak area to L_c .

III. RESULTS

A. Singles UV measurement

Even though the LED lighting caused a significant background level of 58 counts per second (c/s), the UV detector alone was capable of detecting the ^{241}Am source. The source increased the signal by 2 c/s. This figure, together with the activity of the source, suggests an alpha particle detection efficiency of about 4%. The alpha particle detection efficiency was more accurately determined by dividing the area of the 59.5 keV ^{241}Am peak in the gated gamma-ray spectrum with the area of the same peak in the singles spectrum. The resulting alpha detection efficiency of the UV detector was $3.9\% \pm 0.3\%$ (see Table I).

For comparison, the geometrical detection efficiency of a conventional alpha detector having the same geometry as the UV collection lens would be 3.2%. However, no single alpha particle would be detected in these experimental conditions, since they would not reach the detector surface. The measurement was also successfully repeated for a sample inside a transparent plastic bag; 75% of the UV photons penetrated the bag.

TABLE I
COMPARISON OF UNGATED AND UV-GATED GAMMA MEASUREMENTS

	Ungated	Gated
Peak area (counts)	35100 ± 1600	1375 ± 74
Background area (counts)	639600 ± 1600	43 ± 13
Curries L_c (counts)	1316	11
Signal-to-noise ratio	0.047	27.5
Peak significance	22.9	109
MDA (Bq)	3.8	0.88

B. UV-gated gamma measurement

The UV-gated gamma measurement was more sensitive to small ^{241}Am signals than a singles gamma measurement. The 59.5 keV gamma-ray peak of ^{241}Am is negligible in the gamma spectrum measured without the UV-gate (Fig. 2a) but clearly visible in the UV-gated spectrum (Fig. 2b). Analyses of the spectra (Table I) reveal the reason for the increase in sensitivity; although the UV gate greatly reduces the photopeak signal, the reduction in the background is over 500 times more intense. For example, an acquisition time of 40 h is required to reach an MDA of 3.8 Bq without the UV gate, whereas with the UV gate, the same MDA can be reached in less than 4 h (see Fig. 3 for MDA versus measurement time).

The X-ray part of the spectrum, even though it only contains elemental information, is important for the detection of plutonium. $^{239,240}\text{Pu}$ and ^{241}Am decays produce comparable amounts of L X-rays, but the gamma yields for Pu are several orders of magnitude lower than for ^{241}Am . The detection of these X-rays is only possible in low background achieved with the UV gate (Fig. 2b). The L X-rays of plutonium have energies in the range of 12-20 keV, and these can be separated from ^{241}Am X-rays [6].

The possibility of using the UV gate to focus the gamma measurement in a single spot was investigated by moving a ^{241}Am source (activity of 1.9 kBq) perpendicular to the focal axis of the UV detector. The detection efficiencies as a function of the offset are illustrated in Fig. 4. When moved aside, the distance to the germanium detector also changed, causing a slope in the gamma efficiency curve. As can be seen, the UV efficiency will fall below one tenth when the source is only 50 mm off focus of the UV detector.

IV. DISCUSSION

Even though the power of the UV-gamma -coincidence measurement is demonstrated with ^{241}Am , the results are valid for various nuclides decaying through alpha particle emission. Energies of the emitted alpha particles are typically above 4 MeV. This is the case for many nuclides that play a critical role in nuclear safety and security, such as ^{239}Pu , ^{240}Pu and ^{235}U . Therefore, the number of UV-photons generated in air is reduced by only some tens of percents as compared with ^{241}Am . This has only a minor influence to the MDA compared to the advantages provided by UV gating. Consequently for plutonium and uranium, the UV-gated measurement remains superior to singles gamma measurement, even if the alpha detection efficiency is slightly lower than for ^{241}Am .

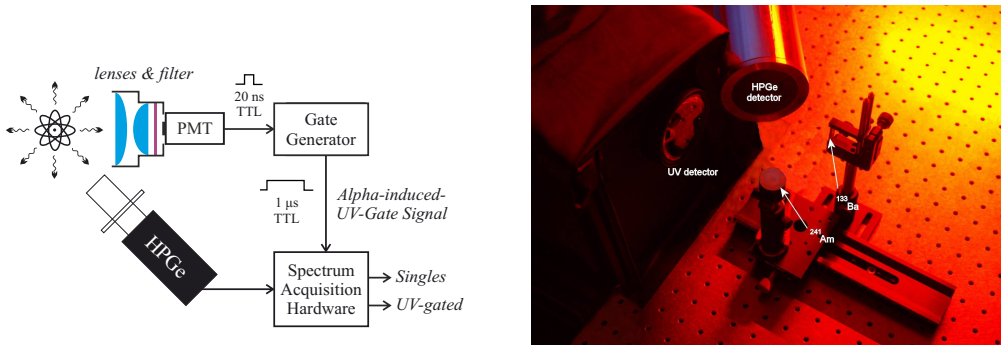


Fig. 1. Measurement setup used in the experiments.

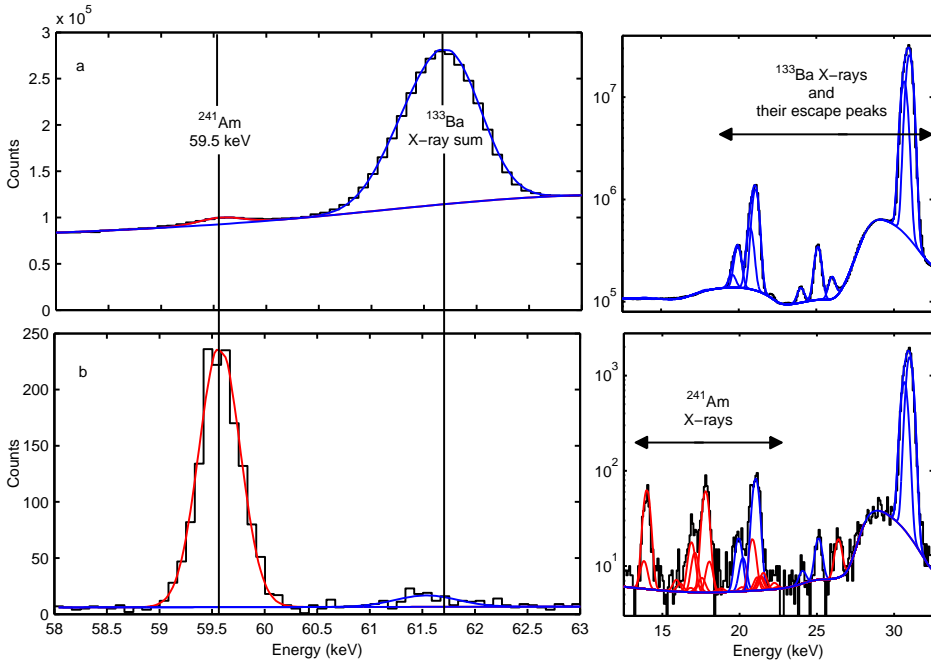


Fig. 2. Singles (a) and UV-gated (b) gamma-ray spectrum of the 59.5 keV ^{241}Am line. The X-ray parts of the same spectra are also shown. The measurements were performed in a high gamma background generated with ^{133}Ba . The ^{133}Ba peaks in the gated spectrum are caused by random coincidences.

The coincidence method does not depend on the age of the material, since the measurement is focused on the plutonium or uranium nuclides themselves, not on their progenies. The progenies of these isotopes that emit most intense gamma radiation decay through beta emission. Because the UV gating efficiently blocks the gamma photons that are not in coincidence with alpha particles, these progenies have practically no contribution to the gated spectra.

The UV-gated gamma measurement has obviously some limitations under specific conditions. The method is inefficient if alpha particles are not absorbed in air or if the visibility to

the air where the alpha particles are absorbed is blocked, for example, by an aluminum foil. Even painting over the source may be enough to absorb the alpha particles and prevent the formation of the UV photons. On the other hand, the capability to measure only the activity directly on the surface may be a great advantage in some cases. This distinction is especially important for the radiation safety, since surface contaminations pose a higher health risk than sealed sources. Determining the fraction of the alpha activity directly on the surface is possible by analyzing both the singles and UV-gated gamma spectra.

As with all coincidence methods, the UV-gamma coinci-

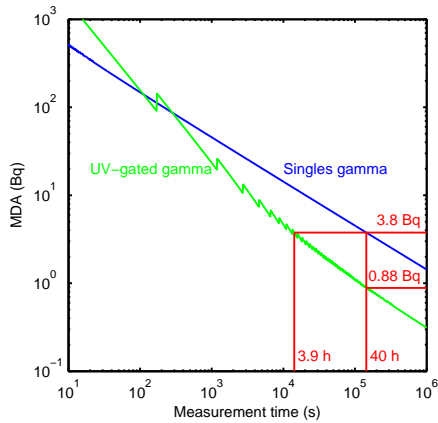


Fig. 3. MDA of ^{241}Am in singles and UV-gated gamma measurement by using 5% risk levels. The saw-edge shape is due to the requirement for an integer number of counts.

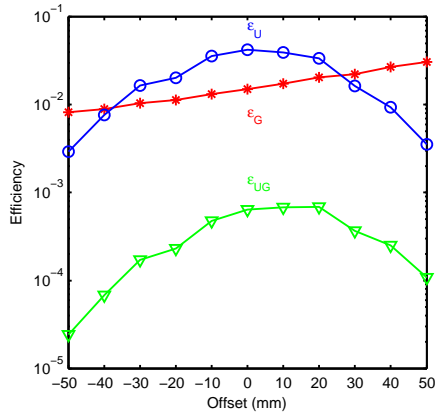


Fig. 4. Detection efficiencies as a function of the source offset from the focal axis of the UV detector. ϵ_G refers to the gamma detection efficiency, ϵ_U to the UV detection efficiency and ϵ_{UG} to the UV-gated gamma detection efficiency. ϵ_G and ϵ_{UG} are measured efficiencies whereas ϵ_U is calculated by $\epsilon_{UG} = \epsilon_U \epsilon_G$.

dence approach increases the MDA the most when the source-to-detector distance is short. Far from the source, the detection efficiency in a singles gamma measurement is inversely proportional to the distance squared (x^2). In a gated measurement instead, the efficiency is inversely proportional to the distance to the power of four (x^4). A higher alpha efficiency is easily achieved by improving the UV collection with larger lenses. However, enhancing the MDA with the coincidence method is complicated if the source-to-detector distance is more than a meter.

Additionally, since the gate reduces the background to the detriment of the efficiency, UV-gating is better suited for long measurements in high gamma background than for short measurements in low background. A typical acquisition time

where advantages are obtained is rather minutes or hours than seconds (see Fig. 3 for more details).

V. CONCLUSIONS

Triggering a gamma detector with UV photons induced by alpha particles is a major step forward in the stand-off detection of actinides and other alpha emitters. The method allows the analyses of isotopes decaying through alpha-particle emission from distances greater than the range of alpha particles in air. Together with a UV-transmitting filter, a photomultiplier tube can be operated for alpha detection in LED lighting. Because UV radiation penetrates many transparent materials, the method is also suited for the analysis of samples inside closed packings.

UV-gated gamma spectroscopy enables the position-sensitive detection and identification of alpha emitters even in a highly contaminated environment. The gate efficiently rejects the gamma photons from alpha sources further than 50 mm off from the measurement focus. The gated spectrum is also almost free from gamma photons not in coincidence with alpha particles. Due to the low background, the achievable MDA in a UV-gated measurement is lower than in a singles gamma measurement.

UV-gamma coincidence can be further optimized for various applications. An obvious usage is screening of contaminated surfaces. Especially decommissioning of nuclear facilities and crime scene investigation would greatly benefit from the detection and analysis of alpha contamination at a stand-off distance. Compared to the strict geometry requirements in a direct alpha measurement, the UV technique offers significant flexibility. For example, even an alpha contamination on the inside wall of a steel drum could be analyzed by looking inside the drum through the lid with a UV detector.

UV-gamma coincidence is also suited for the detection and identification of fissile materials inside a glove box through a closed plexiglass. The feasibility of UV-imaging has already been demonstrated in this environment [9]. A further increase in the UV signal can be achieved by replacing the air in the glove box with some other gas, such as pure nitrogen, which produces a UV signal several times larger than the signal in room air [7]. In general, the random coincidences caused by the UV photons from lighting can be prevented by performing the measurements in darkness. In darkness, the UV filter, which absorbs part of the fluorescent signal, is also not required.

A further potential application for UV-gamma coincidence is the analyses of swipe samples without opening the sealed plastic bags or other transparent packings. This is especially important in nuclear safeguard and forensics, since it guarantees the integrity of the samples and prevents cross-contamination [15], [16]. It should be noted that the alpha particles from a sample in a closed plastic bag would not produce any signal in a gas proportional counter, since they do not penetrate the plastic. The swipe samples typically contain a large amount of non-radioactive dust, which may also contain materials that absorb alpha radiation and emit fluorescent light [17]. The alpha detection efficiency can be drastically

improved by placing the sample in a closed chamber with reflecting surfaces.

REFERENCES

- [1] R. Stone, "State-of-the-art nuclear sleuths," *Science*, vol. 300, no. 5626, pp. 1643–1643, June 2003.
- [2] J. van der Veen, A. van der Wijk, W. G. Mook, and R. J. de Meijer, "Core fragments in Chernobyl fallout," *Nature*, vol. 323, no. 6087, pp. 399–400, October 1986.
- [3] M. Levi and H. Kelly, "Weapons of mass disruption," *Sci. Am.*, vol. 287, no. 5, pp. 76–81, 2002.
- [4] R. D. Horansky, J. N. Ullom, J. A. Beall, G. C. Hilton, K. D. Irwin, D. E. Dry, E. P. Hastings, S. P. Lamont, C. R. Rudy, and M. W. Rabin, "Superconducting calorimetric alpha particle sensors for nuclear nonproliferation applications," *Appl. Phys. Lett.*, vol. 93, no. 12, p. 123504, 2008.
- [5] R. Pöllänen, T. Siiskonen, S. Ihanntola, H. Toivonen, A. Pelikan, K. Inn, J. L. Rosa, and B. Bene, "Activity determination without tracers in high-resolution alpha-particle spectrometry," *J. Radioanal. Nucl. Chem.*, vol. 290, no. 3, pp. 551–555, 2011.
- [6] K. Peräjärvi, S. Ihanntola, R. Pöllänen, H. Toivonen, and J. Turunen, "Determination of ^{235}U , ^{239}Pu , ^{240}Pu , and ^{241}Am in a nuclear bomb particle using a position-sensitive α - γ coincidence technique," *Environ. Sci. Technol.*, vol. 45, no. 4, pp. 1528–1533, February 2011.
- [7] S. Ihanntola, J. Sand, K. Peräjärvi, J. Toivonen, and H. Toivonen, "Principles of UV-gamma coincidence spectrometry," *Nucl. Instrum. Meth. Phys. Res. A*, 2012, in press (DOI: 10.1016/j.nima.2012.06.044).
- [8] M. Nagano, K. Kobayakawa, N. Sakaki, and K. Ando, "Photon yields from nitrogen gas and dry air excited by electrons," *Astropart. Phys.*, vol. 20, no. 3, pp. 293–309, December 2003.
- [9] F. Lamadie, F. Delmas, C. Mahe, P. Girones, C. L. Goaller, and J. R. Costes, "Remote alpha imaging in nuclear installations: new results and prospects," *IEEE Trans. Nucl. Sci.*, vol. 52, no. 6, pp. 3035–3039, 2005.
- [10] T. Waldenmaier, "Spectral resolved measurement of the nitrogen fluorescence yield in air induced by electrons," Ph.D. dissertation, University of Karlsruhe (TH), 2006, FZKA7209.
- [11] P. Bachelor, D. Jordan, W. Harper, B. Cannon, and E. Finn, "Self-absorption effects on alpha-induced atmospheric nitrogen fluorescence yield," *J. Radioanal. Nucl. Chem.*, vol. 282, no. 3, pp. 873–876, 2009.
- [12] D. L. Chichester and S. M. Watson, "Multispectral UV-visual imaging as a tool for locating and assessing ionizing radiation in air," in *Conf. Rec. 2010 IEEE Nuclear Science Symposium (NSS/MIC)*, pp. 447–453.
- [13] T. Waldenmaier, J. Blümer, and H. Klages, "Spectral resolved measurement of the nitrogen fluorescence emissions in air induced by electrons," *Astropart. Phys.*, vol. 29, no. 3, pp. 205–222, April 2008.
- [14] L. A. Currie, "Limits for qualitative detection and quantitative determination. application to radiochemistry," *Anal. Chem.*, vol. 40, no. 3, pp. 586–593, March 1968.
- [15] "Nuclear forensics support, reference manual," IAEA, Tech. Rep., 2006.
- [16] "Safeguards techniques and equipment," IAEA, Tech. Rep., 2011.
- [17] S. B. Utter, P. Beiersdorfer, A. Barnes, R. W. Lougheed, J. R. C. Lopez-Urrutia, J. A. Becker, and M. S. Weiss, "Reexamination of the optical gamma ray decay in Th-229," *Phys. Rev. Lett.*, vol. 82, no. 3, p. 505, January 1999.

Publication VI


J. Sand, S. Ihanola, K. Peräjärvi, H. Toivonen, and J. Toivonen

“Optical detection of radon decay in air”

Scientific Reports, vol. 6, p. 21532, 2016.

Creative Commons Attribution 4.0 License.

SCIENTIFIC REPORTS



OPEN

Optical detection of radon decay in air

Johan Sand^{1,2}, Sakari Ihtantola^{1,†}, Kari Peräjärvi¹, Harri Toivonen^{1,‡} & Juha Toivonen²

Received: 18 August 2015
Accepted: 27 January 2016
Published: 12 February 2016

An optical radon detection method is presented. Radon decay is directly measured by observing the secondary radioluminescence light that alpha particles excite in air, and the selectivity of coincident photon detection is further enhanced with online pulse-shape analysis. The sensitivity of a demonstration device was 6.5 cps/Bq/l and the minimum detectable concentration was 12 Bq/m³ with a 1 h integration time. The presented technique paves the way for optical approaches in rapid radon detection, and it can be applied beyond radon to the analysis of any alpha-active sample which can be placed in the measurement chamber.

Radon gas is released in soil as a result of radioactive decay of uranium and thoron series. As a radioactive noble gas, radon emanates easily through porous ground to housings and is responsible for 42% of the annual radiation dose of population in the world¹. It is widely observed that exposure to radon leads to increased risk of lung cancer^{2,3}. Radon and some of the daughter atoms decay by emitting alpha particles which have short range in air but high damage potential if absorbed in living cells. Radon progenies are easily adhered to surfaces and therefore, the upper respiratory tract is exposed to the highest radiation dose. Due to its carcinogenic nature, radon monitoring is required in risk areas.

Radon levels are typically measured by leaving a piece of special film in a room for a fixed period of time, and the number of alpha particles incident on the film is later counted in a laboratory analysis. This approach provides a reliable and low-cost estimate of the average radon level in the premises but it is not suited to online monitoring applications. In contrast, a fast response is required in the fields of mining industry, uranium exploration, and in verification of radon repairs. Continuous radon monitoring can also be used as a warning system for earthquakes which are known to increase radon levels shortly prior to the event^{4,5}. Currently, detectors employing ionisation chambers, semiconductor sensors, or zinc-sulphide scintillation (Lucas) cells are often used for these applications³.

The absorption of alpha particles in air induces secondary radioluminescence light which can be utilized for remote detection of alpha decay⁶. The light is generated by radiative relaxation of nitrogen molecules, excited by secondary electrons. The conversion efficiency from kinetic energy into optical radiation is 19 photons per each MeV of energy released in air⁷. This corresponds to approximately 100 photons when a single ²²²Rn nucleus releases all of the 5.6 MeV decay energy into air. Most of the photons are observed in the near UV region between 300 nm and 400 nm⁸. The increased range and multiplication of signal carriers are the key benefits of an optical alpha particle detection method.

This work presents the principle and first results of an optical radon measurement. The feasibility of the technique is proven using a demonstration device which is applied to a step-response test and to a longer field test to observe daily variation of radon concentration at an office property. Furthermore, the optical detector is calibrated against an established commercial detector. The technique enables direct radon detection with exceptionally large active volume and high efficiency.

Method

The optical radon measurement is based on simultaneous detection of multiple secondary photons from the same decay event. Since the photons are generated along the alpha particle track and emitted isotropically, it is beneficial to have a measurement volume with highly reflective walls. This enhances detection probability of a single photon by allowing multiple reflections before absorption. The ideal shape of the volume is a sphere since it has the greatest volume-to-surface-area ratio, which minimizes absorption of alpha particles into walls. For these

¹STUK - Radiation and Nuclear Safety Authority, P.O. Box 14, FI-00881 Helsinki, Finland. ²Tampere University of Technology, Department of Physics, P.O. Box 692, FI-33101 Tampere, Finland. [†]Present address: University of Oxford, Department of Physics, Denys Wilkinson Building, Keble Road, OX1 3RH, Oxford, United Kingdom. [‡]Present address: HT Nuclear Ltd, Notkokatu 4, FI-05880 Hyvinkää, Finland. Correspondence and requests for materials should be addressed to J.S. (email: johan.sand@stuk.fi)

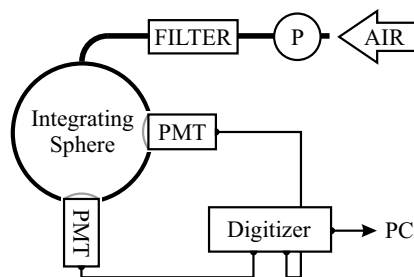


Figure 1. Optical radon detection setup. A pump (P) forces air into the detection volume through a filter which removes radon progenies from the incoming air. The sample leaves the detector through the PMT ports.

reasons, an integrating sphere was used in the measurement setup. The sphere selected for this work (SPH-8-3 AdaptaSphere, Labsphere) has a diameter of 20 cm and it is coated with Spectrafect, which is a BaSO_4 -based diffusive reflector. It has an estimated reflectance of 97% for the nitrogen emission.

A pump was used to continuously circulate air through the sphere with a measured flow rate of 1.4 l/min. A HEPA (high efficiency particulate) filter was placed between the pump and the sphere to remove radon progenies and dust from the inlet air. This ensured that the ambiguous radon-daughter equilibrium could not interfere with signal level. Since only radon could enter the detector, it is assumed that all ^{222}Rn decays in the sphere are followed by two additional alpha decays of the two short-lived daughter atoms, namely ^{218}Po and ^{214}Po . The detection efficiency for daughter decay is limited to 50%, provided that they are adhered to the sphere surface and scintillation properties of BaSO_4 are negligible.

The coincident detection of the secondary photons was conducted with two photomultiplier tubes (PMTs) (9829QB, ET Enterprises). They were selected to provide a high detection efficiency with the large domed windows (46 mm diam. active area), which were sandblasted to further enhance sensitivity. The PMTs were operated in the photon counting regime with a gain of 10^7 , at voltages specified by the manufacturer. A schematic representation of the experimental setup is depicted in Fig. 1.

A fast digitizer (DT5751, Caen) was used to record the events in list mode with 1 ns time-stamp resolution. The device features an online coincidence detection system and a software package for pulse shape discrimination (PSD), which is typically used for neutron-gamma discrimination⁹. This is based on charge integration in two time windows of different lengths. The PSD figure is calculated from the integrated charges with equation

$$PSD = \frac{Q_{long} - Q_{short}}{Q_{long}}. \quad (1)$$

Both of the integration windows start 1 ns after the trigger signal (threshold 19.5 mV, coincidence window 32 ns) which is the minimum allowed gate offset of the digitizer. The length of the short integration window was set to 7 ns, while the long integration window was 50 ns throughout this work. The values were selected to give clear separation of alpha particles from background events.

The key concept of pulse shape discrimination is that one PMT can detect several secondary photons from the same alpha decay event, when an integrating sphere is used as detection volume. Importantly, the photons will arrive at different times since they are emitted at different times and they can travel long distances in the sphere before detection. The flight time of an alpha particle is approximately 5 ns^{10} and most of the photons are emitted within few ns after excitation due to short lifetime of the excited states⁸. However, the most significant pulse stretching arises from the random path length that photons travel in an integrating sphere. The flight time of a photon can be estimated from the sphere multiplier¹¹ (M) and average path length¹² (L) in the sphere

$$t = \frac{1}{c} \cdot M \cdot L = \frac{1}{c} \cdot \frac{\rho}{1 - \rho(1 - f)} \cdot \frac{2}{3}d. \quad (2)$$

Here, c is the speed of light, ρ is the average sphere reflectance for nitrogen emission, f is the fraction of port area to sphere surface area (0.031), and d is the diameter of the sphere. By substituting the relevant values, and assuming that the absorption of near UV light is negligible in air, the equation shows that the average lifetime of a photon in the sphere is 7 ns.

Results

The optical radon detector was applied to several tests in the ground floor of a university building in Tampere, Finland. The property is ventilated during extended office hours only, which leads to a significant rise in radon levels during nights and weekends. This natural radon occurrence and its daily variation was utilized in this work.

The UV signal is categorized on the basis of pulse-shape. The PSD values of coincident PMT signals are presented in a two-dimensional histogram in Fig. 2a, which contains all events that were recorded during a two week measurement period. Notably, the histogram reveals that pulses accumulate in four main regions, which are named ABCD. Each of these regions responds to changes in radon concentration but the signal-to-background

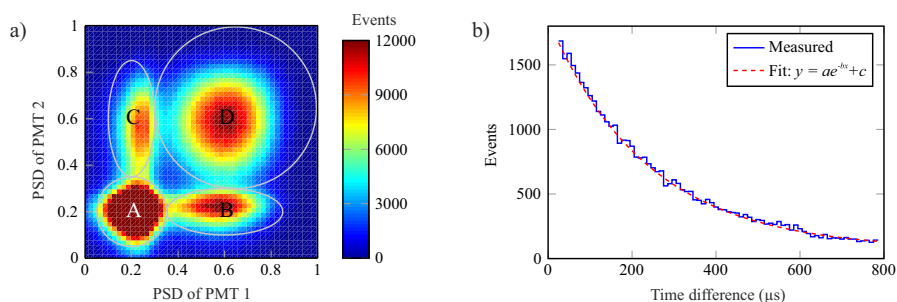


Figure 2. (a) Distribution of coincident pulse shapes over two week measurement period. Radon events accumulate to regions BCD while type A signals are mostly single photoelectron pulses. The peak value in region A is 45 000. (b) Time difference of subsequent coincidence events. The fitting verifies that the half-life is 164.3 μs , as expected for ^{214}Po .

ratio is the best for type D signal. In this region, both PMTs detect several photons so that 40% of total charge is in the short integration window. These pulses can reduce to regions B and C if one detector captures only one photoelectron or if multiple photons arrive simultaneously. Type A signals consist of single photoelectron events related to random coincidences, beta particles and gamma rays, which have a lower light yield than alpha particles. Here, BCD signals are selected to represent radon events.

The transient response of a radon detector can be limited by the two alpha-emitting daughters (^{218}Po and ^{214}Po) following radon in the uranium series. The first daughter atom after radon decay is ^{218}Po and it reaches secular equilibrium with ^{222}Rn within minutes ($T_{1/2}$ of ^{218}Po is 3.1 min¹³). However, ^{214}Po requires several hours before equilibrium is reached and therefore, it should be separated from the previous two to achieve the best possible time response for the detection.

The current design enables the measurement of ^{214}Po contribution by observing the successive beta and alpha emission of ^{214}Bi and ^{214}Po . In this decay chain, a beta particle of ^{214}Bi is followed by an alpha particle of ^{214}Po , with a half-life of 164 μs ^{14,15}. Using temporal and pulse energy discrimination, the decay of ^{214}Po can be reliably identified with an efficiency of 2.5%. This is verified with a histogram representing the distribution of time differences of consecutive coincidence events in Fig. 2b. The data set allows the determination of ^{214}Po half-life with a high precision and the obtained value of 164.3 μs is in agreement with a recent result of 164.2 (6) μs , also measured using the latest digital electronics¹⁵.

The step response of the detector was investigated during a high radon level (weekend) in the laboratory, using radon-less artificial air as a zero reference. The experiment was started with a two-hour baseline measurement with artificial air, as shown in Fig. 3a. Then, the detector was supplied with an ambient radon sample (870 Bq/m³ on average) for four hours to allow equilibrium formation. Lastly, the flow of artificial air was restored for six hours. The acquired step response is shown with and without the contribution of ^{214}Po to highlight the necessity of ^{214}Po subtraction in rapid measurements.

The experimental data is accompanied by modelled response curves in Fig. 3a. The model is based on the half-lives of radon progenies and it is fitted to the total BCD count data using the detection efficiencies for radon and daughter atoms as free parameters. The calculation shows that a good match is achieved when the detection efficiency of radon decay is 0.7 while both alpha emitting daughter atoms are detected with a reduced efficiency of 0.4 due to absorption into the sphere walls. The results were verified with a Monte Carlo model which showed that exactly the same fractions of radon and daughter alpha particles are fully absorbed into air in a detector of this size and geometry.

The performance of the optical detector was evaluated with a side-by-side test with an AlphaGuard radon monitoring system (Saphymo GmbH), which is based on detection with an ionisation chamber¹⁶. The AlphaGuard was set to record the radon concentration in the laboratory with 1 h integration cycle and the data were used for the calibration of the optical detector. It also logged temperature, humidity and pressure data which were close to 22 °C, 20% and 1000 mbar during the time of measurements. The calibration points were selected to be during late afternoon and early morning hours, when the radon concentration is at its most stable. The observed radon activities varied from below 20 Bq/m³ up to peak levels exceeding 1000 Bq/m³, which were reached during the nights. Using the obtained reference points, a calibration curve for the gross coincidence counts of BCD type signals was acquired, and one additional calibration was performed for the same data where the contribution of ^{214}Po was subtracted. The gross sensitivity of the device was 6.5 cps/Bq/l, while ^{222}Rn and ^{218}Po alone yielded 4.9 cps/Bq/l, as shown in Fig. 3b. The respective detection limits were calculated using Currie's method with a confidence level of 95%¹⁷. The minimum detectable concentration (MDC) under stable background conditions can be expressed as

$$MDC = \frac{2.71 + 3.29\sqrt{R_b t_s}}{t_s \varepsilon}, \quad (3)$$

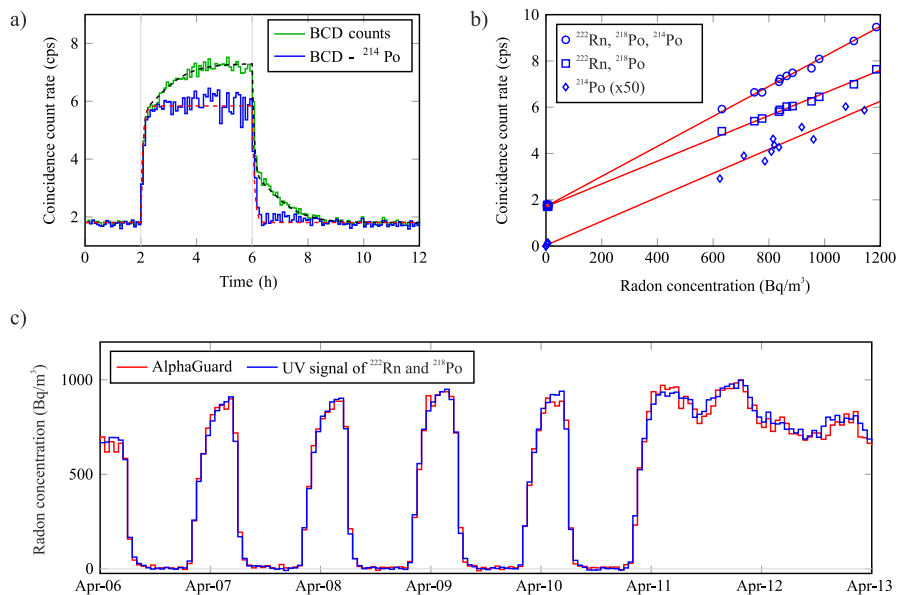


Figure 3. (a) Step response test with artificial air and ambient radon concentration of 870 Bq/m^3 . The start and end of the radon air feed are indicated with vertical lines. The modelled response is shown with a dashed line for both cases, and the experimental data points are averaged for 5 minutes. (b) Calibration of the UV detector with an AlphaGuard radon monitor in steady radon concentrations. The signal of ^{214}Po is multiplied by a factor of 50 to enhance readability. (c) The evolution of UV signals during the in-field experiment. The observed radon signal follows the schedule of the ventilation system, which is active only during extended working hours. The radon concentration is logged with the AlphaGuard and the UV signal of ^{222}Rn and ^{218}Po is calibrated using the data of AlphaGuard. The results are presented with a 1 h integration time.

where R_b is the background count rate, t_s is the sample counting time, and ε is the detection efficiency of decay events per becquerel of radon in one cubic meter (i.e. the slope of linear regression in Fig. 3b). The determined MDC value for one hour measurement was 12 Bq/m^3 for the gross signal and 15 Bq/m^3 for ^{222}Rn and ^{218}Po alone. The reliability of the radon detection is further verified in Fig. 3c where the data of the AlphaGuard and the calibrated UV signal of ^{222}Rn and ^{218}Po are in excellent agreement. It can be also noted that the hour-to-hour fluctuation of the UV signal is minimal.

Discussion

The main difference between the presented and established techniques is that a very high signal count rate can be achieved. Therefore, the method is not limited by statistical uncertainty of signal, which is the case with many radon detection techniques. However, the background signal is higher than in carefully designed Lucas cells and ionisation chambers and therefore, the full potential of the large active volume is not unveiled, when very low radon concentrations (below 12 Bq/m^3) are of interest. Although the detection limits of leading commercial techniques ($1\text{--}2 \text{ Bq/m}^3$)^{16,18} were not currently reached, the performance is already more than adequate for online monitoring of radon. Secondly, the slowly changing signal of ^{214}Po can be omitted to achieve readings without waiting for equilibrium formation within the detector, which is the prevalent approach with Lucas cell designs. For these reasons, the technique shows promise for applications where radon needs to be measured rapidly with small relative uncertainty. It should be also noted that the maximal measurable radon concentration can be at least several MBq/m^3 since air is a very fast scintillator and the secondary photon burst of an alpha particle is shorter than 100 ns even in a large integrating sphere.

The presented device can also be applied beyond radon to surface activity determination of alpha- or beta-emitting samples by placing them into the measurement chamber. The obtained 1 h detection limit of 12 Bq/m^3 for radon equals to an alpha activity of 0.05 Bq in the detection volume, which suggests that the typical definitions of alpha contamination (0.4 Bq/cm^2 for low toxicity emitters and 0.04 Bq/cm^2 for all others¹⁹) are within reach of the presented detection technique. As a practical example, clinical swab samples could be screened down to 0.4 Bq level within a minute with the current device, and by scaling the design, even hand-held tools could be rapidly checked for surface contamination. This could extend the capabilities of current small item monitors²⁰ to include alpha detection, which would be of interest to the nuclear industry. The benefits of the optical approach with respect to conventional techniques are that an integral measurement is performed within the detection volume while no direct interaction with an alpha particle is required for the detection. These factors enable alpha

contamination screening of objects with complex geometries in specifically designed chambers, as long as sufficient photon detection efficiency is ensured with large area photon counters.

Conclusions

A method to directly detect radon decay via radioluminescence photons of air is reported. A demonstration device was developed and its performance was bench-marked with an established commercial detector. The obtained results show that the characteristic optical pulse shape of a radon decay in a highly reflective enclosure can be used to achieve a reliable radon detection in indoor conditions. Additionally, the detection of beta particles was verified and utilized in the identification of ^{214}Bi - ^{214}Po decay to enhance the response for rapid changes in radon concentration. In conclusion, the optical approach is attractive for real-time monitoring, since a large active volume can be used with high efficiency for direct detection of radon decay in air.

References

1. United Nations Scientific Committee on the Effects of Atomic Radiation. *Sources and effects of ionizing radiation UNSCEAR 2008 Report to General Assembly with Scientific Annexes*, vol. 1 (UN, 2008).
2. Darby, S., Hill, D. & Doll, R. Radon: a likely carcinogen at all exposures. *Ann. Oncol.* **12**, 1341–1351 (2001).
3. World Health Organization. *Handbook on indoor radon: a public health perspective* (WHO, 2009).
4. Richon, P. *et al.* Radon anomaly in the soil of Taal volcano, the Philippines: A likely precursor of the M 7.1 Mindoro earthquake (1994). *Geophys. Res. Lett.* **30**, 34-1–34-4 (2003).
5. Cicerone, R. D., Ebel, J. E. & Britton, J. A systematic compilation of earthquake precursors. *Tectonophysics* **476**, 371–396 (2009).
6. Baschenko, S. M. Remote optical detection of alpha particle sources. *J. Radiol. Prot.* **24**, 75–82 (2004).
7. Sand, J., Ihantola, S., Peräjärvi, K., Toivonen, H. & Toivonen, J. Radioluminescence yield of alpha particles in air. *New J. Phys.* **16**, 053022 (2014).
8. Lefeuvre, G., Gorodetzky, P., Dolbeau, J., Patzak, T. & Salin, P. Absolute measurement of the nitrogen fluorescence yield in air between 300 and 430 nm. *Nucl. Instrum. Methods Phys. Res., Sect. A* **578**, 78–87 (2007).
9. Cester, D. *et al.* Pulse shape discrimination with fast digitizers. *Nucl. Instrum. Methods Phys. Res., Sect. A* **748**, 33–38 (2014).
10. Knoll, G. *Radiation Detection and Measurement* (John Wiley & Sons, 2010).
11. Labsphere Inc. Integrating Sphere Theory and Applications (2015). Available at <https://www.labsphere.com/site/assets/files/2551/a-guide-to-integrating-sphere-theory-and-applications.pdf>. Date of access: 20/11/2015.
12. Kirk, J. Modeling the performance of an integrating-cavity absorption meter: Theory and calculations for a spherical cavity. *Appl. Opt.* **34**, 4397–4408 (1995).
13. Bé, M.-M. *et al.* Table of Radionuclides (Vol. 4 - A = 133 to 252) (Bureau International des Poids et Mesures, 2013).
14. Wu, S.-C. Nuclear data sheets for A = 214. *Nucl. Data Sheets* **110**, 681–748 (2009).
15. Suliman, G. *et al.* Measurements of the half-life of ^{214}Po and ^{218}Rn using digital electronics. *Appl. Radiat. Isot.* **70**, 1907–1912 (2012).
16. Saphymo GmbH. AlphaGUARD Radon monitor. Available at http://www.saphymo.com/ftp/ecatalogue/154/29294519EN_C_-_Data_Sheet_ALPHAGUARD.pdf. Date of access: 20/11/2015.
17. Currie, L. A. Limits for qualitative detection and quantitative determination. Application to radiochemistry. *Anal. Chem.* **40**, 586–593 (1968).
18. Sarad GmbH. Radon Scout PMT. Available at http://www.sarad.de/cms/media/docs/handbuch/Manual_Radon_Scout_PMT_EN_29_02_12.pdf. Date of access: 20/11/2015.
19. International Atomic Energy Agency. Regulations for the Safe Transport of Radioactive Material - 2012 Edition, Specific Safety Requirements, Series No. SSR-6 (IAEA, 2012).
20. Canberra Industries. Cronos®-1 Gamma Object/Tool Monitors. Available at http://www.canberra.com/products/hp_radioprotection/pdf/Cronos-1-SS-C40639.pdf. Date of access: 20/11/2015.

Acknowledgements

The authors would like to thank Olli Holmgren for help with the AlphaGuard measurements and Alphamon project (Tekes) for funding.

Author Contributions

K.P., H.T. and J.T. conceived the original idea, J.S. designed the device and signal readout methods, J.S. and S.I. conducted the experiments, J.S. and H.T. analysed the results, J.S. prepared and all authors commented the manuscript.

Additional Information

Competing financial interests: The authors declare no competing financial interests.

How to cite this article: Sand, J. *et al.* Optical detection of radon decay in air. *Sci. Rep.* **6**, 21532; doi: 10.1038/srep21532 (2016).



This work is licensed under a Creative Commons Attribution 4.0 International License. The images or other third party material in this article are included in the article's Creative Commons license, unless indicated otherwise in the credit line; if the material is not included under the Creative Commons license, users will need to obtain permission from the license holder to reproduce the material. To view a copy of this license, visit <http://creativecommons.org/licenses/by/4.0/>

SCIENTIFIC REPORTS

OPEN **Erratum:** Optical detection of radon decay in air

Johan Sand, Sakari Ihantola, Kari Peräjärvi, Harri Toivonen & Juha Toivonen

Scientific Reports 6:21532; doi: 10.1038/srep21532; published online 12 February 2016; updated 22 April 2016

The HTML version of this Article contained a typographical error in the volume number '6', which was incorrectly given as '5'. This has now been corrected.

In addition, there were typographical errors in the Abstract.

"Radon decay is directly measured by observing the secondary radioluminescence light that alpha particles excite in air,"

now reads:

"Radon decay is directly measured by observing the secondary radioluminescence light that alpha particles excite in air,"

"The presented technique paves the way for optical approaches in rapid radon detection,"

now reads:

"The presented technique paves the way for optical approaches in rapid radon detection,"

These errors have now been corrected in the PDF and HTML versions of the Article.



This work is licensed under a Creative Commons Attribution 4.0 International License. The images or other third party material in this article are included in the article's Creative Commons license, unless indicated otherwise in the credit line; if the material is not included under the Creative Commons license, users will need to obtain permission from the license holder to reproduce the material. To view a copy of this license, visit <http://creativecommons.org/licenses/by/4.0/>

Tampereen teknillinen yliopisto
PL 527
33101 Tampere

Tampere University of Technology
P.O.B. 527
FI-33101 Tampere, Finland

ISBN 978-952-15-3882-7
ISSN 1459-2045